

DDC FILE COPY

ADA0 66902

AFAL-TR-78-117

LEVEL

2

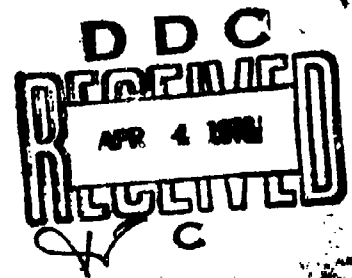
SCANNER DEVELOPMENT

HARRIS CORPORATION
ELECTRONIC SYSTEMS DIVISION
MELBOURNE, FLORIDA 32901



JULY 1978

TECHNICAL REPORT AFAL-TR-78-117



FINAL REPORT FOR PERIOD MAY 1977 - MAY 1978

APPROVED FOR PUBLIC RELEASE; DISTRIBUTION UNLIMITED

AIR FORCE AVIONICS LABORATORY
AIR FORCE WRIGHT AERONAUTICAL LABORATORIES
AIR FORCE SYSTEMS COMMAND
WRIGHT PATTERSON AIR FORCE BASE, OHIO 45433

79 04 05 045

NOTICE

When Government drawings, specifications, or other data are used for any purpose other than in connection with a definitely related Government procurement operation, the United States Government thereby incurs no responsibility nor any obligation whatsoever; and the fact that the government may have formulated, furnished, or in any way supplied the said drawings, specifications, or other data, is not to be regarded by implication or otherwise as in any manner licensing the holder or any other person or corporation, or conveying any rights or permission to manufacture, use, or sell any patented invention that may in any way be related thereto.

This report has been reviewed by the Information Office (OI) and is releasable to the National Technical Information Service (NTIS). At NTIS, it will be available to the general public, including foreign nations.

This technical report has been reviewed and is approved for publication.

David L. Flannery
DAVID L. FLANNERY
Project Engineer
Electro-Optics Techniques and
Applications Group

Kenneth R. Hutchinson
KENNETH R. HUTCHINSON, Chief
Electro-Optics Techniques and
Applications Group
Electro-Optics Technology Branch

FOR THE COMMANDER

Ronald F. Paulson
RONALD F. PAULSON, Acting Chief
Electro-Optics Technology Branch
Electronic Technology Division

"If your address has changed, if you wish to be removed from our mailing list, or if the addressee is no longer employed by your organization please notify AFAA/DHO N-PAFB, ON 45433 to help us maintain a current mailing list".

Copies of this report should not be returned unless return is required by security considerations, contractual obligations, or notice on a specific document.

(19) REPORT DOCUMENTATION PAGE

READ INSTRUCTIONS
BEFORE COMPLETING FORM

REPORT NUMBER

2 GOVT ACCESSION NO.

3. RECIPIENT'S CATALOG NUMBER

(18) AFAL-TR-78-117

(4) TITLE (AND SUBTITLE)

(6) SCANNER DEVELOPMENT

(10) M. C. Greer, B. R. Reddersen
M. L. Shah, T. R. Bader

9. PERFORMING ORGANIZATION NAME AND ADDRESS

Harris Corporation Government Communication
System Division - P.O. Box 37
Melbourne, Florida 32901

11. CONTROLLING OFFICE NAME AND ADDRESS

AF Avionics Laboratory (AFAL/DHO)
Air Force Wright Aeronautical Laboratories

14. MONITORING AGENCY NAME & ADDRESS (if different from Controlling Office)

DCASMA Orlando
3555 Maguire Blvd.
P.O. Box 20025
Orlando, Florida 328145. TYPE OF REPORT & PERIOD COVERED
Final Report
May 1977-May 1978

6. PERFORMING ORG. REPORT NUMBER

8. CONTRACT OR GRANT NUMBER(S)

10. PROGRAM ELEMENT, PROJECT, TASK AREA & WORK UNIT NUMBERS
Project 2001; Task 200102;12. REPORT DATE
July 197813. NUMBER OF PAGES
15316. SECURITY CLASS. OF THIS REPORT
Unclassified

15a. DECLASSIFICATION/DOWNGRADING SCHEDULE

16. DISTRIBUTION STATEMENT (of this Report)

Approved for public release; distribution unlimited

17. DISTRIBUTION STATEMENT (of the material entered in Block 20, if different from Report)

18. SUPPLEMENTARY NOTES

19. KEY WORDS (Continue on reverse side if necessary and identify by block number)

Laser Scanner, Acousto-Optic Beam Deflector (AOBD),
Acoustic Traveling Wave Lens (ATWL)
ELINT Spectrum Analysis

20. ABSTRACT (Continue on reverse side if necessary and identify by block number)

This report describes the development of a high speed laser scanner for spectrum analysis in ELINT applications. A design of an ATWL laser scanner was made with 200KHz line rate, 1000 spots per line and 1000 line format, and a recording bandwidth of 100MHz at 3dB points. An electronic drive circuit was designed and fabricated that achieved a 100% duty line scan with 2% dead time from frame to frame. An analysis was made to determine the optimum drive to the ATWL.

DD FORM 1 JAN 73 1473 EDITION OF 1 NOV 65 IS OBSOLETE

SECURITY CLASSIFICATION OF THIS PAGE (If different from Above)

79 04 03 045
392 092

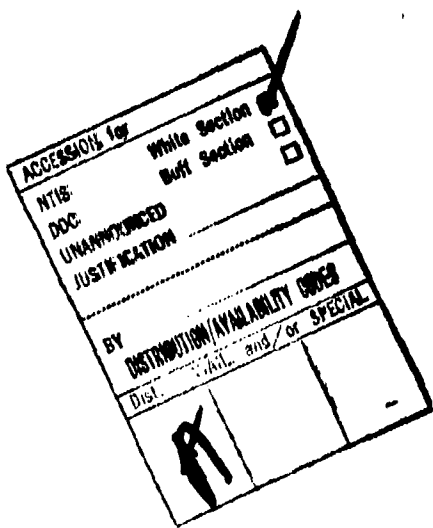
JPC

FOREWORD

This report was prepared by the Electro Optics Department of HARRIS Government Communications System Division, Melbourne, Florida. This effort was sponsored by the Air Force Avionics Laboratory, Contract F33615-77-C-1032, with D. Flannery the Air Force Project Engineer. The work was accomplished in the period May 1977 through May 1978. Principal investigator at Harris GCSD was M. O. Greer. The major contributors to the effort were T. R. Bader, K. R. Porter, B. R. Reddersen, M. L. Shah, T. M. Wolfe, and D. N. Wied.

TABLE OF CONTENTS

<u>Section</u>	<u>Title</u>	<u>Page</u>
I	INTRODUCTION	1
II	SCANNER SYSTEM DESIGN	3
III	DEVICE DEVELOPMENT	62
IV	LASER SCANNER SYSTEM	115
V	CONCLUSIONS	121
VI	RECOMMENDATIONS	123
APPENDIX A	TRANSDUCER IMPULSE RESPONSE	127
APPENDIX B	ELECTRONIC DESIGN	130
APPENDIX C	PROM TEST	146
REFERENCES	149



SECTION I

INTRODUCTION

The primary purpose of the work performed on this contract was to determine the feasibility of using a special high-speed acousto-optic laser scanner as a data recording component (recording onto a device similar to an Itek PROM 1,2,3) of an ELINT system. The laser scanning system under consideration uses a Bragg-effect, acousto-optic beam deflector (AOBD) working in series with an acoustic traveling-wave lens (ATWL) device to produce an extremely fast, high precision laser scanner that uses no moving parts (in the fast scan direction). The program was divided into three tasks:

1. A study and analysis task
2. A device development task
3. A breadboard task

The study and analysis task was performed to determine the best approach for the slow (Y) scan direction, to select a design approach for a 200 MHz modulator, and to determine the optimum drive for efficient lens generation in the ATWL.

As a part of the device development task an AOBD with 100 resolvable spots, 98 percent duty factor scan, and a 200 kHz scan rate was developed where the major emphasis was on a new approach for the drive electronics for the ATWL device. The major development effort on the ATWL was to provide a means for efficient lens generation, and to remove the heat generated by the traveling lens to prevent the cell from breaking due to thermal stresses. In order to show feasibility of using an AOBD/ATWL scanner to meet the 200 kHz scan requirement, a breadboard system was constructed that addressed the following specifications:

Format and size:	Raster scan to produce a 2.5 cm square field of recorded wide-bandwidth signals (maximum)
------------------	---

Fast Axis Resolution (X-Axis):	1000 spots per scanned line (spot width defined at 4 dB points)
Slow Axis Resolution (Y-Axis):	1000 lines per frame
Geometric Fidelity:	Each spot center located to within 0.1 spot diameter of its ideal location
Recording Bandwidth:	100 MHz recorded signal at 6 dB points; 200 MHz electrical-optical analog bandwidth
Recording Duty Cycle:	98 percent (minimum); maximum of 2 percent lost recording time due to all combined effects including line and frame retrace times
Modulation Dynamic Range:	45 dB in light intensity at the recording surface

This report is divided into three major sections. Section II describes the laser scanner system design; Section III presents the results from the device development task; Section IV describes the breadboard and the experimental results. In Section V we provide conclusions and recommendations for future work.

SECTION II

SCANNER SYSTEM DESIGN

In this section a design for a laser scanner system is given; an overview of the complete system is presented first. The subsequent subsections provide more detailed description of the major components. The major components to be described are the acousto-optic modulator, the AOBD/ATWL fast scan approach, a lens design for tracking of the ATWL scan by the AOBD scan, and a design trade-off of a slow Y-scan approach.

2.1 System Concept

A block diagram of a laser scanner system, consistent with the requirements summarized in Section I, is shown in Figure 2.1-1. The system

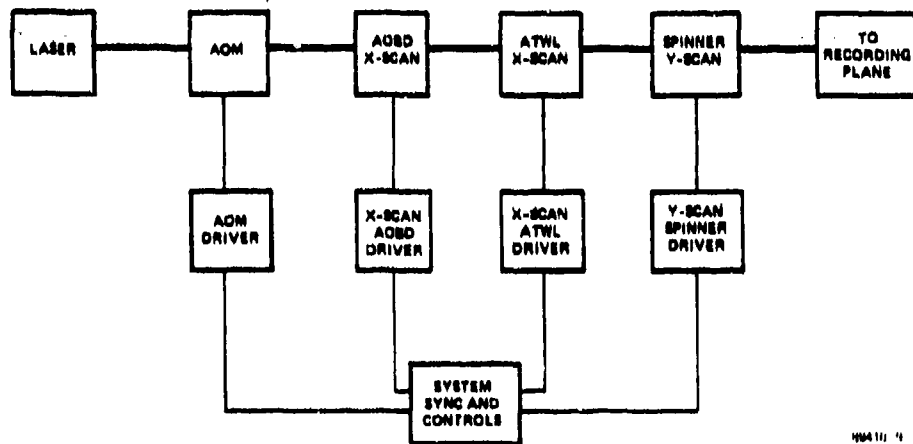


Figure 2.1-1. Block Diagram of X-Y Laser Scanner Subsystem.
consists of a wide bandwidth acousto-optic modulator (AOM) to modulate the intensity of the light during each scan. The fast scan X-axis subsystem consists of a low resolution acousto-optic beam deflector (AOBD) followed by a resolution enhancement element - an acoustic traveling wave lens. The slow scan Y-axis element of the system could be a high resolution AOBD, or a multifaceted rotating

mirror spinner. A trade-off analysis of the Y-scan approaches is given in Section 2.6. The optical system also includes passive elements such as lenses, aperture stops, mirrors, optical filters and mounting fixtures. The electronics to drive various active elements consist of drivers, synchronization, and control signal generation circuitry.

The basic idea involved in increasing the resolution capability of an AOBD beam scanning system is to cascade two different types of acousto-optic devices.⁴ A technique which can be used to obtain a high resolution scanner, utilizing a relatively simple low resolution input beam deflector, is the acoustic traveling wave lens (ATWL). This method consists of a conventional AOBD input scanner, with the scanned spot passing through a second acoustic cell where a traveling strain wave produces a finer focus of the scanned spot.

Figure 2.1-2 provides a more detailed view of the specific AOBD/ATWL line scan recorder system concept. The signal information is imposed on the optical beam by an AOM. From the AOM, the modulated light beam is projected through beam forming optics where it is appropriately shaped to match the rectangular aperture of the AOBD.

From the AOBD, the light beam is projected through the scanner optical system to the aperture of the ATWL. Hence, as the appropriate drive signal is fed into the AOBD, the output beam from the AOBD is scanned across the ATWL cell. In order for this technique to work properly, it is essential that the scan velocity of the beam from the AOBD be precisely matched to the acoustic propagation velocity in the ATWL. Therefore, careful adjustment of the optics between the AOBD and the ATWL is required to achieve tracking. As the beam passes through the ATWL, it is focused to a smaller spot depending upon the power of the acoustic lens. As the acoustic lens travels through the optical material, the final spot traces out a single line which is imaged onto the recording medium. A rotating

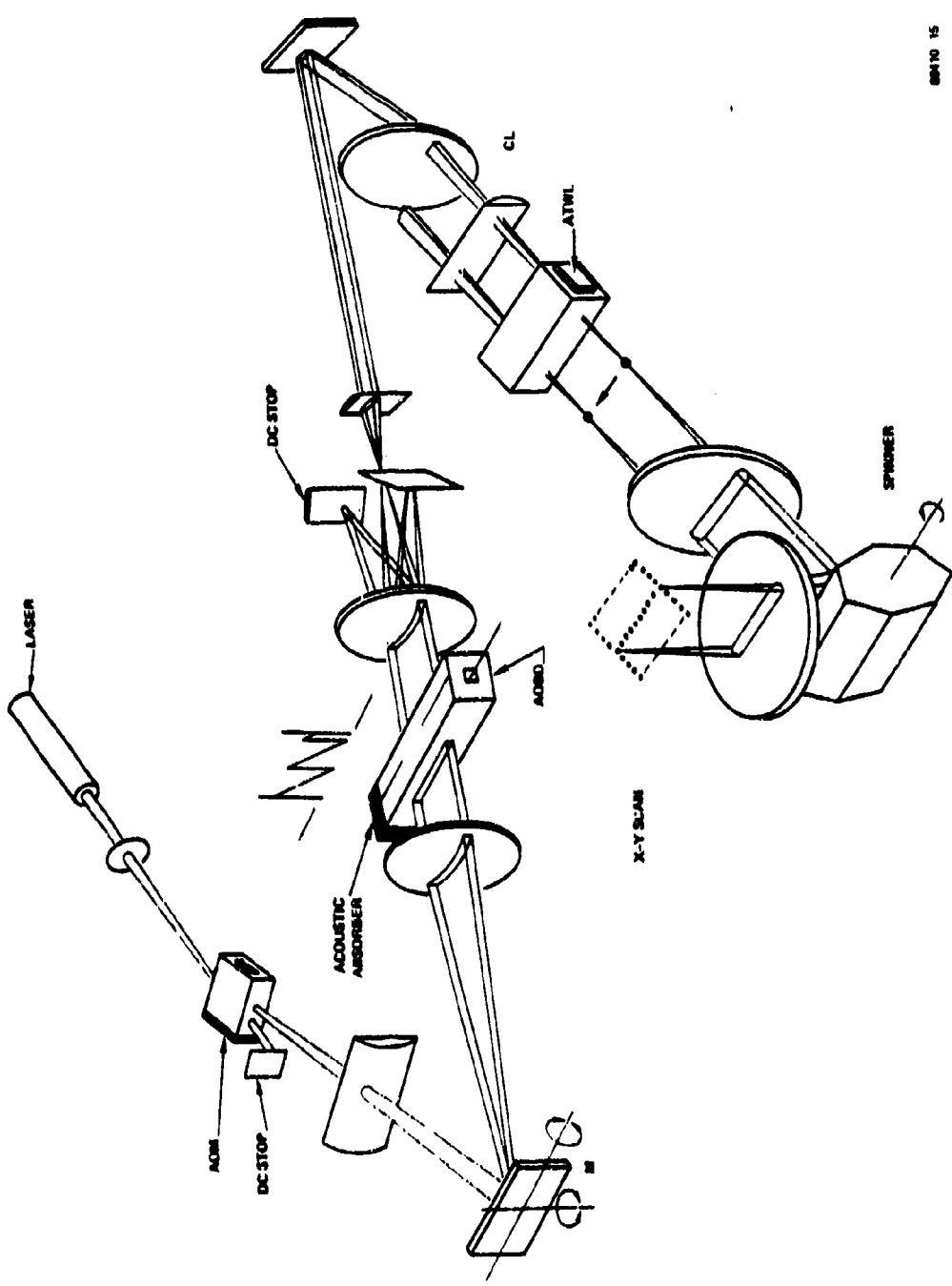


Figure 2.1-2. ATML/AOBD X-Y Laser Scanner System

spinning mirror (or other Y-scan approach) is used to scan the line across the recording medium to form a raster format.

A master clock in the control electronics is used to maintain synchronization between all of the system elements and with the information-bearing signal. The frequency of the clock is maintained at a very stable value by using a crystal-controlled oscillator.

The basic operation of the ATWL, shown in Figure 2.1-3, is to pass the

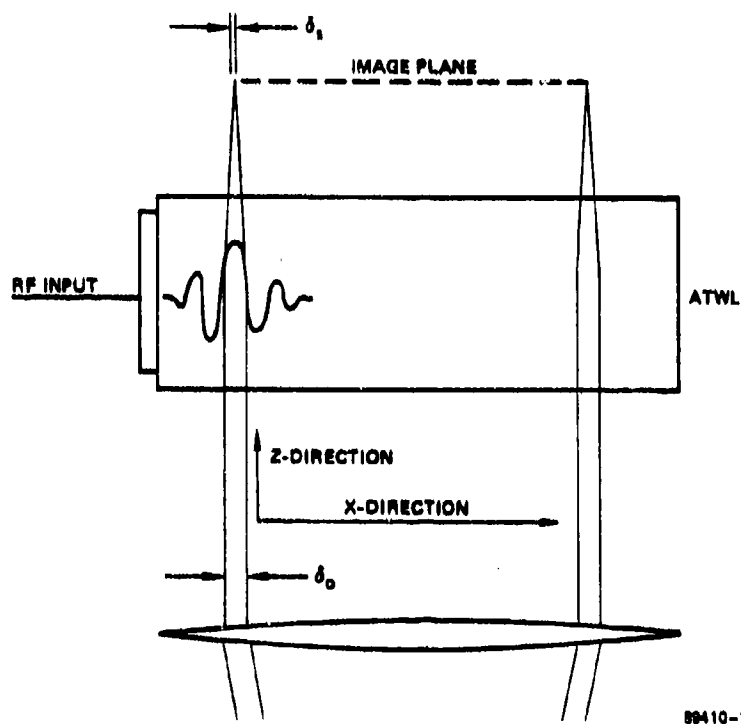


Figure 2.1-3. Acoustic Travelling Wave Lens

AOBD output beam through the positive compressive region of the traveling acoustic strain wave, which acts as a converging lens due to the approximately quadratic refractive index profile. An elastic strain wave of wavelength Λ propagates in the X-direction. A light beam propagates parallel to the acoustic wavefronts in the

Z-direction. The width of the incident light beam is δ_0 and the beam is focused to a spot size δ_s by the refractive index variation associated with the strain wave. The scan rate of the input spot from the AOBD and the acoustic propagation velocity in the ATWL, v , must be carefully matched to ensure proper tracking of the travelling acoustic lens.

The acoustic traveling wave lens is generated by an acoustic pressure wave that is launched along the axis of the acoustic cell by a piezoelectric transducer. The central portion of a positive half cycle of this pressure wave produces a one-dimensional refractive index profile which affects an incident light beam in much the same manner as a cylindrical lens. Hence, the net effect is the production of a small cylindrical lens that travels along the axis of the ATWL cell at a velocity equal to the acoustic velocity in the acousto-optic material. As the light beam passes through this region of the ATWL cell, it is focused to a size δ_s at the image plane as depicted in Figure 2.1-3. Recall that the beam waist upon entering the ATWL cell is δ_0 . Thus, a gain parameter G is defined by the equation

$$G = \delta_0 / \delta_s \quad (2.1-1)$$

Gains as high as 40 have been achieved in existing ATWL's.

The appropriate drive signal for the AOBD is a function whose frequency is changing linearly with time. This signal is referred to as a linear frequency chirp. The RF source used for an AOBD driver is a voltage-controlled oscillator (VCO), but the frequency versus voltage transfer function of a typical VCO is not linear enough to satisfy the above requirement. It is therefore necessary to generate a voltage tuning curve that will compensate for the VCO nonlinearities and produce a linear RF chirp at the VCO output.

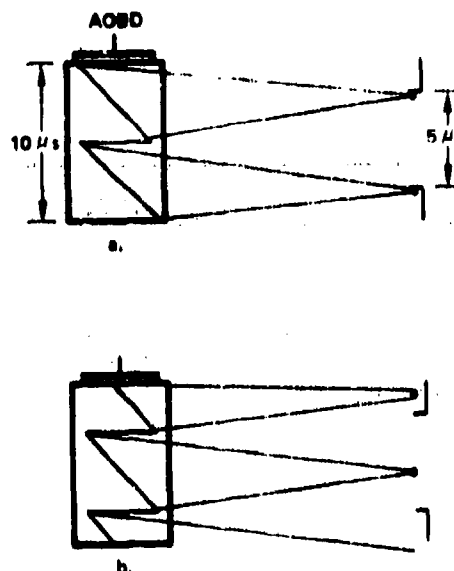
To meet the requirement of 98 percent duty cycle, certain special features need to be incorporated into the AOBD design. Of prime importance in the design of an AOBD is the time-bandwidth product TB , where T is the cell fill time (cell length divided by acoustic velocity) and B is the frequency range of the chirp. This product defines the output resolution capability of an AOBD. In a conventional lower duty cycle system, a chirp signal is fed into the AOBD and allowed to propagate into the cell at the acoustic velocity until the optical aperture is completely filled. At this time active scanning begins and continues until the chirp is completed and a new chirp cycle is initiated. The time required for the cell to fill is nonusable and reduces the device duty cycle.

One technique for reducing the fill time loss and increasing the duty cycle is to shorten the cell length. In this manner, the fill time could be reduced until a chirp length of $0.1 \mu s$ yields a duty cycle of 98 percent. This, however, increases the bandwidth requirements of the chirp to 1 GHz. An alternative approach is to lengthen the cell to an acoustic propagation length of $10\mu s$.

By introducing one $5 \mu s$ chirp every $5 \mu s$, one continuous chirp cycle is present in the cell at all times, as shown in Figure 2.1-4.

As the chirp propagates within the cell, the spot associated with it also moves. In addition to the well defined spot associated with the full chirp cycle, there will be additional poorly defined spots generated by the partial chirp cycles also present. By blocking the poorly defined spots, we obtain a high repetition rate, high duty cycle scan which can be used as the input to the ATWL.

There are several ways to implement the Y-scan. The slow scanning speed in the Y-direction, coupled with the changing directions of the optical rays due to the X-scan seems to favor a large-area, large-angle scanning system such as a rotating mirror spinner. A high resolution AOBD approach also appears feasible,



TRAVELING CHIRP AOB DEVICE

- a. THE START AND END OF SCAN
- b. MID-SCAN

10140 1

Figure 2.1-4. Travelling ChirpAOBD

but it is more difficult to implement an optical system to shape and direct the X-scanning optical beam through the high resolution Y-scan AOB.

A rotating mirror scanner (spinner) is a multifaceted mirror which rotates at a constant velocity about a fixed axis. In order to use a spinner in a high duty cycle system, a technique similar to that shown in Figure 2.1-5 would be used, in which the input beam is expanded to over-illuminate the spinner facets by a factor of two. In this way, one full facet is in the beam at all times and, as it proceeds through its scan, the following facet moves into the beam. Upon completion of a scan, the trailing facet has moved fully into the beam and immediately begins scanning, yielding a 100 percent duty cycle.

The output of the X-direction beam scanner is used as the input to the Y-direction scanner. This input is in the form of a row of focused circular

spots. The spots expand until they reach twice the facet size and are collimated by the transform lens, which converts the spatial displacement of the spots into an angular displacement of the collimated beams. By locating the active spinner facet in the transform plane at the region through which the transformed spots pass (the pupil), the light is directed through a flat-field scanning lens which reimages the spots into a two-dimensional scanned array in the image plane.

In the following sections we will discuss a design of an AOM, AOBD, ATWL, a tracking lens, and a trade-off design for the slow Y-scan approaches.

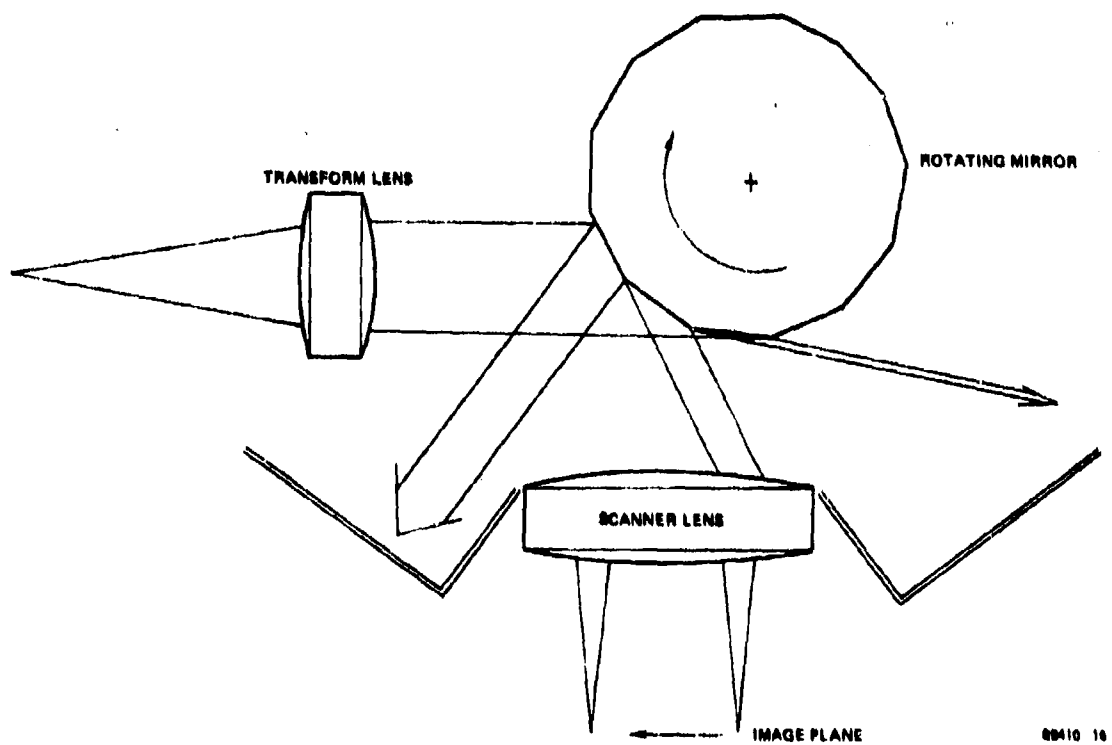


Figure 2.1-5. Rotating Mirror Y-Scan

2.2 AOM Design

The maximum AOM performance is achieved by the careful selection of acousto-optic materials, piezoelectric transducer parameters, and optical beam size. To achieve the required rise time and modulation bandwidth, the piezoelectric transducer parameters are traded off against various optical geometries for the available acousto-optic materials.

The strain pattern associated with the acoustic waves in a material causes refractive index variations in the form of a grating. The amount of phase change, due to the acoustic wave, depends on the amplitude of the strain. Light incident on the grating is diffracted by the Bragg effect if the angle of incidence of light is at the Bragg angle to the acoustic beam. The light diffraction efficiency η , which is the ratio of the diffracted to incident light intensity, can be obtained as:⁵

$$\eta = \sin^2 \left[\pi M_2 \sqrt{(L/H) P_{ac} / 2 \lambda_0^2} \right] \quad (2.2-1)$$

where M_2 is the acousto-optic figure of merit of the material, L/H is the length to height ratio of the acoustic beam cross-section, P_{ac} is the acoustic power and λ_0 is the free space wavelength of light. If the incident light is at an angle other than the Bragg angle, η decreases rapidly as $(\sin x/x)^2$ where $x = \Delta K \cdot L/2$, for the phase mismatch ΔK and interaction length L . Thus, the bandwidth of an AOM or AOBD is limited due to the $(\sin x/x)^2$ dependence of η .

In the scanner system, the input analog signal $m(t)$ modulates an RF source to drive an AOM. The diffracted light intensity I_1 from the AOM is given by

$$I_1 = I_0 \sin^2 a [1 + b m(t)] \quad (2.2-2)$$

where I_0 is the incidence light intensity; a is a constant which depends on the acousto-optic material parameters, wavelength of light and average acoustic power

level (usually $\alpha = \pi/4$ for the best linearity of the AOM); b is the depth of modulation. The diffracted light from the AOM emerges at an angle $2\theta_B$ from the incident light due to Bragg effect. The Bragg angle θ_B is given by

$$\theta_B = \lambda_0/2\Lambda , \quad (2.2-3)$$

where $\Lambda = v/f$ is the acoustic wavelength at frequency f . The function of the AOM is to modulate light in response to the signal; the rise time t_r of the diffracted light, which is related to the acoustic transit time for the optical beam size d , is selected to be as small as possible. The rise time t_r of the AOM is related to the optical beam size d (Gaussian beam diameter $1/e^2$ power points) by

$$t_r = d/1.5 v , \quad (2.2-4)$$

where v is the acoustic velocity. The rise time may also be limited by the piezoelectric transducer bandwidth or the acousto-optic interaction bandwidth due to the Bragg effect. The acousto-optic interaction bandwidth Δf is related to the rise time by

$$\Delta f = 0.5/t_r . \quad (2.2-5)$$

The dominant factor for this bandwidth is the interaction length L which can be expressed as

$$L = \frac{2n\Lambda_0^2}{\lambda_0} \cdot \frac{f_0}{\Delta f} , \quad (2.2-6)$$

where Λ_0 is the acoustic wavelength at the center frequency f_0 and n is the refractive index of the material.

The piezoelectric transducer bandwidth is primarily determined by the transducer material. The bonding technique used for attaching the transducer to the acousto-optic material also affects the transducer bandwidth. We use LiNbO_3 piezoelectric material and an indium-gold vacuum bond to optimize the transducer bandwidth to near the theoretical limit.

In the optical layout shown in Figure 2.2-1 a lens preceding the AOM transforms the laser beam from a 3 mm diameter Gaussian beam into a sharply focused beam at the center of the acoustic beam in the AOM. Laser beam focusing in the AOM is necessary to achieve the specified modulation rate of 100 MHz. The diffracted light from the AOM can follow the fast modulation $m(t)$, only if the acoustic transit time across the optic beam is small.

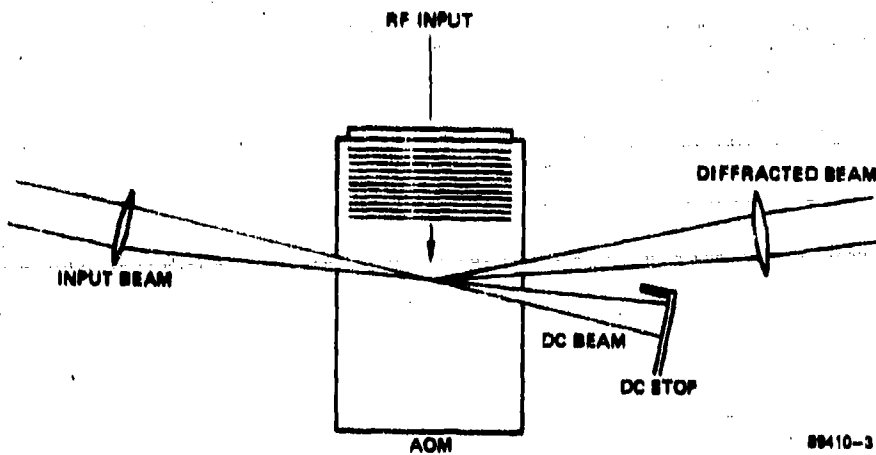


Figure 2.2-1. Acousto-Optic Modulator

The diffracted beam from the AOM is separated from the undiffracted beam which is blocked by a stop. The highly focused diffracted beam emerging from the AOM expands to the size of the AOBD cell. Since the height of the transducer for the AOBD cannot be more than a few millimeters, a cylindrical lens reduces the expansion of the diffracted beam from the AOM to the vertical size of the AOBD transducer. A long focal length spherical lens collimates the beam as necessary for the AOBD input.

After selecting the material for the AOM, the design parameters for the transducer are determined. From Equation (2.2-4) we find that a 5 ns rise time

for the optical flux corresponds to an optical beam diameter of approximately 30 μm . The acoustic beam height H , which equals the transducer height, must be just sufficient to contain the optical beam. The length of the transducer and the center frequency must be such that the acousto-optic interaction bandwidth and the excitation bandwidth of the transducer is sufficiently large to achieve the desired rise time for the pulse. The combination of the transducer and the acousto-optic interaction bandwidth reduces the overall bandwidth of the diffracted light. For that reason, a 3 dB bandwidth of approximately 150 MHz would be more appropriate.

A transducer can occasionally be fabricated to have the 3 dB conversion bandwidth over a frequency range that is 60 percent of the center frequency. However, our experience with TeO_2 indicates that 40 percent of the center frequency value is more easily obtainable. The 150 MHz bandwidth corresponds to a center frequency of the AOM transducer of $f_0 = 150/0.4 = 375 \text{ MHz}$. The length L of the acoustic transducer can be calculated from Equation (2.2-6) for the acousto-optic interaction bandwidth.

Substituting the value for $n \approx 2.3$ as the average of n_e and n_o of TeO_2 and $\lambda_0 = 514.5 \text{ nm}$ in Equation (2.2-6), we have $L = 2.8 \text{ mm}$. Since the height of the electrode $H_1 = 30 \mu\text{m}$ is too small for alignment and wire bonding, we increase this height to $H_1 = 100 \mu\text{m}$, giving $L/H_1 = 25$. The optical diffraction efficiency η can be calculated from Equation (2.2-1). The theoretical value of η is calculated to be 5.9 percent per 10 mW of drive power. If a 5 dB conversion loss is assumed for the transducer, we find that 0.75 W of drive power is sufficient to diffract 90 percent of the incident light. This completes the AOM design; although we did not propose to include the AOM fabrication as part of this study, we included its design to illustrate how the theory of acousto-optic devices is applied. We summarize, in Table 2.2, the important AOM parameters.

Figure 2.2-2 shows a photograph of the AOM used in the breadboard system. The protective cover has been removed so that the device can be seen.

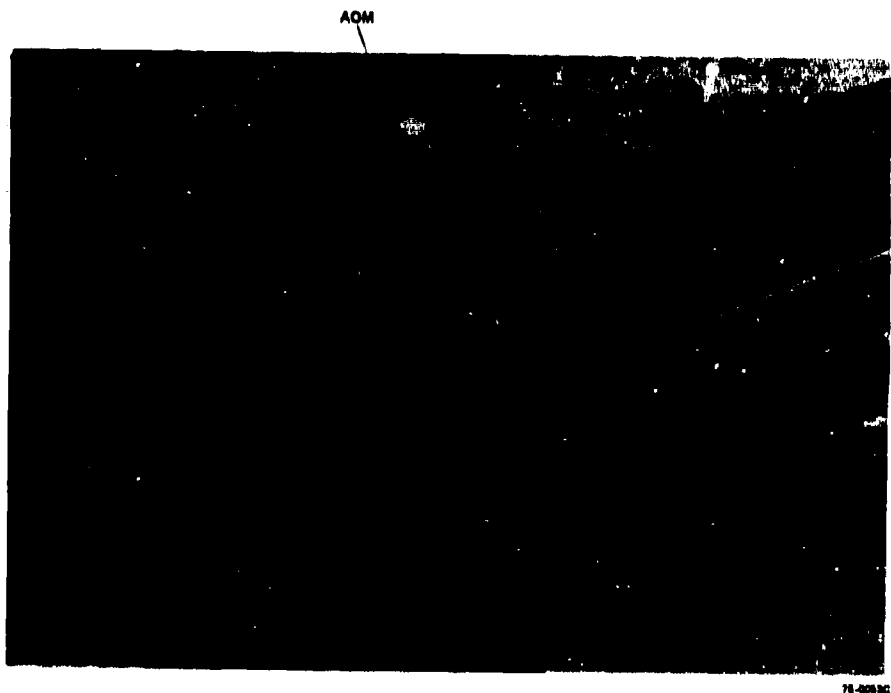


Figure 2.2-2. Photograph of AOM Used in Breadboard System

The device is a part of the Harris owned equipment, and was not designed and fabricated on this program; however it was made available for use in the breadboard setup.

2.3 AOBD Design

The design of the AOBD consists of selecting AO materials, transducer parameters, and optical geometries to achieve the number of spots and scan times required. Special consideration of the acoustic attenuation and the acoustic diffraction spreading is required in designing the AOBD, because of the relatively long interaction lengths and high bandwidths that are necessary to achieve the required resolution. A nearly 100 percent duty cycle is necessary for the present

Table 2.2. AOM Design Parameters

Material	TeO₂	
Optical Beam Diameter	30	μm
Transit Time	7.5	ns
Rise Time	5	ns
Center Frequency	375	MHz
Acoustic Bandwidth	150	MHz
Transducer Height	100	μm
Transducer Length	2.5	mm
Conversion Loss	5	dB
Acousto-Optic Bandwidth	150	MHz
Acousto-Optic Q	27.6	
Bragg Angle (external)	5.25	degrees
Diffraction Efficiency	.59	%/mW
Diffracted Fraction for 0.75 W	90	%
(5 dB conversion loss)		
Bias level for the best linearity	50	%

system; therefore, insufficient time is available to fill the AOBD cell then scan. For this reason, the AOBD cell size is increased and is operated in the traveling chirp mode with two identical AOBD's providing alternate scans.

The function of the AOBD is to diffract light into as many resolvable spots as necessary for the given task. The number of resolvable spots of an AOBD can be increased by either increasing the transducer bandwidth so that light can be diffracted over larger angles as determined by Equation (2.2-3), or by increasing the aperture of the AOBD. Increasing the transducer bandwidth requires a higher operating frequency and a lower interaction length L. The lower value of L means a lower diffraction efficiency for the AOBD as dictated by Equation (2.2-1). The larger aperture implies a longer AOBD cell, where a practical limit on the length may be $l = 10$ to 20 mm, depending on the operating frequency. As the operating frequency is increased the acoustic attenuation in the cell increases as the square of the frequency.

Present state of the art AOBD devices have a maximum number of resolvable spots of about 2,000 with a cell length of about $10 \mu s$ and bandwidths of about 200 MHz. The number of resolvable spots N from an AOBD is given by:

$$N = \frac{\pi}{4} T \cdot B , \quad (2.3-1)$$

where $T = l/v$ is the transit time of the AOBD cell and B is the bandwidth. Equation (2.3-1) is applicable when the chirp rate or the scanning rate is slow. At the 200 kHz line rate, only $5 \mu s$ is available for line scanning. Under such a condition the AOBD operates in a different mode which we call the "traveling chirp mode."

In the traveling chirp mode, a chirp of full bandwidth B fills a fraction C of the AOBD cell having total propagation time T_2 . The chirp

propagates within the cell for the scan time $T = T_2(1 - C)$. From Equation (2.2-3) we can see that the diffraction angle of light is proportional to the acoustic frequency. Therefore, a linear chirp diffracts light such that all rays focus at the same point. The size of the spots formed can be calculated using

$$\delta_c = \frac{4}{\pi} \cdot \frac{v}{B} . \quad (2.3-2)$$

The spot formed by the chirp travels with the chirp. In a scan time $T = T_2(1 - C)$, the spot travels a distance vT providing a number of resolvable spots, N , in a scan given by

$$N = \frac{\pi}{4} T_2 (1 - C) B . \quad (2.3-3)$$

Since only a fraction C of the total illumination of the AOBD is available for use, it is desirable that C be as large as possible. A value of C less than $1/3$ would be impractical, resulting in a considerable loss of available light.

A commonly used parameter for the acousto-optic interaction is acousto-optic Q defined as

$$Q = \frac{2\pi\lambda_0 L}{n\Lambda^2} . \quad (2.3-4)$$

The significance of Q is that a value of $Q \gtrsim 4\pi$ means that most of the light will diffract into a single order, while $Q \gtrsim \pi$ means that a number of higher orders are diffracted. In the design we must set $Q \gtrsim 4\pi$ so that negligible light is diffracted into higher order spots.

The ATWL for this application reduces the spot size by a factor of 10, therefore, an AOBD must have the capability to produce at least 100 resolvable spots in a scan time of $5\mu s$. To keep the light loss as small as possible, C in Equation (2.3-3) is set at $1/2$, $T_2 = 10\mu s$, and $T_1 = 5\mu s$. To produce 100 resolvable spots, the required bandwidth is 26 MHz. An AOBD with 26 MHz bandwidth can be fabricated using low cost SF-8 glass. A center frequency of 70 MHz is

chosen to produce a reasonably flat scan. The AOBD cell length (for a $10\ \mu s$ delay) is calculated to be about 4 cm long, which is long enough to provide an adequate resolution input to the ATWL cell.

Since the acoustic beam in the AOBD cell is required to maintain its height over the AOBD cell length, we must select the transducer height H_2 large enough so that the acoustic diffraction effect is not severe. A 3 dB acoustic beam spread due to diffraction effect occurs in a propagation distance $L = H_2^2 / \Lambda_0$. For beam spread less than 3 dB in 3.9 cm, we must have $H_2 > 1.48$ mm; we select $H_2 = 1.5$ mm. A larger value of H_2 can be selected but at the expense of the diffraction efficiency. From Equation (2.2-1), we estimate the diffraction efficiency of the AOBD having $L_2/H_2 = 20$ to be 23.5 percent/100 mW of drive power. If a 3 dB conversion loss is assumed for the transducer, approximately 2 W of RF drive power will theoretically diffract 100 percent of the incident light within the aperture. The design parameters of the AOBD are summarized in Table 2.3.

Table 2.3. AOBD Design Parameters

<u>Material</u>	<u>SF-8 Glass</u>	
Optical Beam Height	1.0	mm
Optical Beamwidth	4.0	cm
Center Frequency	100	MHz
Acoustic Bandwidth	>30	MHz
Transducer Height	1.5	mm
Transducer Length	3	cm
Conversion Loss	3	dB
Total Propagation Time	10	μ s
Effective Propagation Time	5	μ s
Beam Spread (10 μ s Length)	3	dB
Acousto-Optic Q	18.6	
Diffraction Efficiency	23.5	Percent/100 mW
Diffracted Fraction for 2 W	47	Percent
(3 dB Conversion Loss and 50 Percent Aperture Loss)		

2.4 Acoustic Traveling Wave Lens ATWL Design

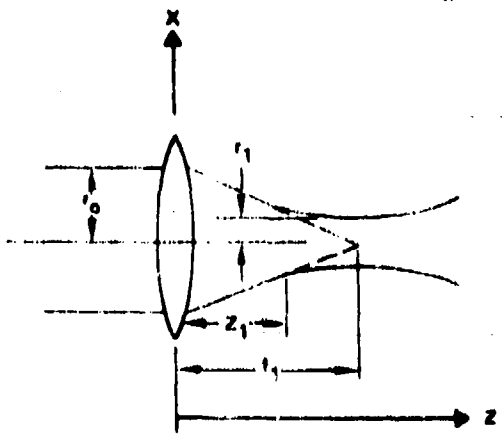
The fundamental idea utilized in increasing the resolution of a beam scanning system is to provide a converging lens whose optical axis always remains aligned with the instantaneous axis of symmetry of the scanned beam. In this way a spatially large information carrying beam can be refocused into a spatially smaller beam in the recording plane where its information can be resolved; the spatial resolution gain is the ratio of the incident beam diameter to the final beam diameter.

A stationary lens, however, is not capable of accomplishing this since the optical axis of a lens and a translating beam can be aligned at only one point. The acoustic traveling wave lens (ATWL) is a device used to generate a traveling converging lens whose optical axis can always align with the axis of a scanning beam. The lens is formed by an acoustically induced refractive index perturbation which causes the positive compressive regions of the acoustic wave to behave as a converging cylindrical lens. The relationship between the acoustic wave and the refractive index perturbations, as well as the properties of the acoustic lens, will be investigated in this section.

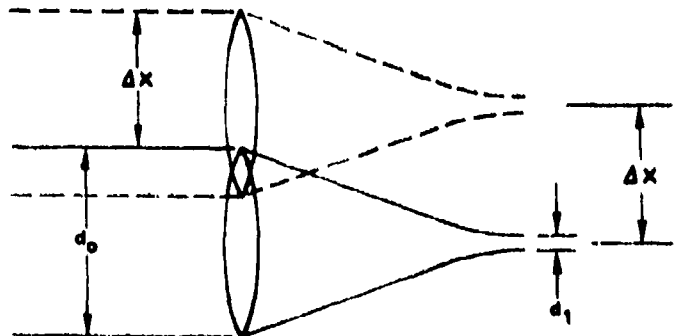
The ATWL provides a one-dimensional scanning lens whose optical axis can be made to align with the low resolution scanning input beam at all points along the scan. The effective lens propagates along the cell at the acoustic velocity associated with the material of the ATWL which refracts the incident light.

Because the ATWL is a one-dimensional scanner, focusing of the optical beam in the scan direction is independent of the orthogonal direction focusing. Hence, the following discussion can be limited to one dimension. Also, the laser beam will be assumed to have a Gaussian distribution and all the optical elements are diffraction limited.

Following the discussion of Foster, et. al.,⁴ consider a collimated Gaussian input beam of wavelength λ with a $1/e^2$ radius r_0 at the input plane $Z = 0$, as shown in Figure 2.4a. This beam is focused by a lens of focal length f_1 to a smaller spot of radius r_1 at $Z = z_1$. The size and position of the spot are given by



a.



b.

Figure 2.4 . Optical Beam Considerations

$$r_1 \approx 1.27 \lambda f_1 / r_0 \quad (2.4-1)$$

$$z_1 \approx f_1 \quad (2.4-2)$$

where the approximations in Equations (2.4-1) and (2.4-2) are good when the final spot is small compared to the input spot.

If a lens is fixed in place and a beam is translated parallel to itself along the X-axis, the focused spot will remain in the same position in the back focal plane of the lens (determined by the angle between the axis of the lens and the beam) but it will vary in angle as it passes through the focus.

However, if the lens can translate along with the scanning beam as shown in Figure 2.4b, then an increase in resolution can be achieved. If the input beam translates one resolution element ($2r_0$) and the lens follows this motion, the output spot will also move a distance $2r_0$. However, in the output plane the spot size is $2r_1$ and a translation of $2r_0$ corresponds to r_0/r_1 resolution elements there, yielding a gain equal to the ratio of spot sizes.

To design a useful system, we must consider the transducer for creating relatively large strain values at frequencies in the low MHz range and the material in which this wave propagates. One of the most important parameters in the design of a traveling acoustic lens device is the maximum refractive index perturbation, Δn , which is produced by the acoustic strain. This index perturbation is related to the strain by

$$\Delta n = \frac{1}{2} \rho s n_0^3 , \quad (2.4-3)$$

where ρ is the acousto-optic coefficient for the material (normally $0.2 < \rho < 0.3$), ϵ is the acoustic strain, and n_0 is the refractive index of the unperturbed material. A useful perturbation results if index variations on the order of 10^{-4} to 10^{-5} are achieved. From Equation (2.4-3) we find that acoustic strains of this same order are also required. These are relatively high strain levels (breaking points of most materials are around 10^{-3}) and achieving them requires relatively high acoustic power density.

The peak change in index of refraction created by a particular drive voltage is given by the following expression:⁴

$$\Delta n_p = \frac{1}{4} \frac{h_{33} E_3 E_3 P n_0^3}{C_{33,3}} , \quad (2.4-4)$$

where h_{33} is the piezoelectric modulus of the transducer material, E_3 is the dielectric permittivity of the transducer material at high frequency, E_3 is the electric field in volts/m, P is the photoelastic constant of the acousto-optic material, and $C_{33,3}$ is the elastic stiffness parameter of the acousto-optic material.

It has been shown⁴ that the focal length of the traveling lens created by this acoustic wave is given by

$$F = \frac{\Lambda}{4} \sqrt{\frac{n_0}{\Delta n_p}} , \quad (2.4-5)$$

where Λ is the acoustic wavelength, n_0 is the static index of refraction of the material, and Δn_p is the peak change in index of refraction created by the acoustic wave.

2.4.1 ATWL Design

The specifications for the ATWL are: 1000-element resolution; $5 \mu s$ active scan time; and SF-59 glass ($n_0 = 1.95$). For a 1000-element resolution, the spot size requirement is:

$$1000 \delta = L , \quad (2.4-6)$$

where $L = v \cdot t$ is the scan length in SF-59 and $v = 3.26 \times 10^9 \mu\text{m/s}$. Thus, the spot size requirement is $\delta = 16.3 \mu\text{m}$. The required refractive index perturbation is:

$$\Delta n_0 = \frac{1}{n_0} \left(\frac{44\lambda}{\delta} \right)^2 = 9.34 \times 10^{-5}, \quad (2.4-7)$$

and

$$\Delta n_{\text{rms}} = \frac{\Delta n}{\sqrt{2}} = 6.6 \times 10^{-5}. \quad (2.4-8)$$

We find that $s_{\text{rms}} = 2\Delta n_{\text{rms}} / pn_0^3$, where p is the elasto-optic coefficient ($p = 0.25$). Substituting $\Delta n_{\text{rms}} = 6.6 \times 10^{-5}$, we find that $s_{\text{rms}} = 7.13 \times 10^{-5}$. The acoustic wavelength Λ is determined by the input AOBD, which has a time bandwidth product ($T \cdot B$) of 100,

$$T \cdot B = \frac{L}{\Lambda/4} \text{ or } \Lambda = \frac{4L}{T \cdot B} = 0.65 \text{ mm}. \quad (2.4-9)$$

Also using $f_0 = v/\Lambda$ to find $f_0 = 5.0 \text{ MHz}$, we see from Equation (2.4-5) that $F = 40.1 \text{ mm}$, which can be obtained with an active transducer interaction length of 35 mm.

The transducer height H required to limit acoustic beam spreading is determined from the equation:

$$\frac{H^2}{\Lambda} = 4L, \quad (2.4-10)$$

so that $H = 8 \text{ mm}$.

In Section 3.2 we discuss the fabrication of and experimentation with the ATWL.

2.5 Lens Design for Tracking of the AOBD/ATWL Scanner

2.5.1 Outline of the Problem

The optical system responsible for tracking the AOBD scan on the image plane is fairly simple in concept, and begins with the lens required to focus the travelling-chirp wavefront from the AOBD into a line along which a spot scans. Based on the AOBD bandwidth, the AOBD can be described as having a resolution of a certain number of spots. With the scanning approach utilized in the present system, the travelling chirp weakly focusses the wavefront illuminating the AOBD and forms a line scan containing this number of resolved spots. If this line scan is used to illuminate an ATWL, the ATWL will focus this scanning beam with its travelling lens. The optical design problem for this system is therefore to cause the AOBD scan to fall on the travelling lens in the ATWL and track its motion exactly with respect to both position and required spot size.

One approach to this design problem would be to directly scan the AOBD line on the ATWL. In this case, however, the typical AOBD focal length is long (as much as 2 meters long for moderate 20-30 MHz bandwidths, depending in part on the AOBD scan aperture utilized). In addition, with such a system there is little of the flexibility for regulating spot size, scan length, and number of spots which is present in a lens tracking system. This method was therefore rejected as impractical for the present problem.

Instead, a two-part optical design was selected to track the AOBD scan on the ATWL. In this concept, a lens L_1 focusses the AOBD scan into a line scan, and a telescope consisting of two lens groups L_2 and L_3 magnifies the scan onto the ATWL. With this approach, exact optical tracking is achievable while retaining complete control over spot size, scan length, and number of resolvable spots in the scanner.

2.5.2 Design Requirements

Before attacking the design itself, some basic design goals have to be set down. The first of these is that the number of spots at the ATWL plane be equal to the number of spots at the AOBD scan plane. Put in another way, what this means is that the ratio of the scan length to the resolvable spot size at the AOBD scan plane matches the requirements at the ATWL. To establish this relationship for the present system, first note that the formula for the number of spots resolved by the AOBD is:

$$N = \frac{\pi}{4} \cdot T \cdot B \quad (2.5-1)$$

where B is the AOBD bandwidth and T is the transmit time of the scan in the AOBD cell. At the ATWL, the required scan length ℓ_2 is given by:

$$\ell_2 = V_2 \cdot T \quad (2.5-2)$$

when V_2 is the acoustic velocity in the ATWL medium and T is the scan transit time again. The required spot size d_2 for optimum illumination of an ATWL lens has been evaluated in previous computer raytrace analysis, yielding a third relationship:

$$d_2 = 0.25 \Lambda \quad (2.5-3)$$

where Λ is the acoustic wavelength in the ATWL. Further, if f_0 is the ATWL drive frequency, a direct function of the system design,

$$V_2 = \Lambda f_0 \quad (2.5-4)$$

combining equations (3) and (4):

$$d_2 = 0.25 \frac{V_2}{f_0} \quad (2.5-5)$$

then the number of spots illuminating the ATWL is:

$$N = \frac{\ell_2}{d_2} = 4 \cdot T \cdot f_0 \quad (2.5-6)$$

Since the number of spots in equations(2.5- 1) and(2.5- 6) must be the same, this means that:

$$\frac{\pi}{4} \cdot T \cdot B = 4 \cdot T \cdot f_0, \text{ or:}$$

$$B = \frac{16}{\pi} \cdot f_0 \quad (2.5- 7)$$

This result shows that there is a fundamental relationship linking the AOBD and the ATWL which affects every part of the system design.

The first of these effects can best be understood by comparing this equation to the fundamental limitations of AOBD's and ATWL. In this system, the final scan resolution is 1000 spots. Because of the limitations of driving the ATWL, the ratio of the illuminating spot diameter to the ATWL-focussed spot diameter is from 10 to 20. Accordingly, the larger the number of spots resolved by the AOBD the better, but since more AOBD spots means a higher AOBD bandwidth, this makes AOBD design more difficult. Also, the higher the bandwidth at the AOBD, the higher the frequency f_0 at the ATWL, meaning smaller values of Λ and smaller spots to be optically resolved at the ATWL. Because of all these interrelationships, a compromise value of $N=100$ spots (for an ATWL gain factor of 10) was selected as the system design goal.

To determine what is necessary to meet this goal, the equations must be worked through from the number of spots to the required ATWL frequency. From Equation(2.5- 1) we have that if $N = 100$ and $T = 5 \mu s$ (required by the system data rate of 1000 spots every 5 μs , or 200 MHz), then $B = 25.46$ MHz. Equation(2.5- 7) then requires that the ATWL frequency be 5 MHz. Since the nearest available ATWL frequency is 4.8 MHz, a result of the resonator design used in this scanner, this was chosen to be the basis for all future calculations. With this value for f_0 , $N = 96$ spots, the required gain factor is 10.41, and the bandwidth of the AOBD is 24.45 MHz.

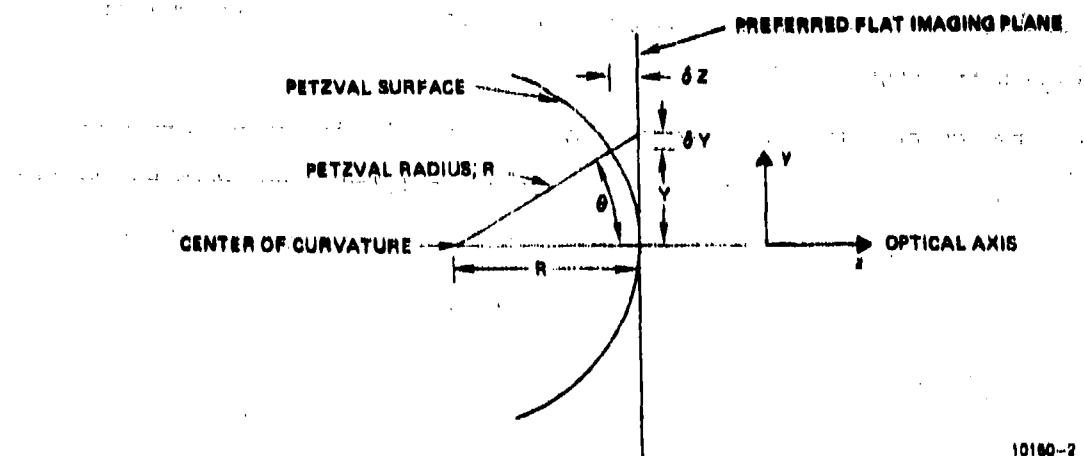
The next design specification to determine is what level of aberration will be tolerated in the optical tracking system. In this case, note that the required spot size is given by Equation 2.5-5. Using SF-59 glass for the ATWL, then, $V_2 = 3.2 \text{ mm}/\mu\text{s}$, and we have that $d_2 = 167 \mu\text{m}$. The allowable degree of spot growth is the result of earlier ATWL analysis, and is given by $\Delta d_2 = 0.04 \Delta$, or $\Delta d_2 = 26.7 \mu\text{m}$ in this example. This amounts to 16 percent spot growth through the system.

The accuracy to which the lens system "tracks" the input scan signal, distortion, is another specification which must be analyzed. One approach would be to use a conventional measure of accuracy, that a scanning spot must be positioned accurately to within 1/10th of an AOBD spot, or to 0.1 percent total AOBD scan accuracy. A second and more accurate approach would be to use the 0.04Δ figure as a level of required accuracy. For the SF-59 ATWL and the transit time $T = 5 \mu\text{s}$, the scan length $\ell_2 = V_2 \cdot T = 16 \text{ mm}$. To track to an accuracy of Δd_2 means that the optical system must produce less than 0.17 percent distortion. As a design goal, then, 0.1 percent of total AOBD scan accuracy is of the proper order of magnitude and will be used throughout this analysis.

Because this is a precision optical system, the phenomenon of apparent distortion as a result of image field curvature will also be important, and for this reason it is the last fundamental consideration for the system. As an approximation of this effect, the geometry of Figure 2.5.2-1 is useful. Here, the Petzval curved field is the actual image field, and the preferred imaging plane represents the ATWL's flat field. In any optical system, if spherical aberration, coma, and astigmatism are small, the image will tend to lie on a curved field known as the Petzval surface. For thin lenses, this Petzval surface will have a radius of curvature R given by the following formula:

$$\frac{1}{R} = \sum_{i=1}^k \frac{1}{f_i n_i} \quad (2.5-8)$$

where f_i is the focal length of the lens with refractive index n_i . In Fig. 2.5.2-1, the impact of this curvature is determined first by noting that



10160-2

Figure 2.5.2-1. Effect of Field Curvature on Image Position

$$\tan \theta = \frac{Y}{R} \quad (2.5-9)$$

From other geometrical considerations, we have that:

$$\frac{\delta z}{R} = (1 - \cos \theta) \quad (2.5-10)$$

and

$$\frac{\delta z}{R} = \frac{\delta Y}{Y} \quad (2.5-11)$$

Combining these three equations, we have that:

$$R = \frac{Y}{(\tan (\cos^{-1} (1 - \frac{\delta Y}{Y})))} \quad (2.5-12)$$

Using $Y = 8$ mm to correspond to the half-width of the ATWL scan aperture and $n = 1.5$ for a typical glass type, the relation between the $\frac{\delta Y}{Y}$ distortion value and the thin lens focal length which will produce this level of distortion has been plotted in Figure 2.5.2-2. The result is that a lens with approximately a

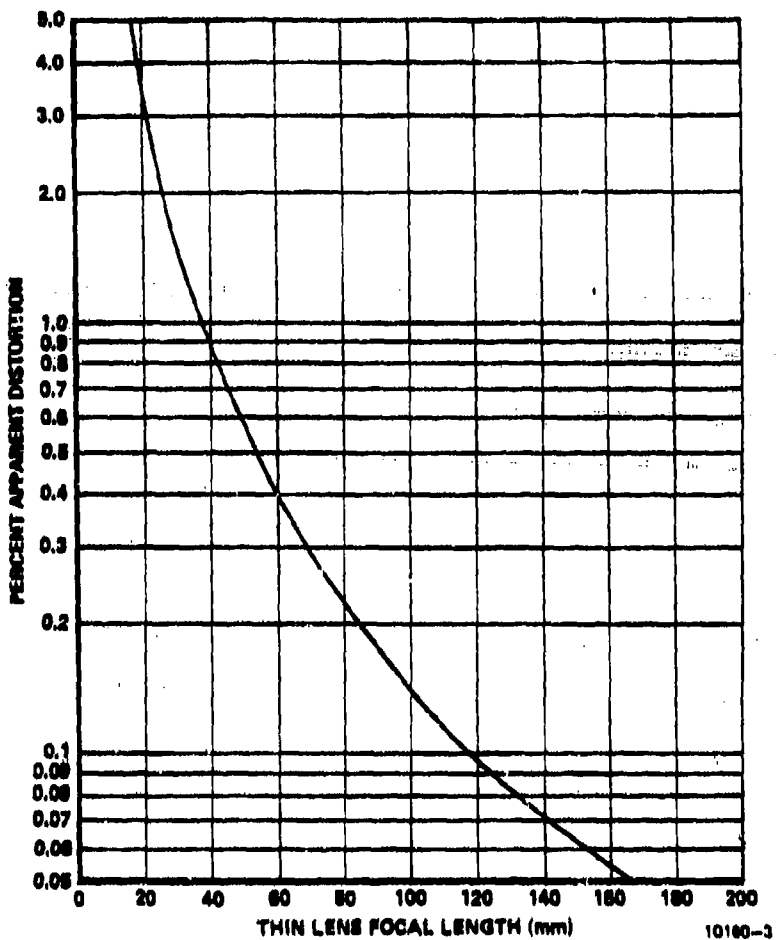


Figure 2.5.2-2. Percent Apparent Distortion Due to Field Curvature
as a Function of Thin Lens Focal Length

119 mm focal length will produce about 0.1 percent apparent distortion from Petzval curvature alone according to this calculation. This worst-case approximation of the field curvature contribution to apparent distortion thus provides a guideline as to the allowable degree of Petzval curvature present in the system. (Note that this also produces a focal plane shift of approximately $0.001 \times R = 178 \mu\text{m}$. Since a Gaussian beam propagates according to the formula⁶

$$w = w_0 \left[1 + \left(\frac{\lambda z}{\pi w_0^2} \right)^2 \right]^{1/2} \quad (2.5-13)$$

where w_0 is the original spot radius, z = the focal shift, λ = the light wavelength, and w = the increased spot size, we have that

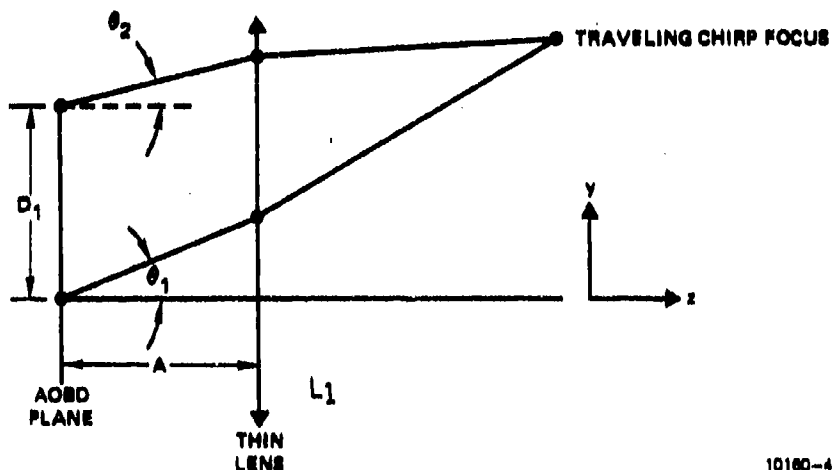
$$w = 1.0000102 w_0$$

for $z = 178 \mu\text{m}$. Depth-of-focus is clearly not a problem in this system.)

The above considerations constitute the specifications for the optical tracking system design.

2.5.3 The AOBD Scan Lens

One of the first considerations for the selection of the lens system L_1 designed to focus the AOBD scan is the scan length. This is important because the longer the scan length L_1 , the lower the required magnification of the scan onto the ATWL. To analyze this problem, consider the geometry of Figure 2.5.3-1. Depicted in this illustration is a thin lens L_1 focussing the



10160-4

Figure 2.5.3-1. Focussing of an AOBD Travelling Chirp By a Thin Lens weakly-convergent beam from the AOBD. D_1 is the optical scan aperture of the AOBD, and θ_1 and θ_2 represent optical rays diffracted by the high and low frequency ends, respectively, of the AOBD's travelling chirp. A is the gap

between the AOBD and the scan lens L_1 .

To begin, the y-heights of the rays at the AOBD are identified:

$$y_2 = y_1 + D_1 \quad (2.5-14)$$

Also: $\theta_1 = \frac{\lambda}{\Omega_1} = \frac{\lambda \gamma_1}{V_1} \quad (2.5-15a)$

and

$$\theta_2 = \frac{\lambda}{\Omega_2} = \frac{\lambda \gamma_2}{V_1} \quad (2.5-15b)$$

Here Λ_1 and Λ_2 are acoustic wavelengths, γ_1 and γ_2 are acoustic frequencies, and V_1 represents the acoustic velocity in the AOBD. Using the relation $y' = y + t \cdot \theta$ we have that the y heights at the lens pupil are:

$$y_1' = y_1 + A \cdot \theta_1, \text{ or}$$

$$y_1' = y_1 + A \cdot \frac{\lambda \gamma_1}{V_1} \quad (2.5-16a)$$

and $y_2' = y_2 + A \cdot \theta_2, \text{ or:}$

$$y_2' = y_1 + D_1 + A \cdot \frac{\lambda \gamma_2}{V_1} \quad (2.5-16b)$$

Further, since $\theta' = \theta - \frac{y'}{f}$ where f is L_1 's focal length (for thin lenses), we have that

$$\theta_1' = \theta_1 - \frac{y_1'}{f}, \text{ or:}$$

$$\theta_1' = \frac{\lambda \gamma_1}{V_1} - \frac{1}{f} \left(y_1 + A \cdot \frac{\lambda \gamma_1}{V_1} \right) \quad 2.5-17a)$$

and $\theta_2' = \theta_2 - \frac{y_2'}{f} = \frac{\lambda \gamma_2}{V_1} - \frac{1}{f} (y_2 + A \cdot \frac{\lambda \gamma_2}{V_1}), \text{ or}$

$$\theta_2' = \frac{\lambda \gamma_2}{V_1} - \frac{1}{f} (y_1 + D_1 + A \cdot \frac{\lambda \gamma_2}{V_1}) \quad (2.5-17b)$$

Now, if we define t as the distance from lens L_1 to the focussed scan plane and y'' is the ray height at this plane, then we have that

$$y'' = y_1' + t \cdot \theta_1' \quad (2.5-18a)$$

and

$$y'' = y_2' + t \cdot \theta_2' \quad (2.5-18b)$$

Solving simultaneously:

$$t = \frac{(y_2' - y_1')}{(\theta_1' - \theta_2')} \quad (2.5-19)$$

Now: $y_2' - y_1' = y_1 + D_1 + A \cdot \frac{\lambda \gamma_2}{V_1} - (y_1 + A \cdot \frac{\lambda \gamma_1}{V_1})$, or

$$y_2' - y_1' = D_1 + \frac{A\lambda}{V_1} \cdot (\gamma_2 - \gamma_1) \quad (2.5-20)$$

Since $B = \gamma_1 - \gamma_2$ we can write this as:

$$y_2' - y_1' = D_1 - \frac{A\lambda B}{V_1} \quad (2.5-21)$$

Similarly, $\theta_1' - \theta_2' = \frac{\lambda \gamma_1}{V_1} - \frac{1}{f} (y_1 + \frac{A\lambda \gamma_1}{V_1})$

$$- \left[\frac{\lambda \gamma_2}{V_1} - \frac{1}{f} \left(y_1 + D_1 + \frac{A\lambda \gamma_2}{V_1} \right) \right] \quad , \text{ or:}$$

$$\theta_1' - \theta_2' = \frac{\lambda}{V_1} \left[\gamma_1 - \gamma_2 \right] - \frac{A\lambda}{fV_1} (\gamma_1 - \gamma_2) + \frac{D_1}{f} \quad , \text{ or:}$$

$$\theta_1' - \theta_2' = \frac{D_1}{f} + \frac{A\lambda B}{V_1} \left[1 - \frac{A}{f} \right] \quad (2.5-22)$$

Combining equations (2.5-19), (2.5-21), and (2.5-22) yields that:

$$t = \frac{\left[D_1 - \frac{A\lambda B}{V_1} \right]}{\frac{D_1}{f} + \left[\frac{\lambda B}{V_1} \cdot \left(1 - \frac{A}{f} \right) \right]} \quad (2.5-23)$$

$y = 0$: To solve for the scan length l_1 , we evaluate equation (2.5-18a) for

$$y'' (y_1 = 0) = A \cdot \frac{\lambda \gamma_1}{V_1} + t \cdot \left[\frac{\lambda \gamma_1}{V_1} \left(1 - \frac{A}{f} \right) \right] \quad (2.5-24)$$

Next, we evaluate Equation (2.5-18a) for $y_1 = D_2$ (where D_2 is the traveling chirp scan distance):

$$y'' (y_1 = D_2) = D_2 + A \cdot \frac{\lambda \gamma_1}{V_1} + t \cdot \left[\frac{\lambda \gamma_1}{V_1} \left(1 - \frac{A}{f} \right) - \frac{D_2}{f} \right] \quad (2.5-25)$$

Subtracting equation (2.5-24) from equation (2.5-25) we have that:

$$l_1 = y'' (y_1 = D_2) - y'' (y_1 = 0), \text{ or:}$$

$$l_1 = D_2 - \frac{D_2}{f} \cdot t, \text{ or:}$$

$$l_1 = D_2 - \frac{D_2}{f} \cdot \left\{ \frac{\left(D_1 - \frac{A\lambda B}{V_1} \right)}{\left(\frac{D_1}{f} + \frac{\lambda B}{V_1} \cdot \left(1 - \frac{A}{f} \right) \right)} \right\} \quad (2.5-26)$$

To interpret these results, the scan length l_1 was calculated using the bandwidth $B = 24.45$ MHz calculated earlier, three values of the lens focal length, $D_1 = D_2 = T \times V_1 = 19.45$ mm (where $T = 5 \mu s$ and V_1 = the acoustic velocity 3.89 mm/ μs in the medium), and a variety of values of A . The calculations are presented in graphical form in Figure 2.5.3-2, and from this it is possible to make several conclusions. First, the scan length increases roughly

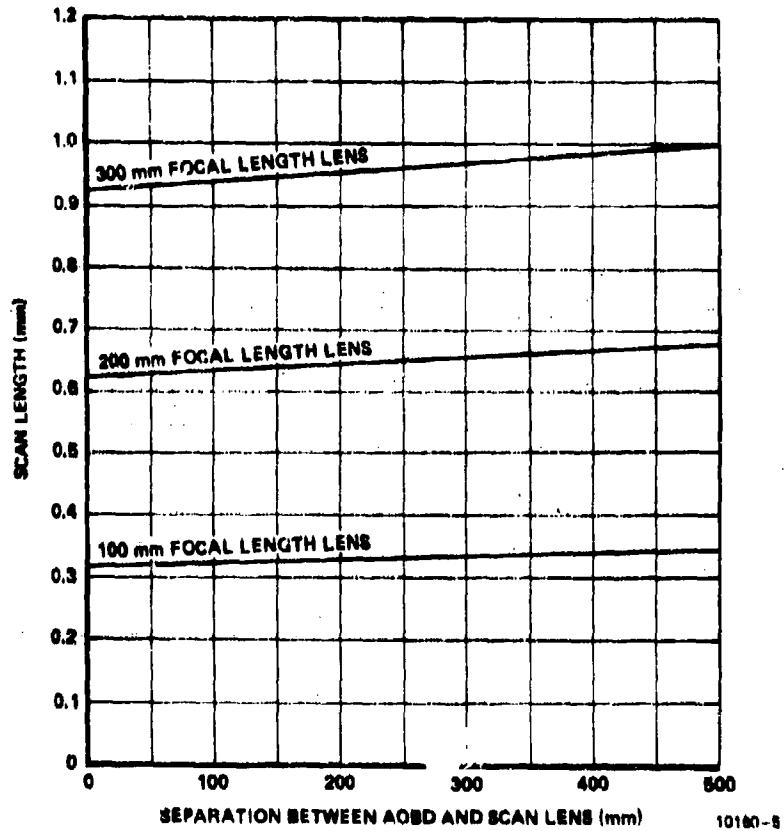


Figure 2.5.3-2. Scan Length as a Function of Separation Between AOBD and Scan Lens

proportional to the focal length for any given position of the lens. Secondly, the value A acts as a kind of "zooming" parameter to adjust the scan length, though it does not vary f_1 more than about 8 percent at most over the 0-500 mm range plotted. Because varying A does not vary f_1 much, it is therefore possible to associate each focal length with an approximate required magnification

of the scan length L_1 to properly match the scan length L_2 of the ATWL. For $A = 25$ mm, for example, a 100 mm lens produces a 0.32 mm scan length and requires a telescope with $\frac{16}{0.32} = 50X$ magnification to scale it properly on the ATWL plane. A 200 mm lens at the same distance produces an 0.63 mm scan length and requires a 25.4X telescope. A 300 mm lens produces an 0.93 mm scan length and requires only a 17.2X magnification to scale the scan properly on the ATWL. In most lens systems of this degree of distortion correction, the smaller the required magnification in the telescope, the better. In addition, with a lower magnification, the actual telescope length can be shortened. For these reasons, L_1 's focal length was selected to be 300 mm.

With the focal length selected, the required lens resolution, acceptable degree of aberration, and allowable distortion must be compared against available lens designs for L_1 . To address the first of these, the required lens resolution is found by calculating the AOBD spot size. The scan length is $L_1 = 0.93$ mm and there are 96 AOBD spots in that scan, for a net spot diameter of $\frac{0.93}{96} = 9.69 \mu\text{m}$. The spot size resolved by L_1 is given by the following equation for single-Rayleigh spots:

$$d_1 = \frac{f}{D_2} \cdot \lambda \quad (2.5-27)$$

where f is the lens focal length, D_2 the input scan aperture, and λ the illuminating wavelength. With $D_2 = 19.45$ mm as before, $\lambda = 0.5145 \mu\text{m}$, and $f = 300$ mm, we have that $d_1 = 7.94 \mu\text{m}$ as resolved by the lens. The 300 mm focal length is therefore just below acceptable limits to match the lens resolution to the AOBD resolution.

Next, to establish the degree of distortion in a typical lens, a computer raytrace of a simple biconvex 300 mm lens was carried out using the 24.45

MHz bandwidth and the $D_2 = 19.45$ mm aperture as inputs to the program. This paraxial analysis established that even this simple a lens produces even less than 0.01 percent distortion, so distortion is not a problem.

To correct for aberrations with a simple lens is not this straightforward. Because of the large aperture utilized on the lens, spherical aberration is extremely large with simple optics used for L_1 , amounting to over 100 percent spot growth without special correction. For this reason, a special computer-optimized achromat consisting of a cemented biconvex and meniscus lens pair was selected to eliminate the aberration problem. According to the manufacturer, Melles Griot, with this lens (No. 01-LAO-255), spot growth is less than 8 percent over a 50° image field from the center to the edge, which puts this within acceptable limits as far as aberrations are concerned. This selection then specifies the first lens group L_1 of the optical tracking system.

2.5.4 The Telescope System

With the 300 mm lens chosen for L_1 , the next stage is the design of the relay optics to magnify the AOBD scan up to match the ATWL scan length. As has been discussed before, with a 25 mm gap between the AOBD and lens L_1 the scan length f_1 is 0.93 mm. This means that a 17.2X telescope is needed to image this scan on the ATWL.

To carry out the design, initially a two-element design was evaluated by paraxial computer raytrace analysis of surface contributions to aberration. Unfortunately, such simple telescope designs could not achieve the required levels of aberration and distortion, so a more complicated design approach was initiated. In this approach, the telescope was configured in a modified double-Gauss layout. This lens form, designed for low distortion at field angles up to 25°, consists of two positive focal length groupings, each of which includes two positive singlets and a negative element for field curvature

correction. Generally, the two lens groupings are symmetrical in shape and layout, with the two sides scaled to yield the proper system magnification. Various modifications of this layout were evaluated in an extensive computer analysis of system, in which each lens grouping was first optimized with respect to aberrations and distortion and then assembled into the proper telescope configuration. In addition, because of the flexibility of magnifying up with lens L_1 to compensate for moderate amounts of distortion in the system, the distortion specification for the telescope was relaxed in favor of meeting the aberration requirement.

The result of this effort in design is depicted in Figure 2.5.4-1. The lens group L_2 includes two biconvex 40 mm lenses and one bi-concave -25 mm focal

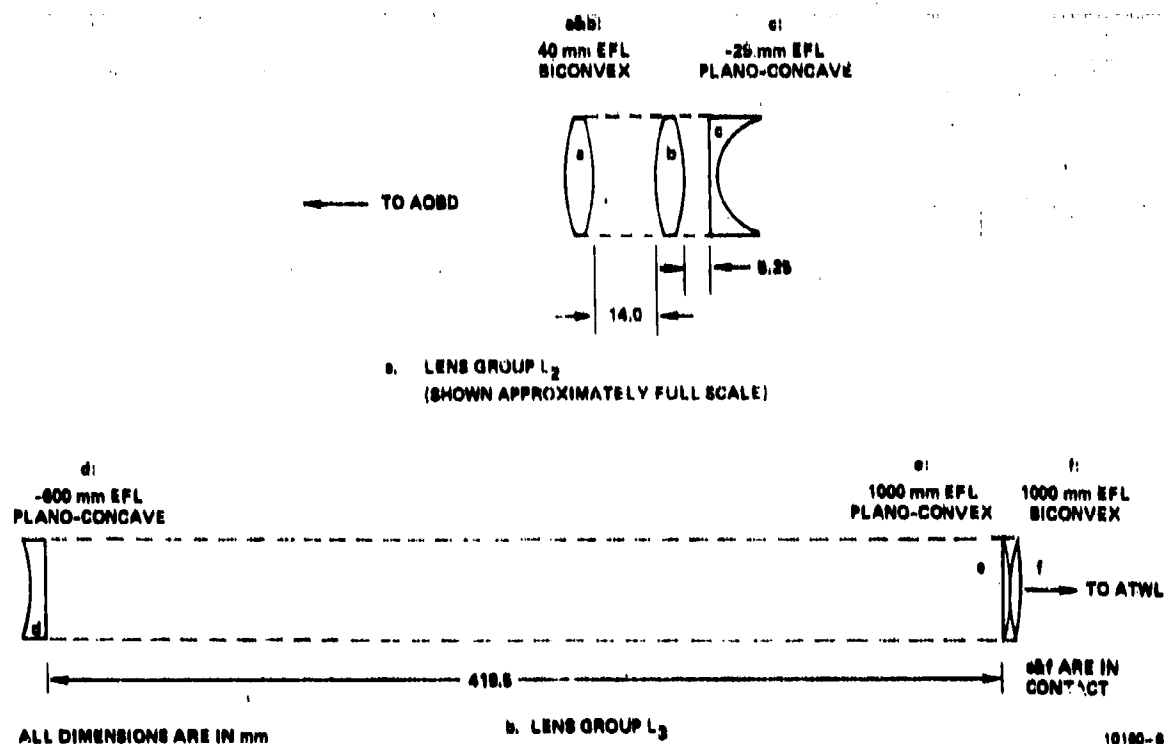
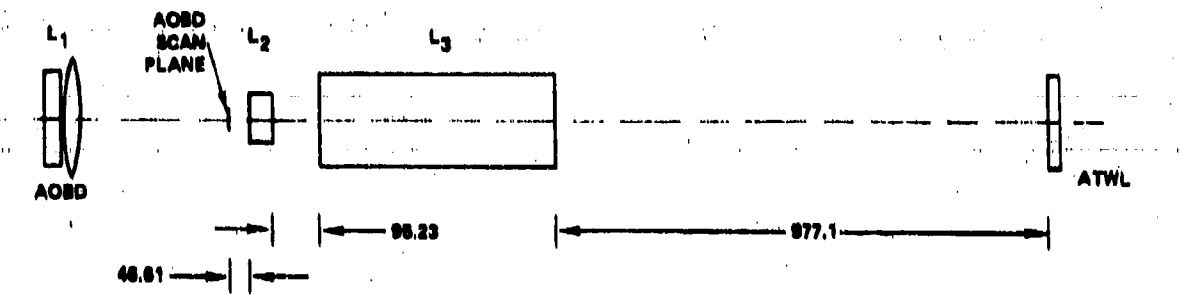


Figure 2.5.4-1. The Two Lens Groups of the Telescope

length planoconcave; its focal length is approximately 33.34 mm. The lens group L_3 includes a 1000 mm focal length biconvex element, a 1000 mm focal length planoconvex element for spherical aberration correction, and a -600 mm focal length planoconcave element for field curvature correction. The focal length of L_3 is approximately 573.5 mm, exactly the 17.2X magnification of L_2 's focal length. With this system assembled as pictured in Figure 2.5.4-2, with the two negative focal length elements facing each other, paraxial analysis of the lens revealed that the L_1 scan is imaged onto the ATWL with a net distortion of



ALL DIMENSIONS ARE IN mm

10180-7

Figure 2.5.4-2. The Optical Tracking System

approximately -0.26 percent, only 0.09 percent more than allowable by strictly considering the aberration specifications alone. The net aberration of the extreme end of the field includes a $-0.66 \mu\text{m}$ spherical aberration contribution, a $+0.88 \mu\text{m}$ coma contribution, and a $-4.5 \mu\text{m}$ astigmatic contribution, amounting to less than 3 percent total spot growth. The Petzval radius of curvature, summed from surface contributions, was found to be 131 mm for this system; this corresponds to a maximum additional apparent distortion of approximately -0.19 percent in the worst case.

To accommodate this estimated $-0.26 - 0.19 = -0.45$ percent distortion, lens L_1 must be moved further away from the AOBD to increase the size of its scan by a factor of 1.0045. This means that $d_1 = 0.93 \times 1.0045 = 0.934$ mm. The exact movement of the lens should be determined experimentally (since focal lengths will be altered as much as 5 percent from these calculated values because of manufacturer's tolerances), but the order of magnitude of the required movement is important to determine at this point. Fortunately, the plot of lens L_1 's "zooming" ability in Figure 2.5.3-2 shows that the required growth of the spot involves motion of an estimated 50 mm away from the AOBD, for a net AOBD-to-lens- L_1 gap of approximately 75 mm. This is a coarse enough movement to make distortion compensation to an accuracy of 0.1 percent relatively easy.

As for more significant alterations of the system, the telescope does have a certain degree of flexibility. During analysis, it was found that changing the spacing between the negative lens and the positive lens pair effectively regulated focal length in each lens group without substantially changing the group distortion contribution. Distortion can be regulated to an extent by adjusting the positive element spacing, if necessary.

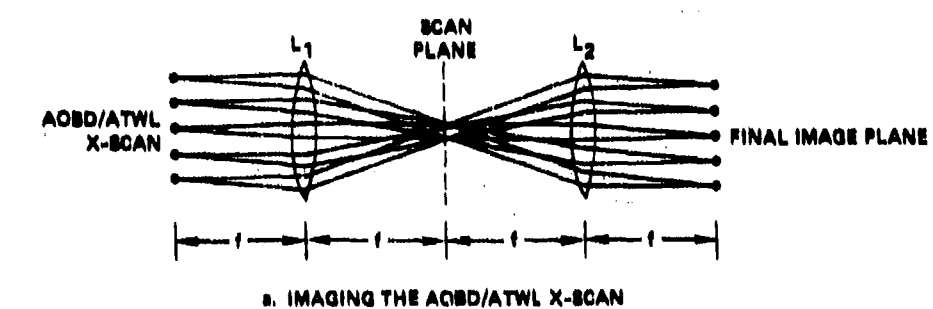
The resulting L_1 , L_2 , and L_3 lens system, pictured in Figure 2.5.4-2, therefore meets all the required system specifications for optical tracking of the AOBD scan onto the ATWI.

2.6 Design Trade-Offs for Y-Scan Approaches

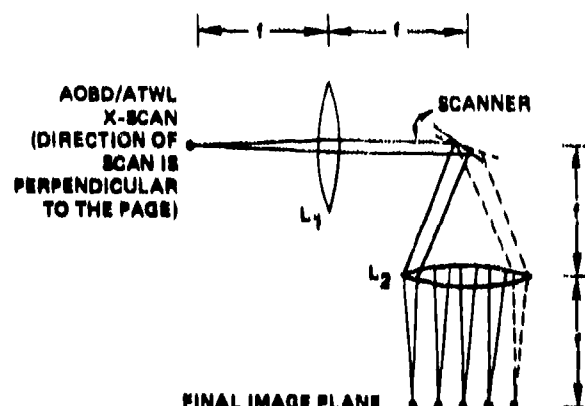
2.6.1 Pre-objective Scanning

In order to take the AOB/ATWL 1000 spot scan and properly scan it perpendicular to its long dimension (effectively recording a square 1000 x 1000 spot matrix), two conditions must be met simultaneously by the optical system involved. The first of these is that the scan lens have the necessary f-number to focus the 16 mm long 1000-spot scan, and the second is that the optics maintain the integrity of the AOB/ATWL X-scan. This means that the optics must include an imaging system, a scanner, and a focussing system, all at the same time.

One way of accomplishing this task involves "pre-objective" scanning. Here a scan lens is placed after a mechanical scanner to focus the Y-scan; it is pictured in Figure 2.6.1-1. Using this method, the AOB/ATWL's 1000-spot X-scan



a. IMAGING THE AOB/ATWL X-SCAN



b. SCANNING IN THE Y-SCAN DIRECTION

10100-8

Figure 2.6.1-1. Optical System for Y-Scanning With a Mechanical Scanner

is imaged to the final recording plane by first forming a Fourier transform of the scan on the scanning mirror (which is in this case one facet of a spinner), and then taking an inverse Fourier transform to recreate the scan. In the Y-scan direction, the line of spots appears to be "on-axis" and is collimated by the first transform lens. The second Fourier transform lens then acts as a scanner lens and focusses the scanning spot across the field.

To implement this concept, since the spots are relatively large (approximately $16 \mu\text{m}$ in diameter) and there are as yet no specific requirements on the linearity of the scan, the main optical problem is that of fitting the spots through the lens apertures. To determine the required lens diameters, first consider the divergence of a spot. If the AOBD/ATWL's spots of diameter d are to be double-Rayleigh resolved by a lens of focal length f and available aperture per spot of D' , the following relationship for resolution at a wavelength λ applies:

$$D' = 2\lambda f/d \quad (2.6-1)$$

For a scan of length ℓ , the necessary lens aperture required to resolve the scan is then given by the scan length plus the required aperture per spot, or:

$$h = \ell + D' = \ell + 2\lambda f/d \quad (2.6-2)$$

Next, this aperture h must be scanned across the scan lens L_2 's aperture. As pictured in Figure 2.6.1-2, what this does is to increase the required aperture of

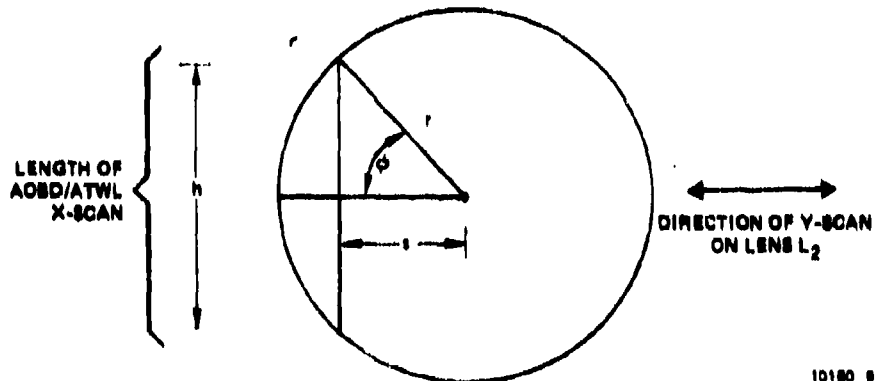


Figure 2.6.1-2. Aperture of Lens L_2

the scan lens, since it must effectively have the aperture for a square $h \times h$ in area; this is because the resolution requirements are the same in both dimensions. From the geometry in the figure, it is clear that:

$$h = 2 \cdot r \cdot \sin \phi \quad (2.6-3)$$

where r is the radius of the lens. Since $\phi = 45^\circ$ if a square recording area is desired, we have that:

$$r = \frac{h}{\sqrt{2}} \quad (2.6-4)$$

The required lens aperture for lens L_2 is therefore given by:

$$D = 2r = \sqrt{2} \cdot \left(\frac{\ell}{f} + 2 \cdot \lambda \cdot \frac{f}{D} \right) \quad (2.6-5)$$

Finally, to guarantee that the lens L_2 scans the proper scan length, the optical scan must subtend an angle of:

$$\theta = \tan^{-1} \left(\frac{\ell}{f} \right) \quad (2.6-6)$$

This then, combined with the requirement that each mirror facet on the scanner has a minimum aperture of $D' \times D'$ to resolve the Fourier transform, completes the optical requirements for the system.

To apply these formulas to the present system requirements, D is calculated first. The 0.5145 μm argon-ion laser line is used for λ , the spot diameter d is 16 μm , and since it is desirable to make f as small as possible let $f = 25\text{mm}$ as a minimum. Then we have from Equation (2.6-1) that $D' = 1.6\text{ mm}$. For a 16 mm scan length ℓ this means that $h = 17.6\text{ mm}$ and $D = 24.9\text{ mm}$. This amounts to a lens L_2 with an f-number of approximately 1, which would require a sophisticated custom design and great expense to fabricate. Since this is not desirable for the present program, the next step is to determine the minimum length quality lens which satisfies the system requirements. Of lenses surveyed from Rolyn Optics, Melles Griot, Klingler Scientific, and a number of other minor

suppliers, the smallest EFL available came in the form of computer-optimized achromatic 80 mm focal length doublets from Melles Griot or Klingler Scientific. For this focal length, $D' = 5.12 \text{ mm}$, so $h = 21.1 \text{ mm}$ and $D = 29.83 \text{ mm}$. This then, requires a minimum facet size of $5.12 \text{ mm} \times 5.12 \text{ mm}$, which is considerably smaller than the $3/4 \text{ inch} \times 11/16 \text{ inch}$ spinner available for this program. To achieve the required 16 mm

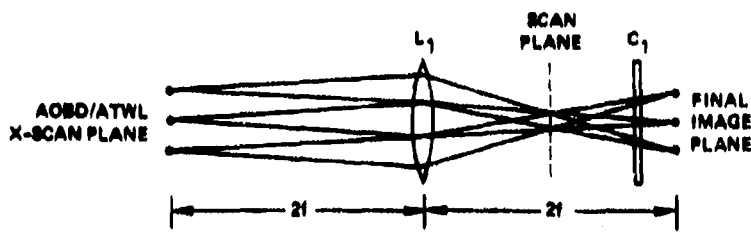
scan, the optical scan angle is $\theta = \tan^{-1} \left(\frac{16 \text{ mm}}{80 \text{ mm}} \right) = 11.3^\circ$, or a mechanical scan angle of 5.65° , again readily achieved since there is a 240° mechanical scan angle available on the spinner. Finally, L_1 and L_2 have been selected as identical lenses for symmetry (to minimize aberrations of the AOBD/ATWL scan imaging), even though L_1 only requires a lens diameter h and is available commercially in smaller focal lengths.

2.6.2 Post - Objective Scanning

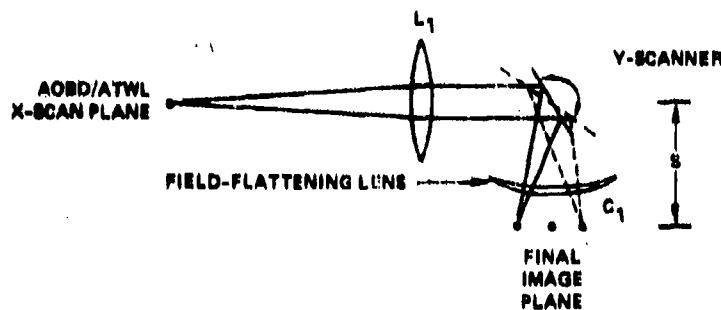
The approach described in the preceding section has certain advantages over other scanning methods. It is simple, relatively compact, and easily configured to produce a telecentric flat-field X-Y scan in the image plane. As for disadvantages, the chief one is that the second lens in the system must act both as a scan lens and a Fourier transform lens. Since the design requirements for focussing and performing a phase-corrected exact optical Fourier transform can be very different, a different approach to mechanical Y-scanning must be considered before making a final design decision. This second approach is known as "post-objective scanning."

In this second optical configuration, L_1 is a conventional imaging lens with focal length f . In the X-Z plane the most compact configuration for imaging the X-scan is to use L_1 , as a 1:1 imaging lens, so that the object and image are each located a distance $2f$ from L_1 . This system is pictured in Figure 2.6.2-1(a). The scan plane is located in the drawing at the Fourier transform plane of L_1 and locates the "minimum scan mirror aperture" position for the mechanical scanner.

In Figure 2.6.2-1(b), the Y-scan configuration is pictured. Lens L_1 focusses the beam, and as the Y-scanner mirror rotates over a full optical angle of 2θ , the scan is relayed over a linear field of length $\lambda = 2 \cdot s \cdot \tan \theta$. As Figure 2.6.2-1 illustrates, depending on the system parameters, it may be necessary to add an anamorphic field flattening lens after the scanner as indicated; this is because the Y-scanner will effectively image the Y-scan on a curved field of a radius s . This field flattening lens is ordinarily a simple meniscus lens (for single-wavelength systems), and compensates for the scan curvature at the edges of the image field.



a. IMAGING THE AOB/ATWL X-SCAN



b. SCANNING IN THE Y-Z PLANE

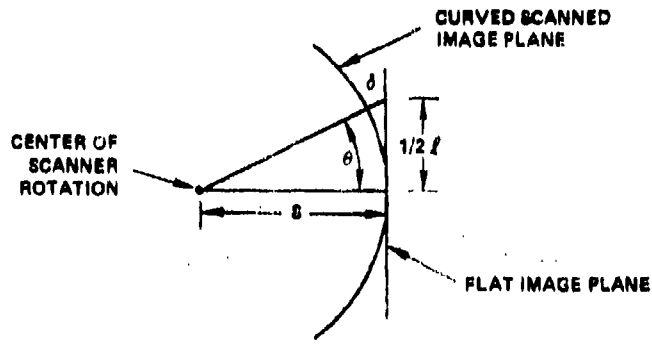
10186-10

Figure 2.6.2-1(a). An Optical System for Cost-Objective Y-Scanning

To illustrate the nature of the design problem for post-objective scanning, only a few key relationships need be derived. In order to achieve a scan of length ℓ at the final image plane, for a scanning mirror a distance s away from the image plane, that mirror must scan over a full optical angle of 2θ where:

$$\theta = \tan^{-1} \left(\frac{\ell}{2s} \right) \quad (2.6-7)$$

As noted before, scanning over an angle θ will produce curvature of the image field; this situation is illustrated in Figure 2.6.2-2. Although the image field will be in focus on-axis, at the perimeter of the field the scan will be a distance δ away from the image plane. Since



10180 11

Figure 2.6.2-2. Curvature of Field in Post-Objective Y-Scanning

$$\cos \theta = \frac{s}{s + \delta} \quad 2.6-8)$$

we have that:

$$\delta = s \left(\frac{1}{\cos \theta} - 1 \right) \quad 2.6-9)$$

Now, if w_0 is the required Gaussian spot radius, and w is the spot radius a distance δ from the focussed spot of radius w_0 , a formula from diffraction theory for spot growth is:

$$w = w_0 \left[1 + \left(\frac{\lambda \delta}{\pi w_0^2} \right)^2 \right]^{\frac{1}{2}} \quad 2.6-10)$$

This then provides a measure of the growth of a focussed spot for a given value of δ for the system.

As a final design requirement, note that because L_1 must have an aperture of :

$$D' = 2\lambda f/d \quad 2.6-11)$$

to resolve each spot a distance f from the spots, at a distance $2f$ from the spots and for a scan length ℓ , lens L_1 must have an aperture of:

$$D'' = \ell + \frac{4\lambda f}{d} \quad (2.6-12)$$

where λ is the system wavelength and d is the required system spot size. Further, to determine the mirror size, note that at the Fourier transform plane the minimum mirror aperture is approximately

$$\frac{1}{2} \cdot \frac{4\lambda f}{d} = \frac{2\lambda f}{d}$$

For a scan plane positioned a distance s' from this Fourier transform plane, then, and positioned with the mirror's center position at 45° to the optical axis of the system, the mirror must have a minimum aperture of:

$$A_x = \frac{2\lambda f}{d} + \frac{s'}{f} \left(\ell + \frac{2\lambda f}{d} \right) \quad (2.6-13)$$

in the x -direction, and

$$A_y = \sqrt{2} \cdot \left(\frac{2\lambda f}{d} \right) \left(1 + \frac{s'}{f} \right) \quad (2.6-14)$$

is the y -direction.

As a design example, let us select a Hastings triplet lens designed for unity (1:1) imaging; this kind of lens can be inexpensively designed for minimum coma and distortion correction, and is therefore a good choice for this application. If the required scan length is 16 mm, the spot size is $d = 16 \mu\text{m}$, and we select $L_1 = 80 \text{ mm}$, then lens L_1 must have an aperture of 26.3 mm for a wavelength $\lambda = 0.5145 \mu\text{m}$. This means it need only operate at $f/3$; such lenses are available commercially. Next, assume we position the scanner at the minimum mirror aperture position, the Fourier transform plane. This means that $s = 80 \text{ mm}$,

and the required scan angle is found from Equation (2.6-7) to be $\theta = 5.70$. From Equation (2.6-3), $\delta = 400 \mu\text{m}$, which corresponds to a 43 percent spot growth when substituted into Equation (2.6-10). If instead $s = 120 \text{ mm}$, placing the scan mirror 40 mm from L_1 , $\theta = 3.89$, and $\delta = 177 \mu\text{m}$; this second case yields only 10 percent spot growth and should be acceptable in most cases. For this second example, since $s' = 40 \text{ mm}$, we have that $A_x = 15.7 \text{ mm}$ and $A_y = 10.9 \text{ mm}$.

The chief advantage of this approach over pre-objective scanning is simplicity and lower overall cost of the optical system. Even if a flat-field corrector is needed, as was not the case in the present system, the optical system will remain less complex than the other system. Nevertheless, it is not telecentric (and would therefore be awkward to use if the spots were to be "read out" after recording by a mirror image of the writing system), and it will not work for image fields with many spots. As the scan angle increases, or the spots grow smaller, the effect of δ on the spot growth will increase and the field flattening lens will have to work even harder. Nevertheless, for image fields up to a few thousand spots this system should be adequate.

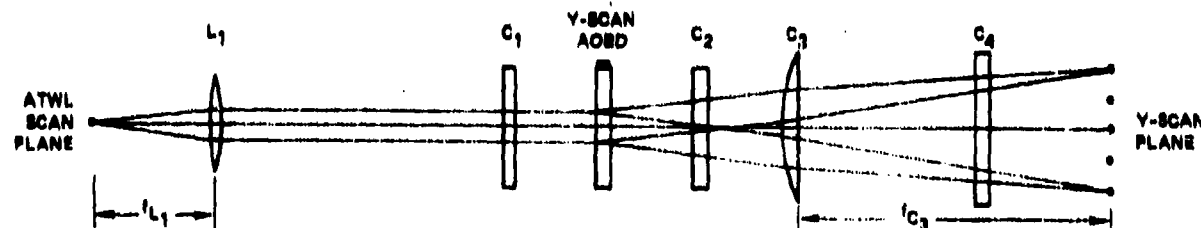
2.6.3 The 1000-Spot AOBD Y-Scanner

A possible alternative to mechanical scanning of the AOBD/ATWL X-scan in the Y-scan direction is to use a 1000 spot AOBD as the second scanner. To do this, first it is necessary to fabricate an AOBD with a useable time-bandwidth product of at least 1000. This in turn forces the AOBD to be either as long as possible (to minimize the bandwidth), to have a large bandwidth (to minimize the length of the AOBD and acoustic attenuation within the cell), or some compromise between these two options. Based on past experience, the practical upper limit on transducer bandwidth for acousto-optic beam deflectors is about 200 MHz. As a result, since the number of AOBD spots is given by:

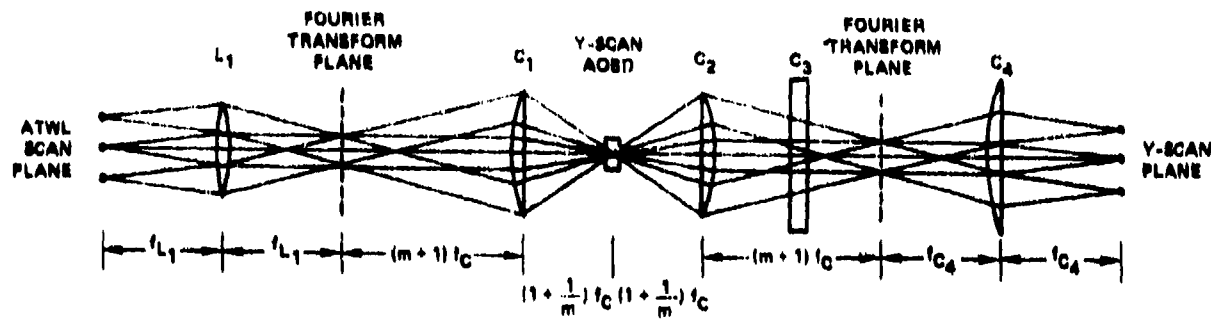
$$N = \frac{\pi}{4} \cdot T \cdot B, \quad (2.6-15)$$

where B is the AOBD bandwidth and T is the transit time of the acoustic beam across the cell, the required cell length is $T = 6.4 \mu s$. With AOBD acoustic velocities ranging between 3 and 4 mm/ μs , this means that the AOBD cell must be between 19.2 and 25.6 mm long. Because of this extremely long length, the AOBD must be selected for high efficiency and low acoustic attenuation. An appropriate material which satisfies these requirements and is commercially available in the proper lengths is lead molybdate, $PbMoO_4$.

With the AOBD selected, the next step is to design the optical system required to produce a quality two-dimensional scan in the image plane. As in the case of mechanical scanning, the optical system must focus the scanning AOBD beam into a 16 mm scan in the Y-direction, while at the same time properly imaging the X-scan onto the Y-scan plane. An optical system which will accomplish both of these goals is pictured in Figure 2.6.3. For the Y-scan dimension, the X-scan



a. THE Y-SCANNER IN THE Y-Z PLANE



b. THE Y-SCANNER IN THE X-Z PLANE

10160. 12

Figure 2.6.3. The AOBD Y-Scan Optical Schematic

appears to scan in and out of the page as pictured in Figure 2.6.3(a). Light from the X-scan spots diverges and, in order to properly illuminate the AOBD, must be collimated by lens L_1 and fill the entire $6.4 \mu s$ aperture of the PbMoO_4 crystal. For a Gaussian spot diameter d in the X-scan, a required AOBD aperture D , and illuminating wavelength λ , the required focal length for lens L_1 is given by:

$$f = \frac{d \cdot D \cdot \pi}{4\lambda} \quad (2.6-16)$$

For PbMoO_4 , the acoustic velocity is $V = 3.6 \text{ mm}/\mu s$, so the required AOBD (and Lens L_1) aperture is $D = V \cdot T = 3.6 \text{ mm}/\mu s \times 6.4 \mu s = 23 \text{ mm}$. With $\lambda = 0.5145 \mu m$ and $d = 16 \mu m$, we therefore have that $f \approx 560 \text{ mm}$.

After the beam is collimated by L_1 , the AOBD scans the beam over an angular range determined by the AOBD bandwidth. For Bragg diffraction from an AOBD with acoustic frequency γ , the diffraction angle is given by:

$$\theta = \frac{\lambda \gamma}{V} \quad (2.6-17)$$

where V is the acoustic velocity in the medium. The total angular scanning angle over a range of frequencies $(\gamma_2 - \gamma_1) = B$ is thus given by:

$$\Delta\theta = \frac{\lambda B}{V} \quad (2.6-18)$$

For a lens of focal length f , as the scan lens focussing this angularly-scanning beam, the resulting scan length is, therefore:

$$L_3 = f \cdot \Delta\theta = \frac{f \lambda B}{V} \quad (2.6-19)$$

Since $L_3 = 16 \text{ mm}$ for this system and $B = 200 \text{ MHz}$, the focal length of lens C_3 is $f = 560 \text{ mm}$. To calculate lens C_3 's f-number, the size of the scanning beam aperture at C_3 is found by first calculating the distance A of lens C_3 from the AOBD. Using the geometry of Figure 2.6.3, this means that:

$$A = \left[\left(2 + m + \frac{1}{m} \right) f_{C_2} + 2 \cdot f_{C_4} \right] - f_{C_3} \quad (2.6-20)$$

Then the aperture D_3 at lens C_3 is given by:

$$D_3 = L_3 \cdot \left(\frac{A}{f_{C_3}} \right) + D \quad (2.6-21)$$

So, finally, we have that:

$$(\#/\#)_{C_3} = \frac{f_{C_3}}{D_3} = \frac{f_{C_3}}{L_3 \cdot \left(\frac{A}{f_{C_3}} \right) + D} \quad (2.6-22)$$

In the X-scan direction pictured in Figure 2.6.3(b), there is a different problem. In order to minimize the RF drive power to the AOBD transducer, the transducer height must be as narrow as possible. Since a typical minimum value for this height is 1.5 mm, this means that while the X-scan is expanded into a 23 mm collimated wavefront in the y-z plane, the X-scan must somehow be condensed into a 1.5 mm aperture in the x-z plane. To do this, first note that spherical lens L_1 produces an exact Fourier transform of the X-scan one focal length from the lens. Then a cylindrical lens C_1 microreduces this transform and images it onto the AOBD's 1.5 mm aperture in this plane. Since at the Fourier transform, the beam is 23 mm in diameter, C_1 must demagnify by a ratio of $m = \frac{23}{1.5} = 15.3$

times. This means that C_1 must be $((1 + m) = 16.3) \cdot f$ away from the Fourier transform plane and $((1 + \frac{1}{m}) = 1.07) \cdot f$ away from the AOBD.

To further specify the lenses in this section of the X-scan imaging system, consider that lens L_1 must have a clear aperture of the scan length plus the $D = 23$ mm beam diameter at the lens, or $16 + 23 = 39$ mm. This makes lens L_1 an f/14 lens. Now, to determine the focal length of lens C_1 , first the scan length ℓ_2 at C_1 is calculated as a function of the scan length ℓ_1 at L_1 from simple geometry:

$$\ell_2 = \ell_1 \left[\frac{(m+1) \cdot f_{C_1}}{f_{L_1}} \right] \quad (2.6-23)$$

The minimum aperture for C_1 is, then, $\ell_2 +$ the size of the beam at the Fourier transform plane. The resulting f-number for lens C_1 is:

$$(f/\#)_{C_1} = \frac{f_{C_1}}{\ell_2 + D} = \frac{f_{C_1}}{\ell_1 \cdot \left[\frac{(m+1) \cdot f_{C_1}}{f_{L_1}} \right] + D} \text{ or:}$$

$$(f/\#)_{C_1} = \left[\left(\frac{\ell_1(m+1)}{f_{L_1}} \right) + \frac{D}{f_{C_1}} \right]^{-1} \quad (2.6-24)$$

Because of the need to specify a lens C , with as large an f-number as possible, next we calculate the maximum f-number for lenses C_1 and C_2 by letting

$f_{C_1} \rightarrow \infty$ in Equation (2.6-24).

Then:

$$f_{C_1 \rightarrow \infty} (f/\#)_{C_1} = \left[\frac{f_{L_1}}{\ell_1(m+1)} \right] \quad (2.6-25)$$

Under the present circumstances, with $f_{L_1} = 560$ mm, $\ell_1 = 16$ mm, and $m = 15.3$, the maximum f-number for C_1 is 2.1. To increase this value, it is necessary to decrease m , since ℓ_1 and f_{L_1} cannot be changed. To do this we must increase the transducer height H , since:

$$m = \frac{D}{H}$$

(2.6-26)

Then, we can solve Equation (2.6-10) for H:

$$H = \frac{D}{\left(\frac{f_{L_1}}{\left(f_{L_1} + \max^* f_{C_1} \right)} - 1 \right)} \quad (2.6-27)$$

Now, if we select a maximum f-number of 4.0, then Equation (2.6-27) yields that $H = 3$ mm. Then, $m = 7.7$, and if we solve Equation (2.6-24) for the focal length required for an actual f-number of 2, we have that $f_{C_1} = 92$ mm.

To determine the impact on the power consumption requirements with $H = 3$ mm, note that a similar AOBD device with a 200 MHz bandwidth and $H = 2$ mm required 100 mW of RF input power to produce a diffraction efficiency of 8 percent. For this case, then, an AOBD Y-scanner would require 1.5 times as much power, or approximately 560 mW of RF drive power for a diffraction efficiency of 30 percent.

On the other side of the AOBD, a cylinder lens C_2 remagnifies the X-scan Fourier transform up to its full size. In order to assure maximum resolution in the image plane, C_2 should be identical to C_1 in design and placed in the system exactly opposite to the way C_1 was placed; this will result in cancellation of key aberrations introduced by the first cylinder lens in front of the AOBD.

The final lens in the X-scan system, C_4 , performs an inverse optical Fourier transform and reimages the X-scan in the final image plane. As the present system is configured, since C_1 and C_2 are identical the scan length ℓ_3 at lens C_4 is given by:

$$\ell_3 = \ell_1 \cdot \frac{f_{C_4}}{f_{L_1}} \quad (2.6-28)$$

Cylindrical lens C_4 therefore requires a clear aperture of $L_3 + D$, and the f/# for lens C_4 is:

$$(f/\#)_{C_4} = \frac{f_{C_4}}{L_3 + D} = \left(\frac{f_{L_1}}{f_{C_4}} + \frac{D}{f_{C_4}} \right)^{-1} \quad (2.6-29)$$

If we choose a minimum f-number of 2.0 for this lens this means that C_4 's focal length is 107 mm, with a clear aperture of approximately 54 mm.

Finally, using this value for f_{C_4} and knowing that $f_{C_2} = 92$ mm, $m = 7.7$, $f_{C_3} = 560$ mm, we can now use Equation (2.6-15) to calculate that $(f/\#)_{C_3} = 14.4$. This is more than large enough to guarantee image quality with commercially-available lenses.

As designed, then, the present optical system provides a 1000 x 1000 spot scan of $16\mu m$ spots over a 16 mm x 16 mm field in a completely solid-state x-y scanning system. The schematic and above discussion demonstrate that depending on the system requirements, this optical layout could be reconfigured to match various x-y scan formats with little difficulty. The most difficult lenses to manufacture for the system are C_1 and C_2 , with C_4 the third most difficult; if the total optical path length is not critical, however, the above f# equations show that a longer focal length for all of these lenses will result in larger f#,s, and, therefore, more easily fabricated lenses. Nevertheless, all the values calculated in this example are representative of quality commercial optical components, and should provide excellent results in producing a 1000 x 1000 solid-state x-y scanning system.

2.6.4 A Comparison of Various Y-Scanner Approaches

A listing of the major mechanical Y-scan devices, the AOBD Y-scanner, and the general performance characteristics of each technology is presented in Table 2.6.4. Each device has been quantified both in relation to applicability to the present system requirements and with consideration of the optical system required to implement that component. In the preparation of this table and in the brief discussion of each device in this section, the bulk of the information is drawn from Reference 9.

Fixed Frequency Scanning Devices

Both the torsion rod scanner and the taut band scanners are designed to resonate at a single fixed frequency and are limited to sinusoidal waveforms by nature of their design. Because of the limitation on waveform shapes, the only solution to producing a quality linear scan in the Y-scan plane would be to buffer the incoming data according to the rate at which the Y-scanner oscillates in any portion of the scan. This procedure is awkward at best and expensive at worst, and as a result the fixed frequency scanners are not recommended for the Y-scanning system.

Variable Frequency Mechanical Scanners

In this category are moderate-cost galvanometer systems and higher-cost piezoelectric systems, both of which may include electronic feedback to improve the linearity of their scan. Both types of devices accept a broad range of driving waveforms and are capable of high precision in scanning. The chief advantage of the piezoelectric device over galvanometers is the high frequency at which it can be driven; it cannot, however, achieve the large scan angle of galvanometer systems, and is generally a higher-cost device. For the present application, then, a quality galvanometer system probably provides the greatest flexibility of operation for the lowest cost of these two devices.

Table 2.6.4. Characteristics of Y-Scanning Techniques

<u>Device</u>	<u>Principle of Operation</u>	<u>Optical Scan Angle Peak/Peak</u>	<u>Frequency</u>	<u>Max. No. Resolv. Spots</u>	<u>Cost</u>	<u>Driving Waveform</u>
<u>Fixed Frequency</u>						
Torsion Rod	Oscillating magnetic field excites rod to resonance	Up to 14°	400 to 20,000	500 Poor	Moderate	Sine wave
Taut Band	Resonant "taut band" with moving permanent magnetic armature	Up to 30°	5 to 1000	500 Poor	Low	Sine wave
<u>Variable Frequency</u>						
Galva-nometer	Iron Core or Wound Armature	Up to 60°	0 to 25,000	2,000 Good	Moderate	Sine wave, sawtooth, ramp, random
Piezo-electric	Ceramic wafers bend in an electrostatic field	Up to 2°	0 to 45,000	2,000 Good	High	Sine wave, sawtooth, ramp, random
Rotating Polygon	Multifaceted motor-driven mirror	Up to 180°	0 to 50,000	>10,000 Excellent	Moderate to High	Sawtooth, ramp
Acousto-Optic Beam Deflector	Bragg diffraction from changing Acoustic frequencies in a crystal	Up to 2°	>10,000	2,000 Good	Moderate to High	Sine wave sawtooth, ramp, random

Rotating Polygon Scanners

These scanners, consisting of multifaceted mirrors driven by stepper or continuous-motion precision motors, provide overall the best combination of features for a Y-scanning application. Because of the excellent resolution available in state of the art motor drives and the quality achievable in fabricating precisely-aligned multifaceted mirror assemblies, rotating polygon mirror systems can achieve the highest Y-scan frequencies available and are limited in resolution only by the ability of scan lenses to resolve spots. The main drawback to the polygon scanner approach is cost, which can be extremely high when the scanner cost and the cost of the scan lens are added together. For this reason, for low-resolution systems with less than 1000 spots, the polygon scanner may not be appropriate for a given application.

Acousto-Optic Beam Deflectors

Available at moderate-to-high costs, these small-angle scanners provide the only high resolution solid-state optical scanning technique available today. Further, at the high end of AOBD capabilities where 2000 spot time-bandwidth products are desired, they are cost-competitive with polygonal scanners. Also, they have the capability to handle any number of drive waveforms so that for a random-access X-Y scanning technique they are far more suitable than the polygon approach, and (at the lower end of the resolution spectrum - 10 to 500 spots) could be competitive with galvanometer systems depending on the detailed system requirements.

Y-Scanner Implementation

Each of the above devices requires an optical system to integrate it into the X-Y scanner which has been proposed. The specific details of these systems have been described in the preceding sections. One conclusion from these analyses is that post-objective scanning offers the least complicated optical

system, although it may be so compact as to be awkward (especially for small spots in the X-Y scan plan) in some cases. The pre-objective scanner is more complicated, but still relatively inexpensive; it also offers telecentricity and provides greater room for the scanner and placement of optics than the first approach. The AOBD Y-scanner, while a powerful method of optical scanning, is more complicated and more expensive to implement because of the many lenses involved in its use. For these reasons, up to this point the best compromise between complexity and flexibility of the system appears to be the pre-objective scanning approach.

To complete the trade-offs between these techniques, however, a final consideration is that of the scanner's useful duty cycle. This is significant for the present application because, to minimize buffering requirements, a Y-scanner should be capable of scanning a second line of data as soon after the first line of data as possible. As a result, for mechanical scanners a galvanometer system becomes very undesirable, since from 20 to 30 percent of the scan will be lost in retracing and settling for each scan. A polygonal scanner is a much better approach, since by overilluminating two facets of the scanner at the same time, one can guarantee almost a 100 percent duty cycle. The AOBD system, however, of all the techniques described, is the most adaptable to continuous scanning, since at the Y-scan speeds there is a negligible "lag" or "retrace" in the AOBD. Techniques such as have been used in loading the AOBD in the AOBD/ATWL X-scan system, and in particular, the "traveling chirp" concept, are directly applicable here. The chief limitation in the AOBD design for a 100 percent duty cycle system will be the difficulty in fabricating a crystal long enough and homogeneous enough to provide the necessary beam uniformity and scan linearity. Such crystals are available, however, and represent primarily a system cost impact rather than a high technical risk. Of the various Y-scanner approaches described, only the AOBD

Y-scanner can provide all the necessary performance features including a 100 percent duty cycle; it is recommended for future system implementations.

SECTION III

DEVICE DEVELOPMENT

In this section we discuss the development of acousto-optic devices for laser scanning. An analysis of an optimum drive for an ATWL is presented in Paragraph 3.1 while the experimental results of the development of the ATWL device are presented in Paragraph 3.2. The acousto-optic beam deflector (AOBD) required for the laser scanner is a fairly simple device to fabricate because it is well within the state of the art for Bragg cell beam deflectors. However, the electronics to drive the AOBD at the 200 kHz rate and the drive for the ATWL required some development effort; the results of this effort are presented in Paragraph 3.3.

3.1 ATWL Drive for Efficient Lens Generation

The problem addressed in this section is the determination of the form of the input drive to the transducer that produces a given size acoustic lens with the minimum power consumption. The approach has been to estimate the form the acoustic pulse should have, define the impulse response of the transducer as mounted in an ATWL, and, finally, determine the form of the drive pulse that produces an optimized acoustic lens. The principal results are:

- A general expression for the impulse response of a double-loaded transducer and specific results for configurations of interest for present ATWL designs;
- Pulse forms for efficient lens generation;
- Suggested technique for generating desired pulse forms;
- Suggested technique for the extraction of acoustic power at the far end of the ATWL.

3.1.1 Optimization Considerations

The problem of finding the drive form that produces a given output spot size with minimum power involves a number of mutually dependent factors: the size of the lens, which is partially related to the transducer size and is constrained by frequency-dependent acoustic absorption, is also related to the size requirement of the AOBD; the useful power of the lens (Δn) and the lens size and interaction depth are further constrained by aberrations that spread the focal spot. For our present purposes we will limit ourselves to finding the shape of the input pulse that produces the strongest acoustic (largest Δn) lens assuming a given acoustic energy and a given lens size and depth, neglecting aberration effects.

The model that we assume for the ATWL is a transducer (such as LZT-2H or LiNbO_3 , operated in the longitudinal mode) sandwiched between the acoustic lens material (such as SF-59) and a backing medium (such as Al or air). The strains induced in the transducer, lens material and backing medium are, respectively, $S_1(t)$, $S_2(t)$ and $S_3(t)$. We define the impulse response of the transducer as the strain function in the acoustic lens medium produced by an impulse of free charge (proportional to electric displacement D) on the transducer electrodes. Thus for a more general D ,

$$S_2(\omega) = H(\omega) D(\omega), \quad (3.1-1)$$

where $H(\omega)$ is the frequency response of the transducer (Fourier transform of the impulse response), and $S(\omega)$ and $D(\omega)$ are the transforms of $S(t)$ and $D(t)$.

The criterion for determining the optimum $D(t)$ is not simple, even under the limitations we imposed on ourselves above, by the fact that energy is dissipated into both the backing medium and the lens medium and that the lens is described by the value of the second derivative of $S_2(t)$ at the peak and by the distances in both directions from the peak that $S_2(t)$ is quadratic to some

tolerance (presently undetermined). Furthermore, a determination of the input pulse form that produces maximum $S_2''(t)$ for a given energy leads to an unrealizable pulse drive (infinite in duration) and generally a nonsymmetrical pulse. To circumvent these difficulties we will choose the criterion of maximizing $|S_2''(t)|$ under the constraint of a fixed integrated square transducer electrode current. This constrains the input pulse length and, as will be seen, results in a symmetrical strain pulse.

Let $I(\omega) = iA D(\omega)$ be the transducer current and

$$\int_{-\infty}^{\infty} |I(\omega)|^2 d\omega = K, \quad (3.1-2)$$

where K is a constant and A is the area of the transducer. At the peak of the pulse,

$$|S_2''(t_p)|^2 = \left| A^{-1} \int_{-\infty}^{\infty} \omega H(\omega) I(\omega) Q(\omega) e^{i\omega t_p} d\omega \right|^2. \quad (3.1-3)$$

The function $Q(\omega) = \text{rect}(\omega/2\omega_m)$ is simply an expression of the constraint on lens size, principally due to frequency dependent attenuation, by limiting the frequencies to be equal to or less than ω_m . By the Schwarz inequality,

$$\left| \int_{-\infty}^{\infty} F_1(\omega) F_2(\omega) d\omega \right|^2 \leq \int_{-\infty}^{\infty} |F_1(\omega)|^2 d\omega \int_{-\infty}^{\infty} |F_2(\omega)|^2 d\omega \quad (3.1-4)$$

Applying this to Equation (3.3) at the peak t_p ,

$$|S_2''(t_p)|^2 \leq (K/A)^2 \int_{-\infty}^{\infty} |\omega H(\omega) Q(\omega)|^2 d\omega. \quad (3.1-5)$$

The equality holds if

$$I(\omega) = H^*(\omega) Q(\omega), \quad (3.1-6)$$

$$\text{or } D(\omega) = -iA H^*(\omega) Q(\omega) \quad (3.1-7)$$

Thus, we are faced with the task of providing a drive pulse which is matched with the transfer function of the transducer. From Equation (3.1-1) it is evident that

the strain pulse $S_2(t)$ is the autocorrelation of the impulse response convolved with a sinc function, and is therefore symmetrical about its peak.

Frequency Response

The model for the ATWL is indicated in Figure 3.1.1-1.

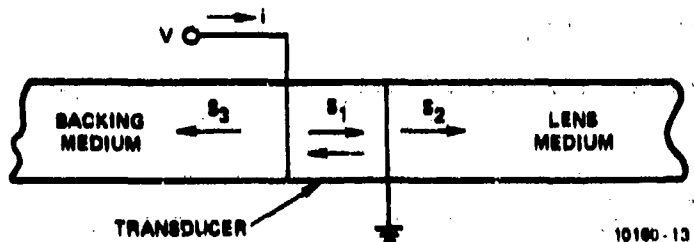


Figure 3.1.1-1. The Model for the ATWL

Let u_1 , u_2 , and u_3 be the particle displacements in the three media. These must satisfy the wave equations

$$\frac{\partial^2 u_1}{\partial t^2} = \frac{1}{v_1} \frac{\partial^2 u_1}{\partial x^2} \quad (3.1-8)$$

subject to the boundary conditions

$$\begin{aligned} T_1(0) &= T_3(0) \\ T_1(d) &= T_2(d) \end{aligned} \quad (3.1-9)$$

and the initial conditions

$$\left(\frac{\partial u_1}{\partial t}\right)_{x=0} = \left(\frac{\partial u_3}{\partial t}\right)_{x=0} \quad (3.1-10)$$

$$\left(\frac{\partial u_1}{\partial t}\right)_d = \left(\frac{\partial u_2}{\partial t}\right)_d$$

where $S = \partial u / \partial x$, D and the stress T satisfy

$$T_1 = c_1 S_1 - h D \delta_{11}. \quad (3.1-11)$$

The c_i are the elastic stiffness constants, h is the piezoelectric modulus, d is the thickness of the transducer, v_i are the sound velocities and δ_{ij} is the Kronecker delta. Below we use $k_i = \omega/v_i$ and t as the time of the impulse. Letting $D(\omega) = D_0 \exp(i\omega t)$ and

$$\begin{aligned} u_1 &= B_1 [\sin k_1 x + B_2 \cos k_1 x] D_0 \exp(i\omega t) \\ u_2 &= G_2 \exp[-i(k_2 x - \omega t)] \\ u_3 &= G_3 \exp[i(k_3 x + \omega t)] \end{aligned} \quad (3.1-12)$$

the constants B_1 , B_2 , G_2 and G_3 are evaluated, after some algebra, through the boundary conditions to obtain

$$H(\omega) = \gamma \frac{1 - \cos k_1 d - i b \sin k_1 d}{\sin k_1 d - i e \cos k_1 d} \quad (3.1-13)$$

where

$$\gamma = \frac{-i h v_1 D_0}{c_1 v_2 (1+ab)} \quad (3.1-14)$$

$$a = c_2 v_1 / c_1 v_2 = z_2/z_1$$

$$b = c_3 v_1 / c_1 v_3 = z_3/z_1$$

$$e = (a + b) / (1 + ab),$$

and z_i is the acoustic impedance of medium i . Figure 3.1.1-2 contains plots of $|H(\omega)|$ for an unloaded transducer ($a = b = 0$), for a LiNbO_3 transducer loaded on

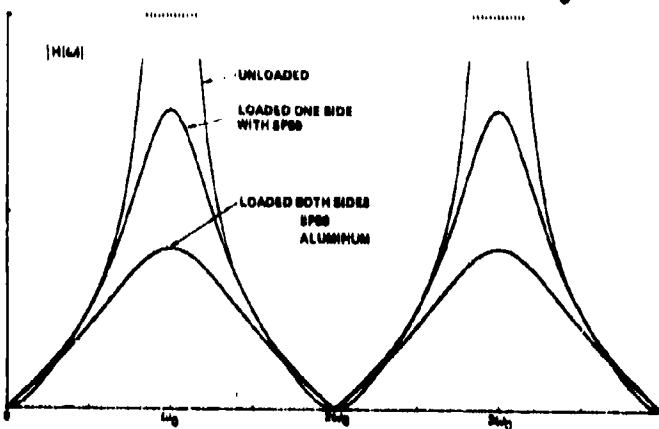


Figure 3.1.1-2. Absolute Value of the Frequency Response of a LiNbO_3 Transducer

one side with SF-59 ($a = 0.656$, $b=0$), and for a LiNbO₃ transducer loaded on one side with SF-59 and on the other side with aluminum ($a=0.656$, $b=0.567$). Note that the strain in the backing medium resulting from an impulse of charge is also given by Equation (3.1-13) but with a and b interchanged.

Impulse Response

The impulse response is given by the Fourier transform of Equation (3.1-13) and, as shown in Appendix A, is given by

$$H(t) = 4 \pi a D_0/c_3(1 + a)(1 + b) \\ \times \left\{ -\frac{1+b}{2} \delta(t) + \sum_{n=0}^{\infty} r_2^n r_3^n \delta[t - (2n+1)T] - \left(\frac{1-b}{1+a}\right) \sum_{n=1}^{\infty} r_2^n r_3^n \delta[t - 2nT] \right\} \quad (3.1-15)$$

where the acoustic amplitude reflectances are given by

$$r_2 = \frac{1-a}{1+a}$$

and

$$r_3 = \frac{1-b}{1+b}$$

Schematics of these responses for single and double loaded LiNbO₃ and LZT-2h transducers are shown in Figure 3.1.1-3. Also shown are the responses in the aluminum for the double loaded cases. These have been normalized with respect to the second (maximum) pulse; the total power into the aluminum is slightly less than that into the SF-59.

Figures 3.1.1-4, 3.1.1-5 and 3.1.1-6 show in each case the response to a pulse $D(t) = D_0 \sin(2\pi t/T) / (2\pi t/T)$; that is, a pulse sharply band-limited to $\omega_b = 2\omega_0$, where

$$\omega_0 = 1/2T = v_1/2d \quad (3.1-17)$$

is the first resonant frequency of the transducer.

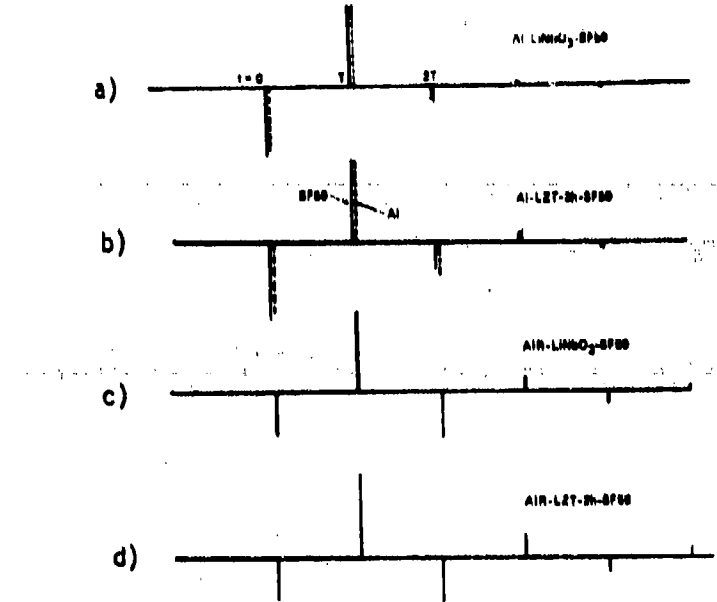


Figure 3.1.1-3. Impulse Responses of Loaded Transducers

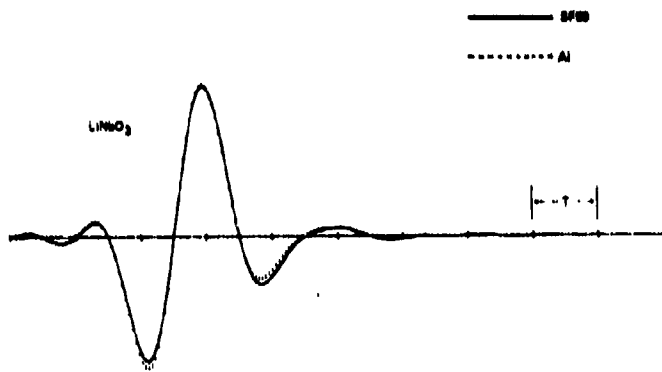


Figure 3.1.1-4. Pulse Response of Al-LiNbO₃ - SF-59 Transducer for Sharp Band Limit at $w_b = 2 w_0$

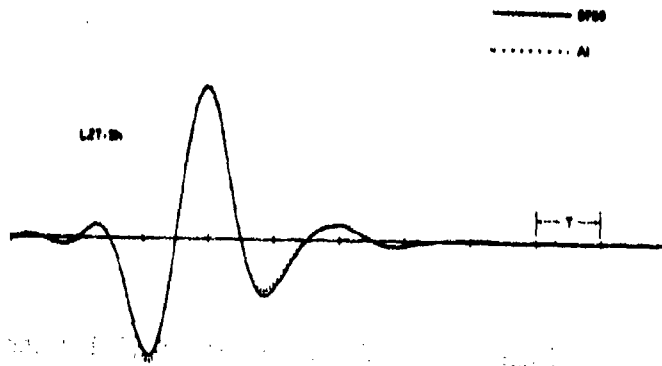


Figure 3.1.1-5. Pulse Response of $A_1 = LZT - 2H - SF-59$
Transducer for Sharp Band Limit at $\omega_b = 2\omega_0$

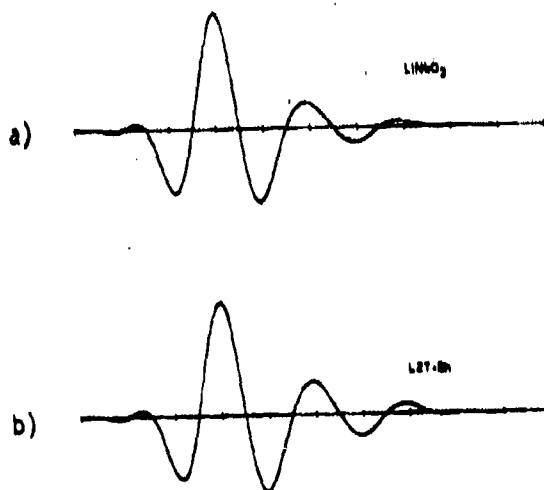


Figure 3.1.1-6. Pulse Response for Transducers loaded on One Side
With SF-59 Band Sharply Limited at $\omega_b = 2\omega_0$

Drive Pulses

A band-limited matched input pulse is identical to the relevant solid curve of Figures 3.1.1-4 through 3.1.1-6 played backwards; that is, since the frequency spectrum of the required pulse is the complex conjugate of the transducer frequency response Equation (3.1-7) up to the band limit, the required pulse form is the time-reversed pulse response. Figure 3.1.1-7 shows the required transducer electrode charge pulse, the corresponding required transducer current

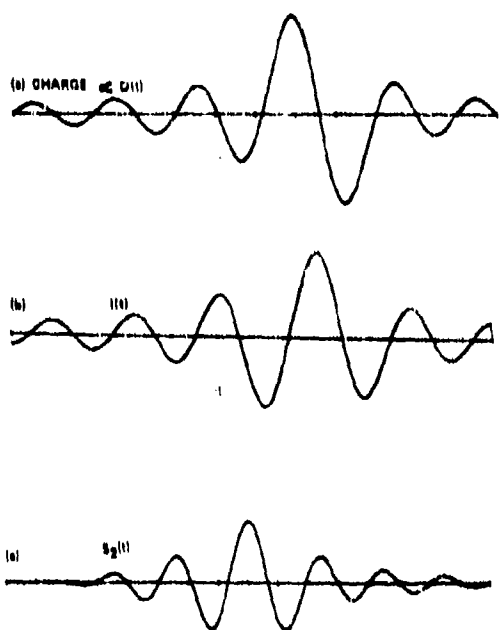


Figure 3.1.1-7. Band-Limited Matched Pulse Forms and Lens Pulse. $\omega_b = \omega_0$

pulse and the resulting strain pulse in the lens medium, for a band limit $\omega_b = \omega_0$. Figures 3.1.1-8 and 3.1.1-9 are the same, but with cutoff frequencies, respectively, of $\omega_b = 1.5\omega_0$ and $\omega_b = 2\omega_0$.

Note that Figure 3.1.1-8 and particularly Figure 3.1.1-9 exhibit less side lobe ringing than Figure 3.1.1-7. This is a result of the discontinuities

created in the spectra of Figures 3.1.1-7 and 3.1.1-8 by the band limits imposed (see Figure 3.1.1-2). (The lack of symmetry in the side lobes of the autocorrelation pulses was the result of the insufficient data block sizes used in the computations. These curves are for illustration only; more accurate values are readily obtainable.)

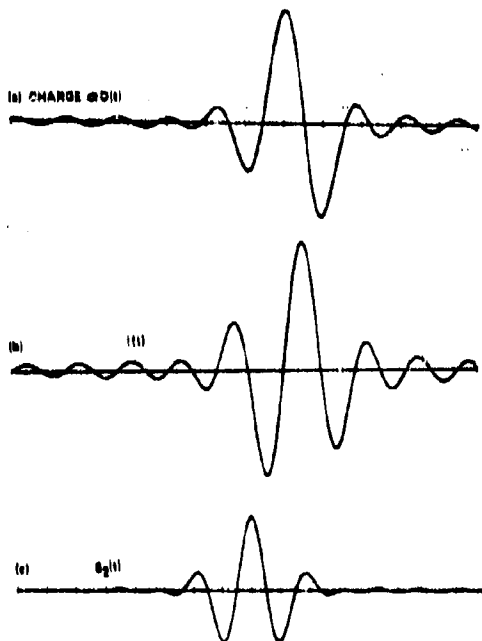


Figure 3.1.1-8. Band-Limited Matched Pulse Forms and Lens Pulse. $\omega_b = 1.5 \omega_0$

These curves are sufficient if the transducer is driven by a current source. For a voltage source the form of the voltage pulse corresponding to the curves above needs to be known. To determine this we note that the transducer parameters must satisfy

$$E = -h S_1 + \beta d D , \quad (3.1-18)$$

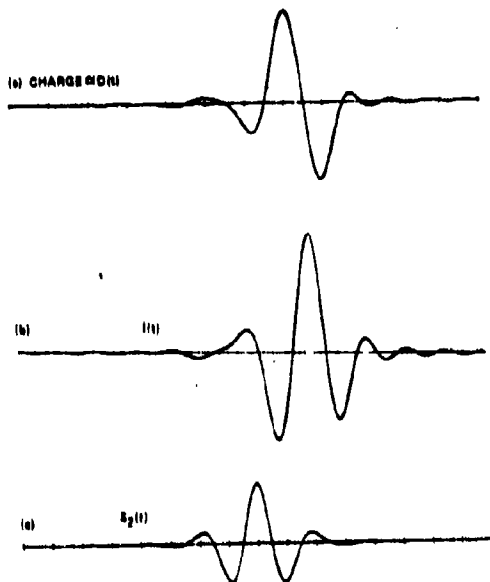


Figure 3.1.1-9. Band-Limited Matched Pulse Forms and Lens Pulse. $\omega_b = 2\omega_0$

where E is the electric field, β is the reciprocal permittivity parameter and the other parameters are as defined earlier. The transducer voltage is

$$v = \int_0^d E(x)dx = -h[u_1(d) - u_1(0)] + \beta dD. \quad (3.1-19)$$

Using the expression for $u_1(x)$ from Equation (3.1-12) (including the evaluated B constants that, for brevity, were not included in the earlier discussion), the voltage spectrum is found to be

$$v(\omega) = \zeta W(\omega) D(\omega) \quad (3.1-20)$$

where

$$\zeta = \frac{h^2 d}{c_1(1+ab)}$$

and

$$W(\omega) = \frac{v_1}{\omega d} \frac{i e \sin(\omega d/v_1) - 2[1 - \cos(\omega d/v_1)](1+ab)^{-1}}{\sin(\omega d/v_1) - i e \cos(\omega d/v_1)} + \frac{c_1(1+ab)}{h^2} \quad (3.1-21)$$

The function $W(t) * \sin(2\pi t/T) / (2\pi t/T)$, which is the F.T. of Equation (3.1-21) sharply band-limited at $\omega_b = 2\omega_0$, has been numerically computed and is shown in Figure 3.1.1-10 for a double-loaded and a single-loaded transducer. Note that a voltage pulse as in Figure 3.1.1-10(a) will produce a lens medium strain pulse like the solid curve in Figure 3.1.1-4; the pulse of Figure 3.1.1-10(b) produces the strain pulse of Figure 3.1.1-6(a). The voltage pulse required to generate matched strain pulse Figure 3.1.1-9(c) is Figure 3.1.1-10(a) convolved with Figure 3.1.1-3(a) (solid lines).

3.1.2 Comments on Implementation

The chief difficulty with electronic matched filtering is normally that it is not physically realizable; that is, a matched filter is asked to respond to a pulse before the pulse arrives. The present situation is one in which the filter is defined and the pulse is to be constructed to match the filter. Since we know, in this application, precisely when a pulse is to arrive, it is clear that a matched pulse (predictive portion and all) can be generated. However, for

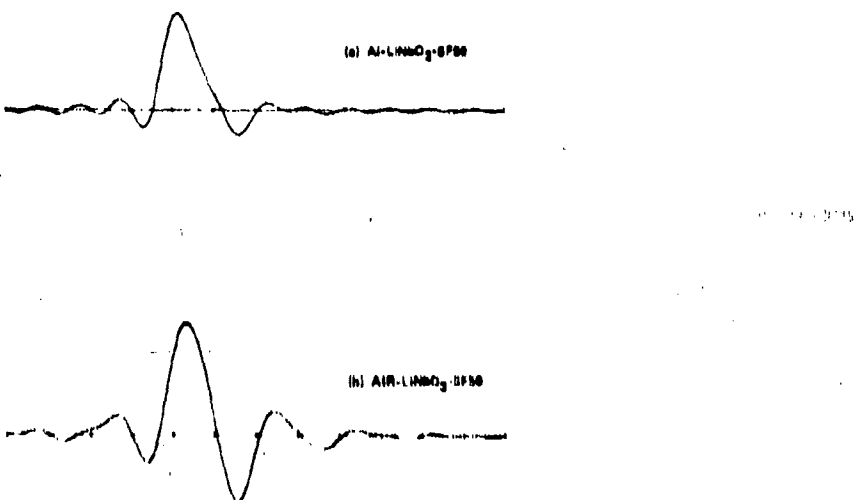


Figure 3.1.1-10. Voltage Pulse Corresponding to a Sharply Band-Limited Input Charge Pulse

the classical reasons, analog techniques are not well suited to generating a matched pulse. A filter can, in principle, be designed to approximate a matched pulse from an impulse if sufficient lag is introduced. However, it is believed that an easier and less expensive approach is to construct the drive pulse from samples stored in a PROM, as sketched in Figure 3.1.2-1.

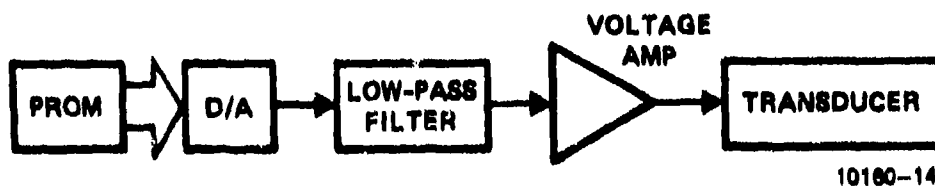
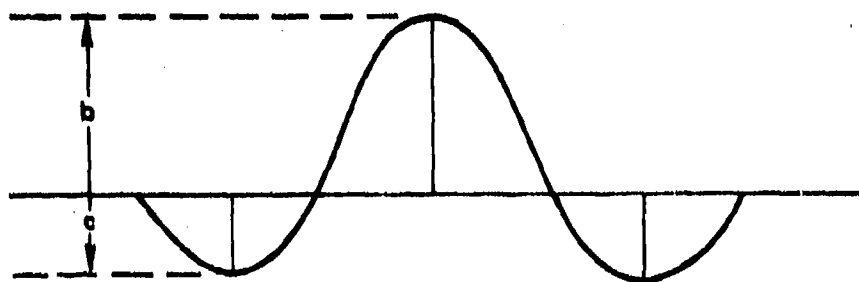


Figure 3.1.2-1. Transducer Pulse Generation

For a transducer with a resonant frequency of 5 MHz, such that the maximum frequency in the drive pulse, for example, is 10 MHz, the minimum sampling frequency, allowing some room for the low pass filter cutoff region, is 25-30 MHz. A D/A convertor and low-pass filter can be obtained for several hundred dollars. PROMs are even less expensive.

Power Considerations

The objective is to produce a lens pulse with the minimum acoustic energy. This means, obviously, that superfluous side lobes should be suppressed. A single central lobe, however, is not efficient; consider, for discussion purposes, the symmetric lens sketched in Figure 3.1.2-2, where b and c are the magnitudes of the central and side peaks, respectively. If we assume, for the



10160-15

Figure 3.1.2-2. Hypothetical Lens Pulse

moment, that the energy in each lobe is proportional to the square of the magnitude of the lobe, we find the energy in the pulse to be

$$U = b^2 + 2c^2 \quad (3.1-22)$$

If we minimize this under the condition of constant peak-to-peak strain $b-c = K$,

$$\begin{aligned} dU &= d[b^2 + 2(b-k)^2] \\ &= [2b + 4(b-k)] db \\ &= 0, \end{aligned} \quad (3.1-23)$$

we find that $c = -b/2$ is the optimum condition. In practice, side lobes smaller than the central peak will be narrower, so that the optimum c/b ratio will be slightly larger than $1/2$. It will be noted that our lenses, particularly Figure 3.1.1-9(c), agree quite well with these guidelines, even though they were not derived under the condition of minimum energy, but of minimum integrated square input current. Note also that a minimum energy pulse for a given peak-to-peak swing would have a principal lobe and only one equal-magnitude side lobe. This, in fact, is what results when one derives the pulse shape under the minimum energy condition, which we rejected for reasons of symmetry. A further comment, appropriate at this point, is that minimization of superfluous side lobes suggests that the Q of the transducer sandwich should be as low as possible. The ideal case for minimizing the lens medium acoustic energy is perfect matching of the transducer with the lens medium and to the backing medium. For minimization of the total energy the ideal case would be perfect matching to the lens medium and no backing ($r_3 = -1$). These cases are illustrated (using Equation (3.1-15)) in Figures 3.1.2-3 (a) and (b), respectively.

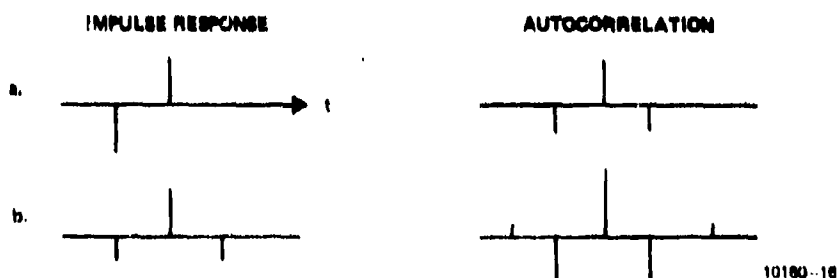


Figure 3.1.2-3. Ideal ATWL

To estimate the energy lost into the backing medium, we note that this energy is given by¹⁰

$$U_3 = \rho_3 \int [v_{p3}(x)]^2 dx \quad (3.1-24)$$

where v_p is the particle velocity and ρ_3 is the density. Since by definition

$v_p = T/z$, $T = c S$ and $z = \rho v$, we can write

$$\frac{U_3}{U_2} = \frac{z_2 v_2}{z_3 v_3} R \quad (3.1-25)$$

where

$$R = \frac{\int [c_3 S_3(x)]^2 dx}{\int [c_2 S_2(x)]^2 dx} \quad (3.1-26)$$

For a LiNbO₃, Al, SF-59 ATWL, R is about $(b/a)^2 = 0.75$ using Equation (3.1-15) and its counterpart for the aluminum, since the autocorrelation of H(t) in Figure 3.1.1-1(a) is approximately equal to the cross correlation of H(t) with the pulse response in the Al (dashed lines). Using

$$\begin{aligned} z_2 &= 2.0 \times 10^7 \\ z_3 &= 1.73 \times 10^7 \\ v_2 &= 3201 \\ v_3 &= 6420 \end{aligned} \quad (3.1-27)$$

we find

$$\frac{U_3}{U_2} = 0.43 \quad (3.1-28)$$

Pulse Extraction

Since heating in the lens medium appears to be a serious problem, it is of interest to consider the requirements for extracting the acoustic pulse at the far end of the ATWL. The obvious solution is to acoustically match the lens medium to another that can be more readily and safely cooled. Matching impedances may not be easy, however, and even a well matched antireflection layer does not

work well for a pulse with only a few lobes. It should be possible to extract the pulse with another transducer. However, the transducer must be properly driven. To determine the requirement for the drive, we observe that the lens pulse approaching the transducer has form $V_{in}(t) * H(t)$ and the pulse that would be reflected from a shorted transducer has form $R(t) * V_{in} * H(t)$, where $R(t)$ is the closed-loop ($V=0$) reflectance of the transducer

$$R(t) = r_1 \delta(t) + r_2 t_1^2 \sum_{n=0}^{\infty} (-1)^n (r_1 r_2)^n \delta(t-2nT), \quad (3.1-29)$$

where r_1 , r_2 and t_1 are internal zero voltage surface reflectance coefficients, which can be determined from the constitutive relations of Equation (3.1-11) and Equation (3.1-18). Note that r_1 and r_2 above are not the same as the quantities in Equation (3.1-16), which are zero surface charge reflectances.

The reflected pulse must be negated by driving the transducer with $V_{out}(t)$ such that

$$V_{out}(t) * H(t) = -R(t) * V_{in}(t) * H(t) \quad (3.1-30)$$

and therefore

$$V_{out}(t) = -R(t) * V_{in}(t) \quad (3.1-31)$$

If the transducer drives are current sources, then $V(t)$ of Equation (3.1-31) becomes $I(t)$, and $R(t)$ is defined in terms of the zero surface charge coefficients.

In all of the preceding discussion it has been assumed that the "catcher" transducer was identical to the "pitcher" transducer, with the same backing medium. This is not an absolute requirement for extraction of the acoustic energy from the lens medium, but alteration of the "catcher" characteristics complicates the analysis. Also, the obvious required time delays have been omitted for simplicity.

A remaining question concerns the dissipation of the energy. For transducers loaded on only one side, all the energy must be dissipated in the

"catcher" drive circuit. This point needs to be more clearly defined. If a backing medium is present, a pulse (perhaps larger than the incoming pulse) is generated into the backing medium of the "catcher," for which provisions must be made for dissipation.

As a final note, the air-transducer-matched lens medium ATWL which was described earlier as being ideal in that it lost no energy into the backing medium and produced an energy-efficient pulse in the lens medium, is also ideal for energy extraction.

3.2 Development of Acoustic Traveling Wave Lens (ATWL)

This section of the report summarizes the development activities for a 200 kHz scan rate, 1000 spot/line ATWL. The results obtained during various phases of the ATWL development are presented. To extend the capability of the ATWL required some solutions to several problems that were experienced when the device was operated at higher repetition rates. The two major problems were: 1) High electrical power switching at 200 kHz rate and 2) Loss of significant power into the compression fixture.

During the course of this investigation, two other problems were encountered. At low repetition rates the acoustic reflections from the end of the ATWL, opposite the transducer end, died out between two successive scans. At high repetition rate a small but troublesome reflection persisted to cause nonuniformity in the traveling lens. The other problem discovered was that the cooling of the ATWL block at each end was not enough to prevent cracking of the ATWL at high repetition rate.

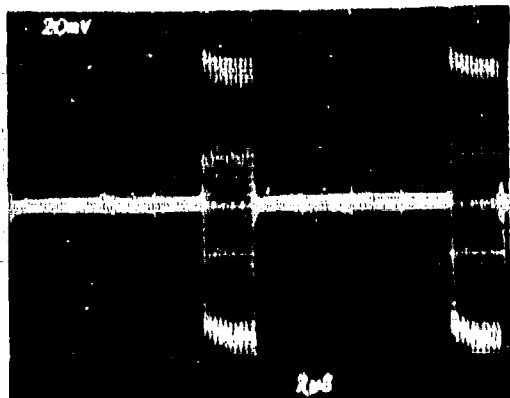
Our development effort was directed to solving the problems just mentioned.

3.2.1 Proper Excitation of ATWL at High Repetition Rates

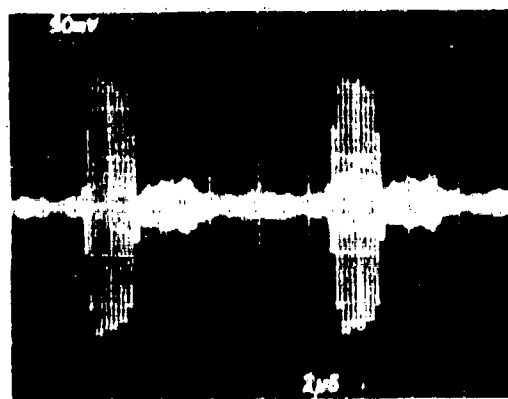
Due to switching time limitations of high voltage SCR's, the circuits using these devices are not suitable for the 200 kHz repetition rate requirement. In an earlier IR&D experiment an effort was made to generate strong acoustic waves without electrically over-stressing the transducer; resonance excitation was suggested and verified to be superior to the step excitation used in previous devices. The resonance excitation of the transducer generated higher peak acoustic strain with the same peak voltage as in the step excitation. The resonance excitation occurred when several cycles of electrical signal at the resonance frequency were applied to the transducer. In an ATWL experiment

consisting of a PZT-5 input transducer and a PZT-5 detector transducer at the other end of the ATWL, it was observed that the output signal attained its full strength at about the third cycle when excited by an RF pulse. This observation was consistent with the theory that PZT-5 has electromechanical coupling factor $k = 0.49$ which results in the electromechanical Q = $\pi Z_t / 4k^2 = 2$ (Reference 2). The efficiency of resonance excitation was further verified when a focused spot of the same size as in a step excitation was obtained with an RF pulse of one third the peak voltage. A consideration of the acoustic transducer's bandpass characteristic and the amplitudes of the Fourier components produced by the step excitation versus the RF pulse of equal peak voltage suggests that a resonance RF pulse with a rise time equal to the reciprocal of the transducer bandwidth would be the best choice for exciting the ATWL transducer. The rise and fall time of the RF pulse should be such that the RF pulse does not contain any frequency component outside the transducer bandwidth. The photographs in Figure 3.2.1-1 and 3.2.1-2 shows the effect of the shape and width of the RF pulse on the acoustic lens and RF reflection as observed in an ATWL. The top photograph shows the gated RF input signal into an ATWL. The middle photograph of Figure 3.2.1-1 show the throughput signal detected by a second transducer attached to the opposite end of the cell. The bottom photograph shows the reflected signal as seen at the input transducer using an electrical bridge circuit (the output transducer was terminated to a 50 Ω load.)

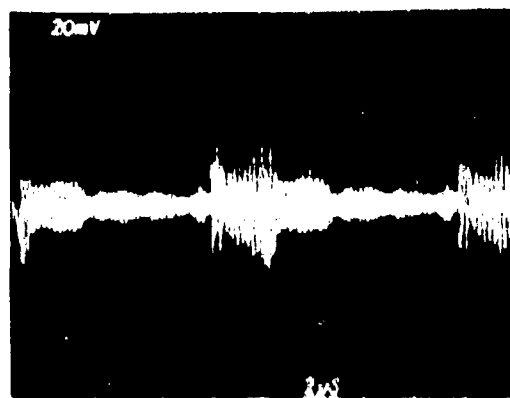
In Figure 3.2.1-2 a similar experiment was performed with a slowly rising and falling RF pulse as shown in the top photograph. Note that the reflected wave is reduced by using a shaped input to the transducer. The reduction in the reflected signal lowers the power requirement for the ATWL. By reducing the number of cycles a result similar to that shown in Figure 3.2.1-2 is obtained.



(a) INPUT SIGNAL



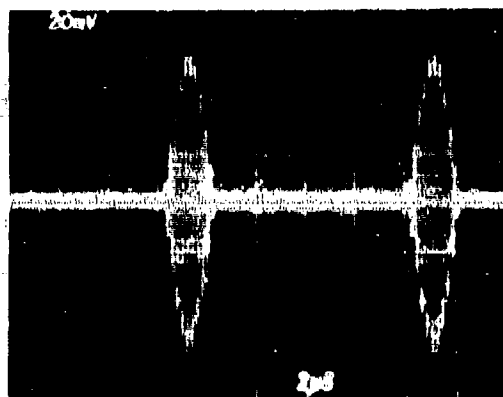
(b) THROUGHPUT SIGNAL



(c) REFLECTED SIGNAL WITH OUTPUT
 50Ω TERMINATION

10160-17

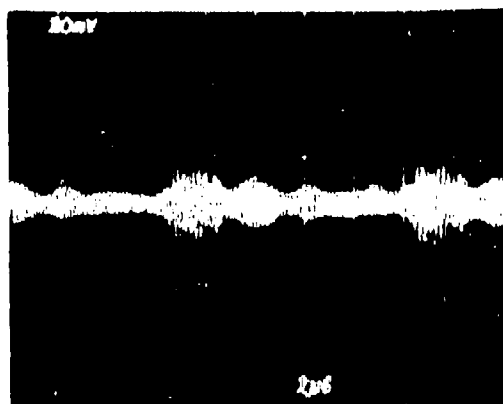
Figure 3.2.1-1. Square Wave Modulated RF Pulse



(a) INPUT SIGNAL



(b) THROUGHPUT SIGNAL



(c) REFLECTED SIGNAL WITH OUTPUT
50Ω TERMINATION

10180-18

Figure 3.2, 1-2. A Shaped RF Drive Pulse.

The reduced voltage requirement for the ATWL transducer in the resonance excitation mode allowed us to successfully use a readily available high power RF amplifier for driving at the 200 kHz repetition rate ATWL. The RF amplifier used in the present investigation was a Class A amplifier with 400 W output power capability and 30 MHz bandwidth.

3.2.2 Maximization of Power Transfer Between the Transducer and the ATWL Cell

For the best use of the input electrical power to ATWL, it is desirable that the transducer couple very little energy into the compression fixture and as much as possible into the ATWL cell. In most acoustic devices, one of the transducer faces is bonded to the work piece and the other face is left free. Therefore, due to the very low coupling of the high frequency acoustic energy into the air, all the energy is coupled into the medium desired. In the present case, the high stress level necessary to produce a $12 \mu\text{m}$ spot is assumed to be above the tensile strength of SF-59 glass. In order to generate higher compression stress in the acoustic wave than the tensile stress of the material, a compression bias is applied to the ATWL assembly. This arrangement causes transducer to radiate into the compression fixture as well as the glass cell.

If the compression fixture is required to make contact with the transducer, the only effective way to isolate the transducer and the compression fixture is to use a multiple quarter wave plate stacked between the transducer and the compression block. This stack can act like a multilayer dielectric reflective coating in optics. Partial isolation can be achieved if the contact between the transducer and the compression block is left dry. The transmission of the acoustic energy to the ATWL cell is improved by a matching plate between them. It was thought that the resonance excitation of the transducer introduces stresses with less gradient change than the step excitation case; therefore the breakage of SF-59 glass observed in the previous ATWL work may not occur with the gated RF

drive. For this reason, a metallically bonded transducer without any compression bias was tested for breakage of the glass at a power level required to produce a $12 \mu\text{m}$ spot. We found that the glass did not break due to the acoustic compression wave overstressing the glass. However, we did experience breakage due to a thermal buildup problem. The acoustic energy is converted to thermal energy from reflections and absorption and causes the glass cell to heat up very rapidly causing it to crack.

Since the thermal build up of the SF-59 glass is a problem, we investigated the possibility of converting the acoustic energy into electrical energy by another transducer at the other end of the cell. To evaluate various ideas for maximizing the energy transfer between the transducer and the cell, the following fabrication and experiments were carried out.

An ATWL was fabricated and assembled as shown in Figure 3.2.2-1. Note that a transducer was placed at each end of the cell to help measure the energy

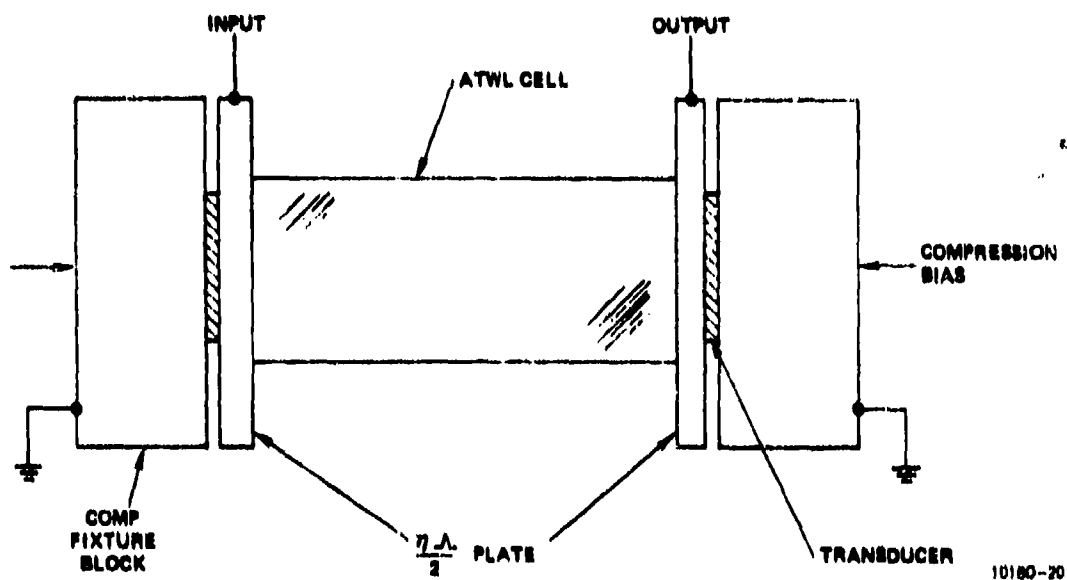


Figure 3.2.2-1. ATWL Assembly Used on the Earlier Experiments
loss to the compression fixture and to reduce the heating problem. The
compression fixture is grounded and the quarter wave plates serve as the other

electrode. The quarter wave plates are polished aluminum plates where the thickness is an N multiple of half the acoustic wave length. An epoxy resin (without the hardener) was used as the acoustic coupling material on both sides of the quarter wave plates; however, no resin was placed between the compression block and the transducer surface. After tuning both PZT transducers to 3.5 MHz, the throughput was measured in the pulsed mode. The throughput was between 20 to 25 percent indicating substantial power loss into the compression fixture and reflections. Due to the bidirectionality of the transducer under compression it is theoretically impossible to absorb all the energy incident upon the receiving transducer even though it is perfectly matched electrically. Only when the transducer is isolated from the compression fixture can all the energy be absorbed.

An attempt was made to isolate the transducers from the compression fixture using brass and mylar sheet quarterwave stacks with an interface of thin resin. The throughput observed in this condition was less than 6 percent. Because of the many unknown acoustic properties of the brass and mylar sheets, the investigation was not carried further. In another attempt, aluminum and tungsten sheets were used to make the quarterwave stacks. In this case, the plates were epoxied together. The throughput measured in this case was less than that observed in the ATWL without a reflective stack. Uneveness of the epoxy, plates, and PZT as well as interface losses were suspected to be the reasons for the low throughput.

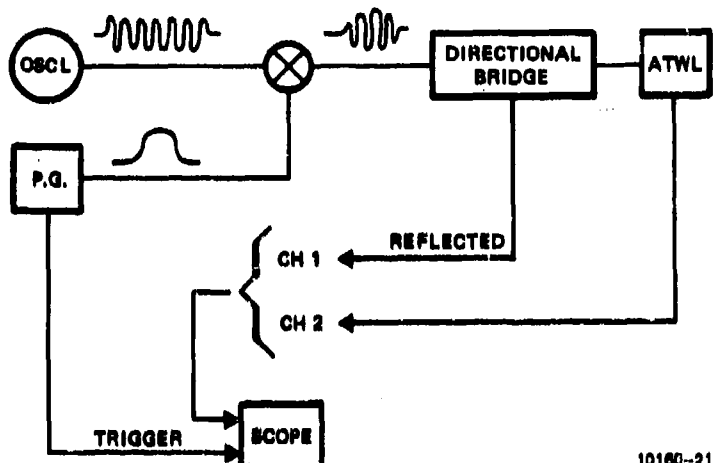
Because of the low throughput observed in the above experiment we needed to establish that a better value of throughput is possible. A fused quartz block with LiNbO_3 transducers metallically bonded on two opposite faces was prepared and tested. A throughput of 64 percent was observed in this case. In a similar experiment where two PZT transducers were used throughput was much lower. Since PZT, being opaque, cannot be made parallel like LiNbO_3 , we suspect that

nonparallelism plus the grainy structure of PZT caused the radiation patterns of the two transducers to be significantly different from each other. Such differences in radiation pattern caused the low throughput. The reflected acoustic energy cannot be detected by the input transducer in such a case. It will be discussed later that, even though less than 1 percent reflection was measured by the input transducer in the ATWL experiment, the optical pattern did show a significant standing wave within the cell. Thus we feel that the major cause of the low throughput in most of our experiments was the difference in the radiation pattern of the input and output transducers. This difference may have increased further with reflective stacks due to the uneven contact. Furthermore, the interface between the sheets of reflective stack falls at the stress maximum for the quarterwave thickness of the sheet. Therefore, increased losses are expected for the interfaces separated by quarterwave compared to halfwave stacks. This was one of the reasons for using a halfwave plate between the transducer and the ATWL cell when an unbonded transducer was used.

The poor performance of the quarterwave reflective stacks led us to discontinue this approach. The only further investigation that we conducted was the use of a dry interface between the compression fixture and the transducer, and the elimination of the compression bias.

An SF-59 block with two LiNbO₃ transducers bonded onto the ends of parallel faces was fabricated into an ATWL cell. A schematic of the setup used to make selected measurements is shown in Figure 3.2.2-2. Note that a directional bridge is used to measure the reflected signal in the ATWL. The ATWL (after tuning) showed less than 3 percent reflection losses for each transducer in the unclamped condition (i.e., compression bias was not applied to the cell, and very low power levels were used in making these measurements). The output energy was 64 percent of the input energy. The acoustic reflections as measured by the

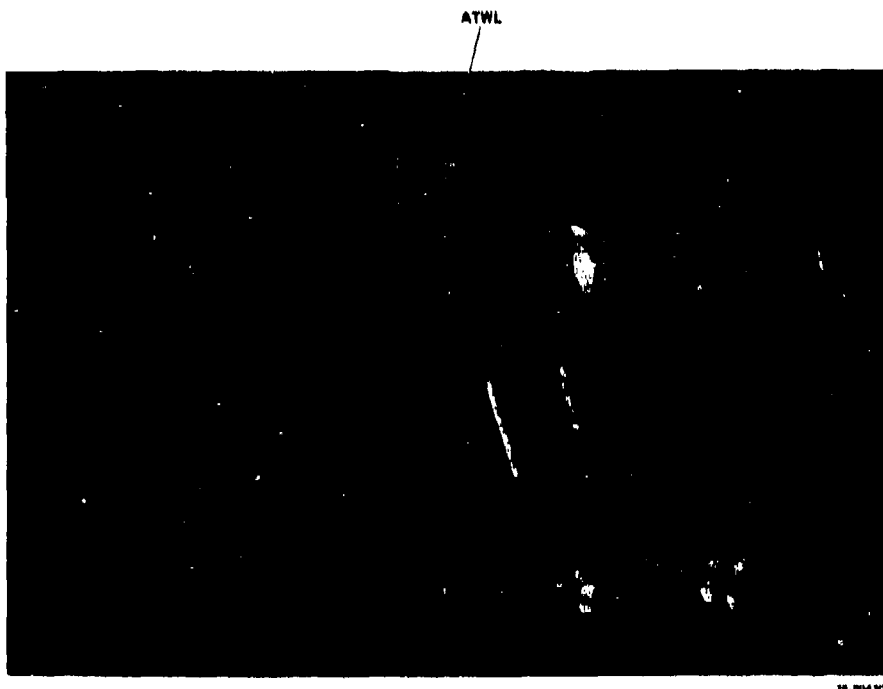
directional bridge were less than 1 percent when the output transducer was terminated into a $50\sqrt{2}$ load.



10180-21

Figure 3.2.2.2. ATWL Electrical Measurement Set-Up

When the ATWL was assembled into the water cooled compression fixture (as shown in Figure 3.2.2-3) and retuned, the reflection and throughput remained



10-01470

Figure 3.2.2-3. ATWL Compression Fixture

unchanged from the unclamped condition. This suggested that good isolation existed between the transducers and the compression fixture. Although the compression fixture was lapped flat at the active sites, we believe that a minute gap existed between the transducer and the compression fixture interface. This condition was sufficient to allow the metallically bonded transducer on the SF-59 block to vibrate unhindered by the compression fixture. When the interface between the transducer and the compression fixture was filled with resin or STP oil, a significant reduction in the throughput was observed.

A completed ATWL was readied for optical testing; unfortunately, in the early stage of operation the output from the high power amplifier became CW due to a malfunctioning circuit and destroyed the ATWL cell by overheating.

An ATWL cell similar to the one described above was assembled using unbonded transducers and halfwave plates between the transducer and SF-59 block. A throughput of 25 percent was measured for this case. The superiority of metallically bonded transducers was established. This device was operated for a considerable period to investigate its optical focusing properties.

A schematic arrangement of the optical test setup that was used to evaluate the performance characteristics of the ATWL is shown in Figure 3.2.2-4. The cylindrical lens is used to focus the light in the X-direction and focuses a few millimeters beyond the ATWL. The traveling lens is moving down the cell in the Y-direction while the expanded (nonscanning) laser beam travels along the Z-axis. The ATWL causes the light to come to focus in the Y-dimension, approximately in the same plane as the cylindrical lens. The spherical lens is used to image the focused spot onto the $2\mu m$ slit; behind the slit is placed a fast avalanche photodiode to detect the light passing across the slit. The focused spot travels along the Y-dimension at the acoustic velocity of the material causing the spot to sweep across the slit. The profile of the scanning

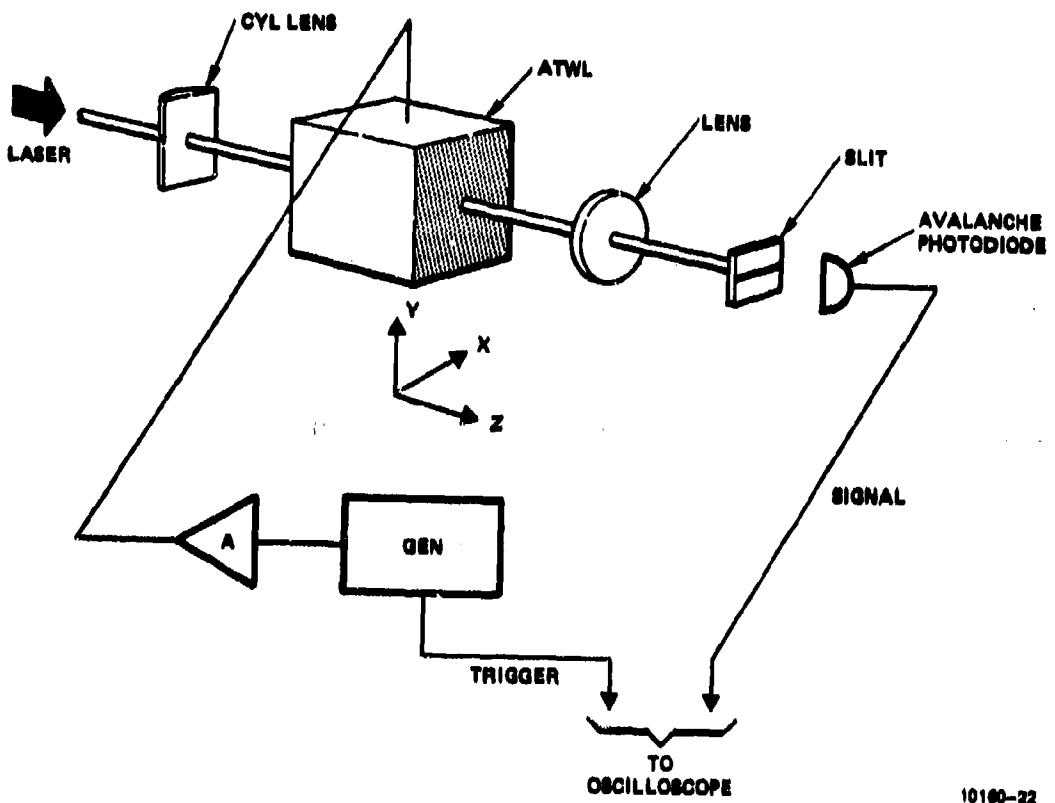


Figure 3.2.2-4. ATWL Optical Test Set-Up

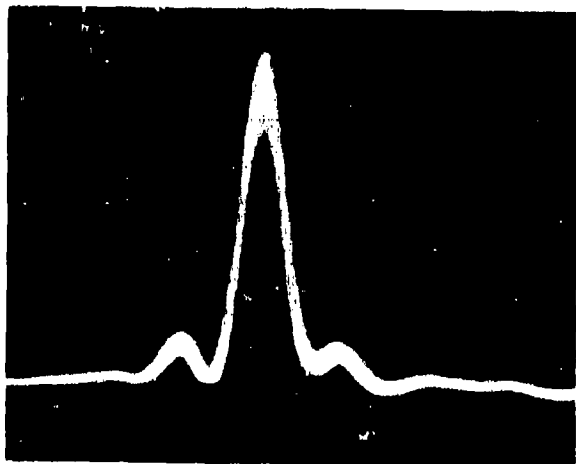


Figure 3.2.2-5. ATWL Focussed Spot Profile

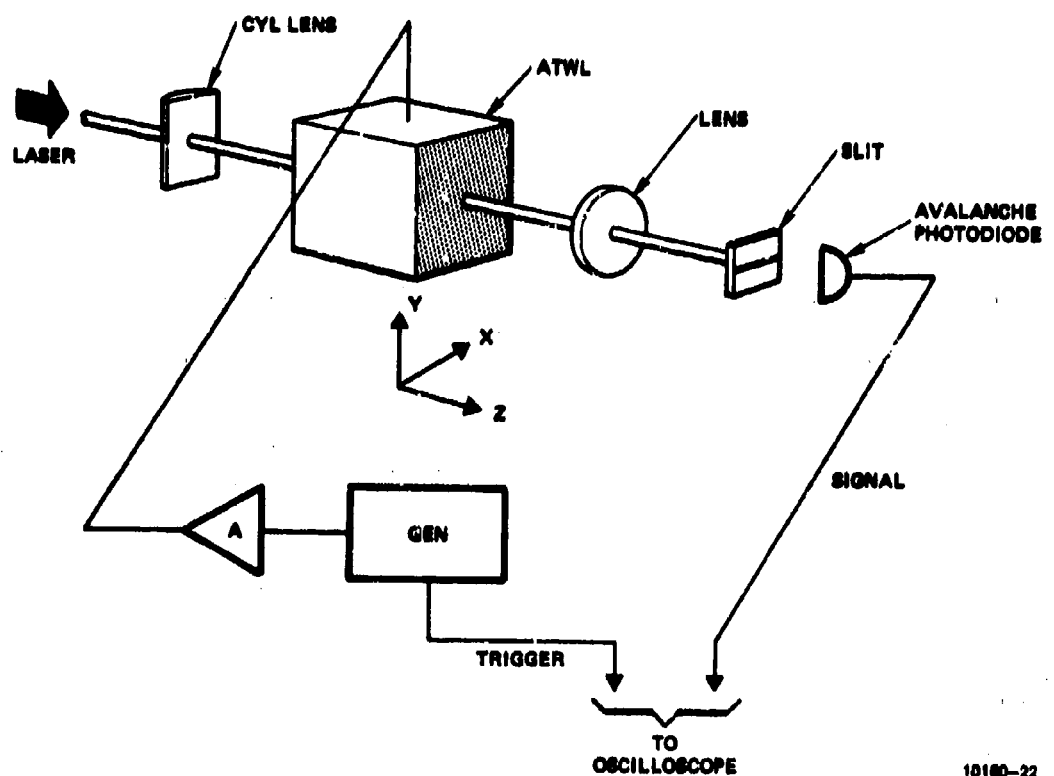


Figure 3.2.2-4. ATWL Optical Test Set-Up

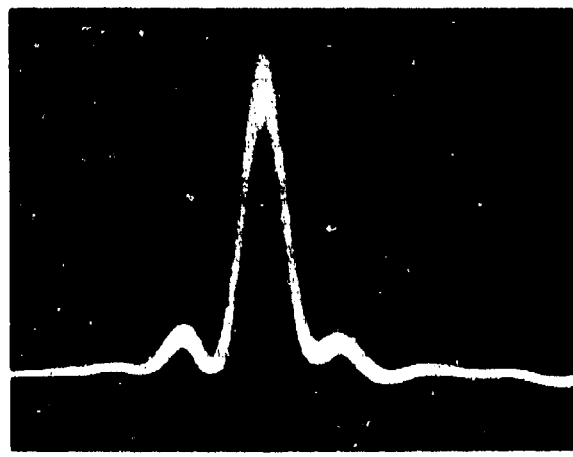


Figure 3.2.2-5. ATWL Focussed Spot Profile

spot can be seen on an oscilloscope. Figure 3.2.2-5 shows the output photograph of oscilloscope trace showing the profile of the spot. A Tektronix 7904 oscilloscope was used with the time base set at 5 ns per division. The width of the spot is approximately 4.5 ns at the halfpower point; the acoustic velocity of SF-59 is $3.2 \mu\text{m/ns}$; therefore, the spot size is obtained by multiplying the velocity by the time to get a $14.4 \mu\text{m}$ spot size at the full width halfpower point (FWHP). With an input beam that is tracking the ATWL, the spot size can be somewhat smaller; if the input beam diameter is $\Lambda/4$, (where Λ is the acoustic wavelength in the SF-59 glass at 4.8 MHz) then minimum aberrations will be seen in the output plane. In an experiment with the ATWL and the laser beam scanning and tracking over a short distance, a $12.8 \mu\text{m}$ spot size was measured using the same drive voltage.

During the optical evaluation of the ATWL it was found that the SF-59 block became significantly hotter than the aluminum blocks in the compression fixture. Poor thermal conductivity of SF-59 did not allow sufficient heat transfer to the aluminum blocks in the compression fixture that were in contact with the transducers. This problem implies that a heat sink on the sides of the SF-59 block is required to keep the glass from over heating and cracking at the full repetition rate.

The other problem seen during the experiment was that the reflected acoustic pulse from the end of the glass interfered with the next pulse. Although monitoring of this reflection at the input transducer end revealed that less than one percent electrical reflection was observed, optical probing showed significant standing waves in the ATWL cell.

3.2.3 Solution to the Reflection and Cracking Problems

The undesirable effects observed in our experiments suggested several design changes. We considered modifying the compression fixture and the ATWL acoustic absorber scheme. Side cooling of the SF-59 block is necessary.

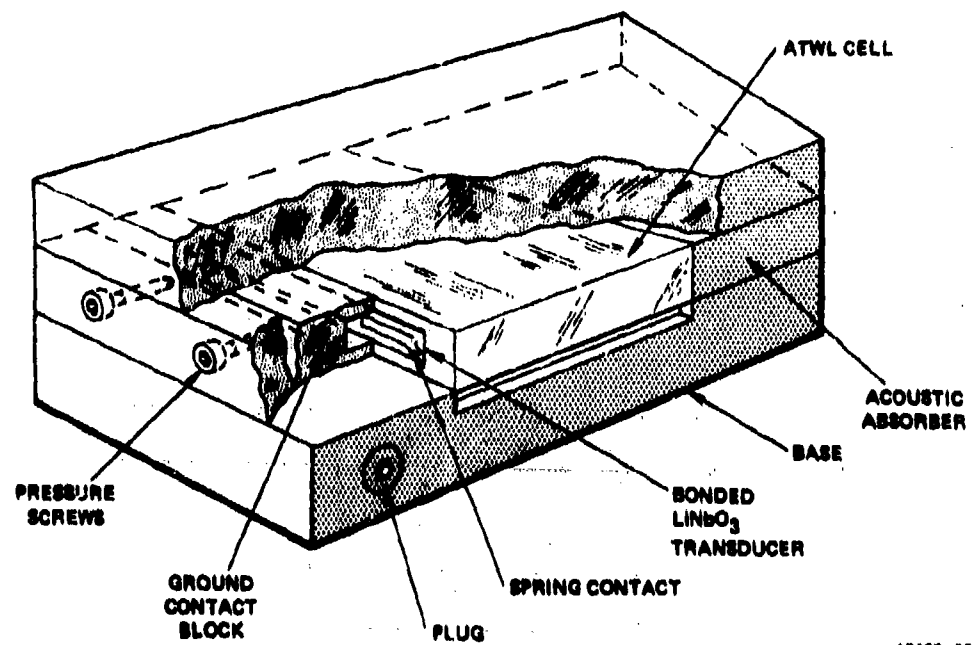
The temperature rise in the glass causes a scan distortion and destroys the tracking between the ATWL cell and the AOBD. The acoustic velocity coefficient for SF-59 is 93 parts per million (PPM) per degree centigrade. The required temperature uniformity can be calculated from the scan distortion specification as follows:

$$\frac{\text{Scan Distortion Range}}{\text{Velocity Coefficient}} = \frac{1 \times 10^{-4}}{93 \times 10^{-6}} = 1.08^\circ \text{ C}$$

Temperature differentials of about 50° C were actually encountered during the preliminary experiment. A heat sink was incorporated into the compression assembly to provide a temperature uniformity of 10° C .

Since gradual stresses are produced in the gated RF pulse excitation of the transducer, we thought that the compression fixture could be completely eliminated if the side heat sinks are used. The reflection problem can be eliminated by cutting all reflecting surfaces at an angle relative to the transducer so that the optical beam passes through a very small portion of the reflected wavefront. As much of the incident wave as possible must be transmitted to a large aluminum block that is in contact with the SF-59 block at the reflecting surface. A schematic of the new arrangement is shown in Figure 3.2.3-1. To learn about whether the bonded transducers and the ATWL cell can withstand the operational acoustic stress without the compression bias, the bonded LiNbO_3 transducers on fused quartz were tested at full power level.

No deleterious effect in this case was observed. The SF-59 material is fragile compared to the fused quartz. Similar experiments using SF-59 were required to establish that the compression fixture can be eliminated.



10100-23

Figure 3.2.3-1. Schematic of the New ATWL Mounting Fixture With Side Cooling

A LiNbO_3 transducer was bonded to SF-59 block with the opposite face polished at a 50 wedge. The cell was assembled in a modified, readily available Harris Q-switch housing which provided a heat sink on the side faces of the SF-59 block. Unfortunately, a small crack developed near the edge of the transducer where ground contact was made by mechanical pressure. Although the crack was outside the aperture, it did propagate across the cell when full electrical power was applied. A small aluminum block was pressed against the 50 wedged face (with STP oil serving as the acoustic interface) to remove the acoustic energy from the SF-59 at the opposite end.

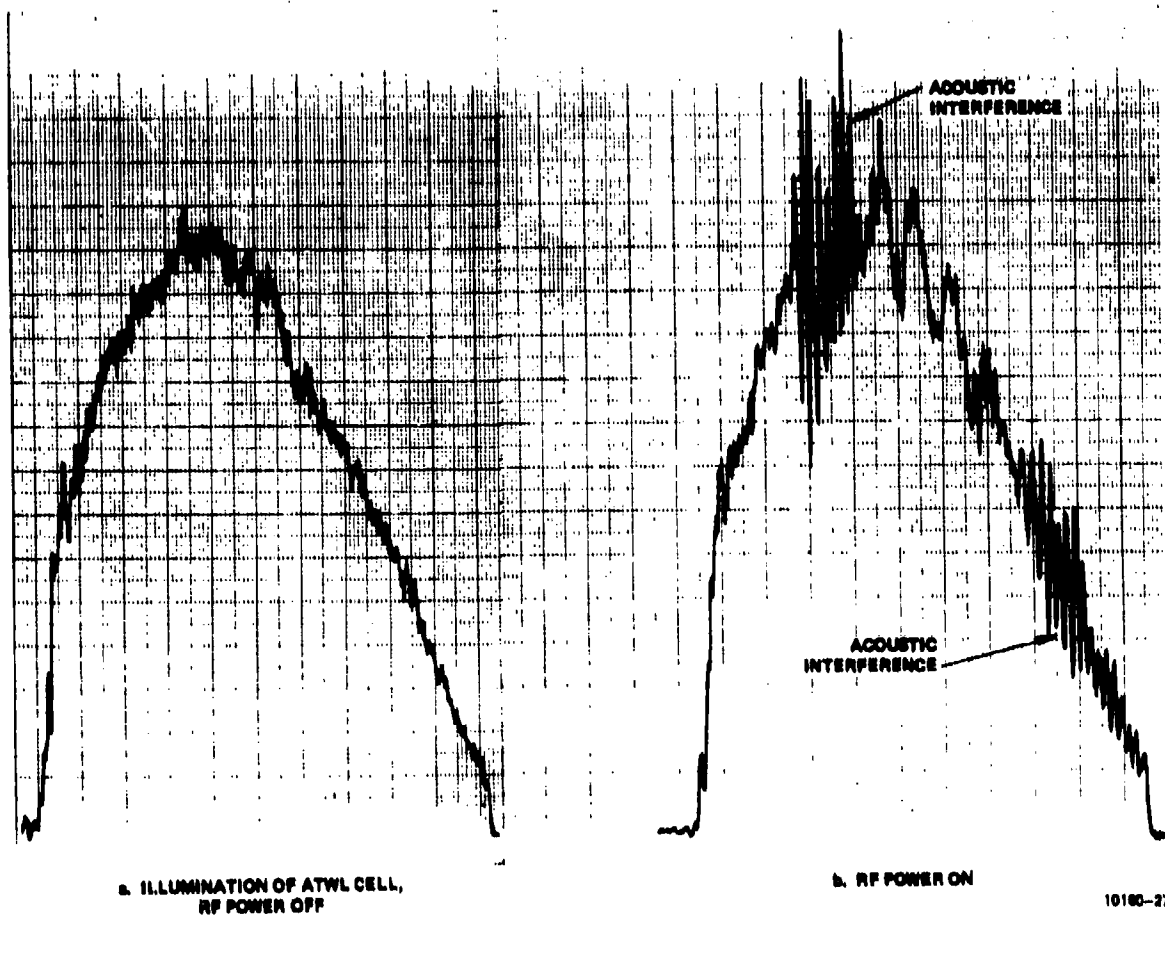


Figure 3, 2, 3-3. ATWL with Parallel Surfaces

near the beginning of the scan. The interference of the second and third pulse is shown near the end of the scan. The illumination of the cell was not uniform (as shown in Figure a) however it is used as a reference to show the acoustic interference problem. A similar experiment was performed with the ATWL described above that has the opposite face polished at a 50° wedge. The results are shown in Figure 3.2.3-4. Note that the acoustic interference has been reduced considerably in amplitude compared to the device shown in Figure 3.2.3-3. A longer SF-59 cell and a larger aluminum block is expected to reduce the standing wave further.

The assembly was tested first at maximum available peak power but at 50 kHz or less repetition rate. The focused spot size and the standing wave were evaluated. The standing wave pattern was reduced significantly and was at an acceptable level. A longer SF-59 cell and aluminum block is expected to reduce the standing wave further.

When the pulse repetition rate was increased to 100 kHz, the crack propagated. After that repetition rate was increased to 200 kHz with the crack propagating further. No further degradation of the cell was observed even operating at full power. The standing wave and focused spot size data at 200 kHz repetition rate did not change from the previous results.

Because of the long and involved fabrication process for the bonded transducer, no further attempt was made to replace the cracked ATWL. Instead, a previously prepared SF-59 block with a 50° wedge and a LiNbO₃ transducer was assembled in a Q-switch mount. A half wave aluminum plate was used between the LiNbO₃ transducer and the SF-59. The transducer was pressed onto the ATWL by a small aluminum block and a screw.

The tuned transducer bandwidth in this case was only 0.5 MHz indicating the superiority of the bonded transducer approach where a bandwidth in excess of

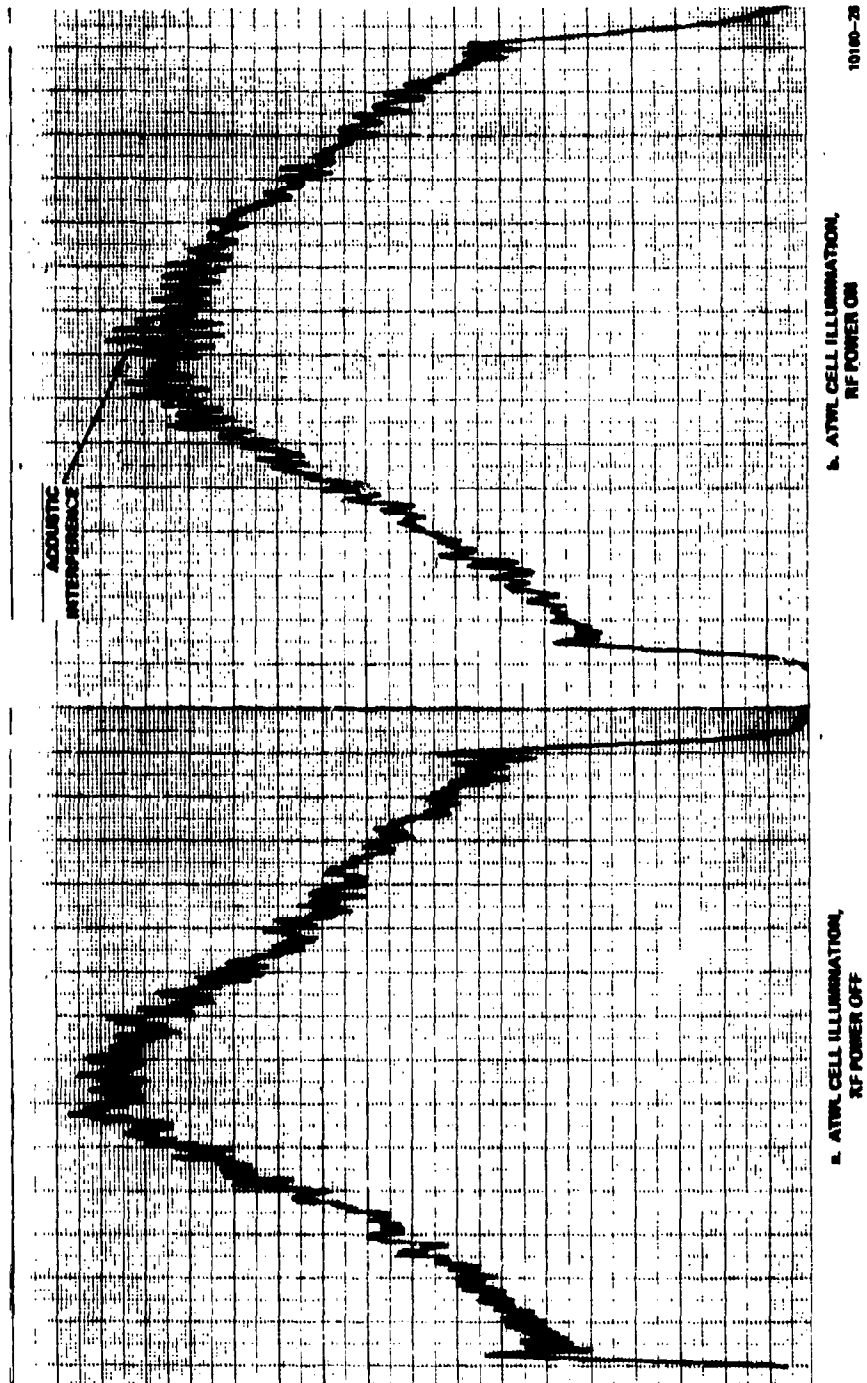


Figure 3.2.3-4. ATWL with a Wedged Surface

2 MHz was observed. The optical experiment showed a 20% increase in spot size in comparison to the previous results. The ATWL withstood the full power input. No cracking or degradation of the focused spot was observed after several hours of operation at full power level.

Figure 3.2.3-5 shows the RF wave form used to drive the ATWL. The first photograph shows the pulses occurring at the 200 kHz line rate. The second photograph shows the wave form in more detail. During our tracking experiments we would try to cause the scanning laser beam from the AOBD to track the central pulse shown. The RF waveform shown is the input to the ENI A-300 amplifier, where the average power output was 35 W. The waveform is similar to theoretical results described in Paragraph 3.1, however it was not optimized.

Figure 3.2.3-6 shows the profile of a focused spot from a 5° wedged, bonded transducer ATWL that was assembled in a Q-switch mount. The ATWL was not under a compression bias, and 400 watts of peak power was applied to the transducer. Note that the spot size for this case was about $14 \mu\text{m}$ at the FWHP

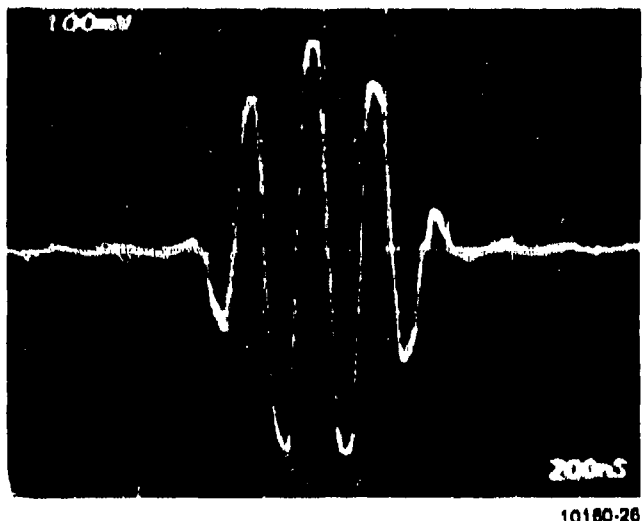
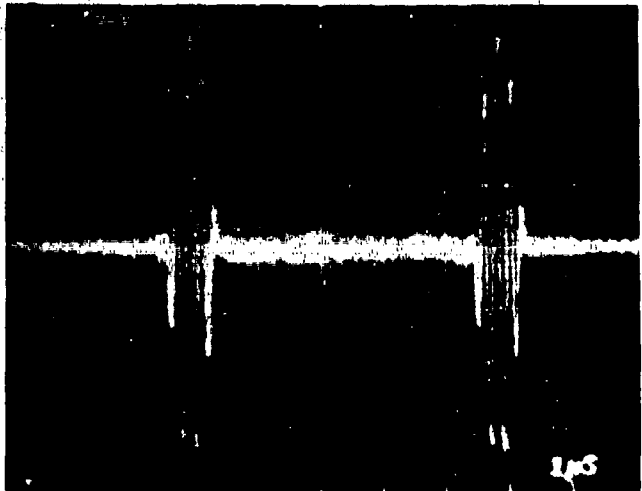


Figure 3, 2, 3-5. RF Pulse Used as the Input to the ATWL. The Average Input Power was 35W.

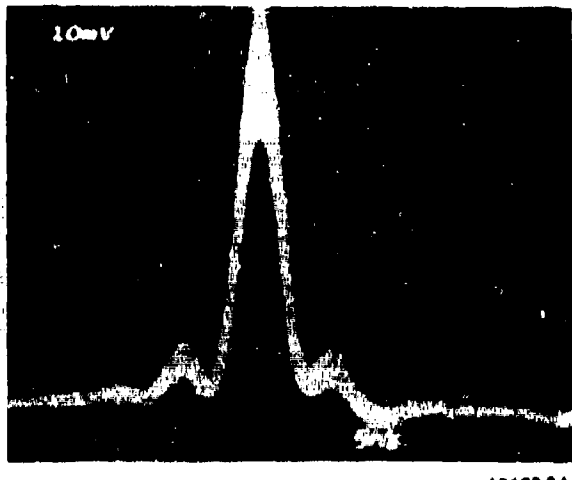
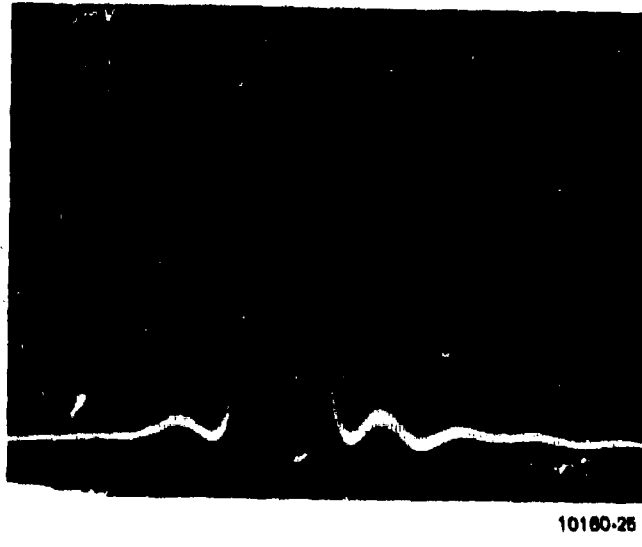


Figure 3.2.3-6. Profile of a Focused Spot From a 50° Wedged Bonded Transducer. ATWL Assembled in a Q-Switch Housing. point. The high side lobe level is due to the expanded beam illumination (nonscanning - no tracking). A smaller spot size and lower side lobes can be achieved with a tracking beam. This will be discussed in ~~Section IV~~. In our previous ATWL scanner development program 12-14 μ m spots could not be obtained without the use of compression bias. However, with an RF drive the same spot size has been achieved without compression bias and with one third the peak voltage to the transducer.

Figure 3.2.3-7 shows the spot profile from an ATWL with an unbonded transducer. Note the spot size in this case is about 16 μ m with the same drive



10160-25

Figure 3.2.3-7. Profile of a Spot From a 50 Wedged ATWL Cell,
With an Unbonded Transducer and Without Compression Bias.

The Cell Was Assembled in a Q-Switch Housing
power used for the bonded transducer case. The bonded transducer is definitely
superior in coupling the acoustic energy into the glass cell.

A summary of the work to develop the 200 kHz line rate ATWL is shown in Table 3.2.3. The main results that were obtained during this task are the following:

1. Gated RF excitation is far superior to the previously used stepped approach of charging the transducer to a high voltage and switching it to ground quickly.
2. Bonded transducers are more efficient in converting the electrical energy into useful acoustic energy
3. Compressing bias does not appear to be required for the gated RF drive
4. The affects of acoustic interference can be eliminated with careful design

5. Because of the high average power when the ATWL is operated at the full line rate design consideration for cooling the ATWL is required.

Table 3.2.3. Summary of the ATWL Development Task

<u>Experimental Device Description</u>	<u>Results</u>	<u>Remarks</u>
1. Old compression fixture design. Throughput 20-25 Percent PZT transducers, half-wave plates as electrode.		Connected using resin between all interfaces except on the compression fixture block.
2. Same as above with mylar and brass reflective stacks.	Throughput less than 6 percent	Connected using resin. Surfaces as available.
3. Same as in 1. with epoxy bonded W and Al reflective stacks.	Throughput less than 12 percent	Resin in between other surfaces.
4. Fused quartz with metallically bonded LiNbO ₃ transducers without compression bias. the input.	Throughput 64 percent. Reflection less than 1 percent as measured at	Electroded contacted with springs.
5. Same as above with PZT.	Very Low. PZT.	Questionable quality
6. SF-59 block with LiNbO ₃ transducer contacted with resin compression and half wave plates.	Operated satisfactorily. Obtained optical data. Presence of acoustic reflections. Throughput less than 25 percent.	Operated for a long period at full power without any deterioration.
7. SF-59 block with metallically bonded LiNbO ₃ transducer. Under compression.	Less than 3 percent losses at the input-output. Throughput 50 percent; less than 1 percent reflection as observed at the input end	Cracked in testing.
8. Bonded transducer SF-59 cell with 5° wedge and under compression bias.	No reflections seen by electrical means.	Cracked after some optical test due to heat build up.

Table 3.2.3. Summary of the ATWL Development Task (Continued)

<u>Experimental Device Description</u>	<u>Results</u>	<u>Remarks</u>
9. Bonded transducer with 50° wedge assembled in Q-switch housing.	Obtained 13 μm spot. Once the cell stabilized operated under full power for a long period. No further deterioration. Clear aperture exists for full scanning.	Cracked at corners while assembling. Crack propagated when operating.
10. Contact transducer with Q-switch assembly.	Obtained focused spot but not as good as in 9. ATWL operating at full power level. Reflections present but reduced in amplitude.	Operational cell.

3.3 Development of Electronic Design

3.3.1 AOBG Driver Requirements

The AOBG used in the laser scanner system requires a 2.0 watt drive signal which is swept in frequency from 80 to 120 MHz. The AOBG driver specification requires that the rate at which the frequency range is swept be 200 kHz with a 98 percent duty cycle. This corresponds to a time scan of 5 μ sec with only 0.1 μ sec allowed for flyback. This dictates the need for two VCO's which are time multiplexed to produce the 200 kHz repetition rate for the scanner. This method allows one VCO to flyback while the other is sweeping. Also required is the ability to vary the bandwidth of the VCO outputs.

3.3.2 AOBG Electronics Description

A functional block diagram of the AOBG electronics is shown in Figure 3.3.2-1. All control signals for the electronics are derived from a 96 MHz

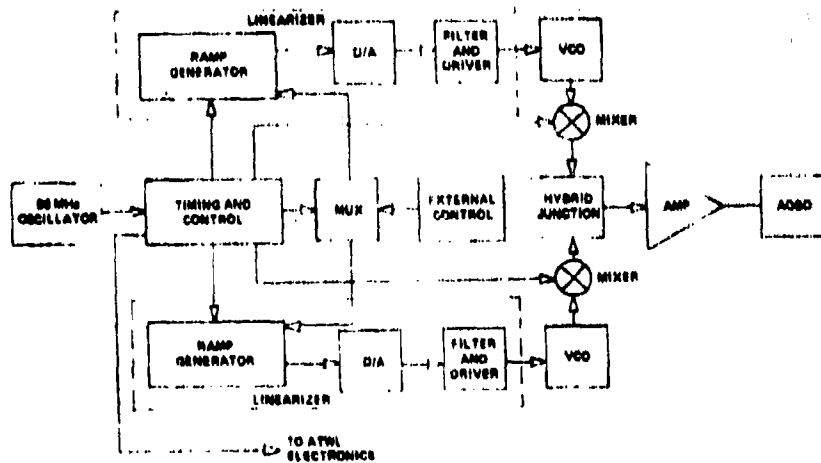


Figure 3.3.2-1. AOBG Driver Electronics

precision oscillator. The two VCO's are time multiplexed to give a 200 kHz, 98 percent duty cycle repetition rate. The outputs of the VCO's are gated on and off

through the mixers, which act like RF switches, and are summed at the hybrid junction. This junction provides approximately 40 dB isolation in the off state, effectively isolating the two VCO's from each other. The output of the hybrid junction is then amplified to produce the required 2.0 watt RF signal to drive the AOBD.

In order to drive the VCO's, special linearization circuits are incorporated that produce a linear sweep. A typical VCO tuning characteristic curve is shown in Figure 3.3.2-2. The linearizer circuits can be programmed in such a way as to produce a nonlinear ramp to drive the VCO's, which effectively offsets the nonlinearities of their tuning characteristics. A linear sweep is then obtained. Since each VCO has a slightly different tuning characteristic, two linearizer circuits were required. Only one programmer was used, however, to program the circuits. This programmer is multiplexed between the two circuits, which makes the system easier to operate.

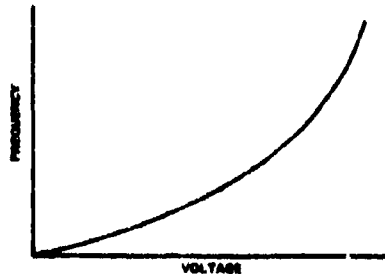


Figure 3.3.2-2. Typical VCO Tuning Characteristic

As shown in Figure 3.3.2-1 the linearization circuit consists of a ramp generator, a digital to analog converter (D/A), and a filter and driver.

3.3.3 Voltage-Controlled Oscillators

The most important component in the AOBD driver is the voltage-controlled oscillator (VCO). The linearity of the AOBD scan is directly

proportional to the linearity of the frequency sweep of the VCO. The two oscillators used in this program were Texscan model VTS 205. The tuning linearity was specified at $\pm 10\%$ with a frequency stability of 250 PPM/°C. The power variation was 2 dB over the frequency range of 80 MHz to 120 MHz.

When these oscillators were first tried, it was found that they could not be swept at the 200 kHz rate that our specification required. After consulting with Texscan, it was found that the VCO's had not been set up at the factory to be swept at 200 kHz. The highest possible sweep rate was only 20 kHz. However, with only a slight modification the VCO's could be swept at a higher sweep rate. It was decided that due to the delays in the shipment of the VCO's from Texscan, it would be to the program's benefit to modify the VCO's in-house instead of sending the VCO's back to Texscan for modification. The modification for the VCO's is shown in Figure 3.3.3. The input was changed to provide a lower input impedance and lower input capacitance to accept a faster sweep rate. The

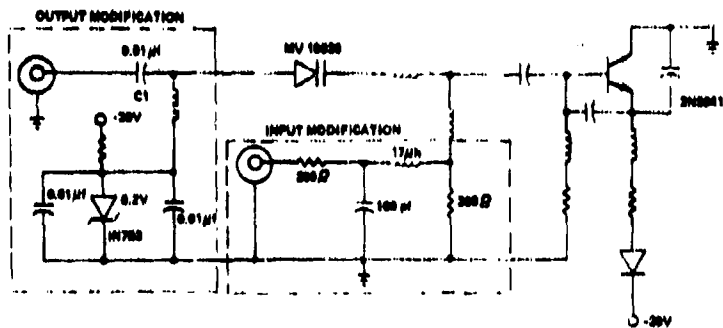


Figure 3.3.3. Modified VTS -205 Voltage Controlled Oscillator

17 μ H inductor was incorporated as part of the input filter to decouple the RF from the VCO drive circuit. After this was done it was found that the bandwidth and center frequency of the VCO had shifted considerably from what was required.

After some time at trying to retune the VCO, it was decided that the tuning characteristic had changed considerably. Therefore, it was necessary to put a negative bias on the varactor to bring the tuning curve down to a useable position. The 6.2 volt Zener diode provides this bias. It was then necessary to AC couple the output of the VCO to remove the DC offset from the RF. This is provided by capacitor C1. Some time was spent in making these modifications but the necessary bandwidth and center frequency, along with the appropriate tuning curve, were achieved. The same modifications were made to the other VCO and similar results were obtained. Due to the experimentation with the first VCO to determine the needed modifications, it was necessary to replace its transistor and varactor. Damage to these components resulted when the VCO was left off its heat sink (which was necessary during the experimentation) and the soldering that was done to the varactor when installing the components needed for the modification. However, after the new transistor and varactor were installed in the first VCO, both VCO's have been working properly up to the present time.

3.3.4 VCO Linearization

Since the linearity specification was not established for the AOBD, it was decided to linearize the VCO's to a reasonable value that would be acceptable for the breadboard experiments. The linearization method used here has the capability of linearizing a VCO to 0.01 percent over an octave tuning range. However, this requires additional time spent in programming the linearizers.

A functional block diagram of the linearity measuring technique is shown in Figure 3.3.4-1. This method involves a somewhat indirect method of deriving a difference frequency from the frequency sweep and comparing that frequency with a reference frequency. The output of the VCO can be expressed as

$$A_1 \sin 2\pi \frac{\Delta f}{\Delta t} t^2,$$

3.3.4-(1)

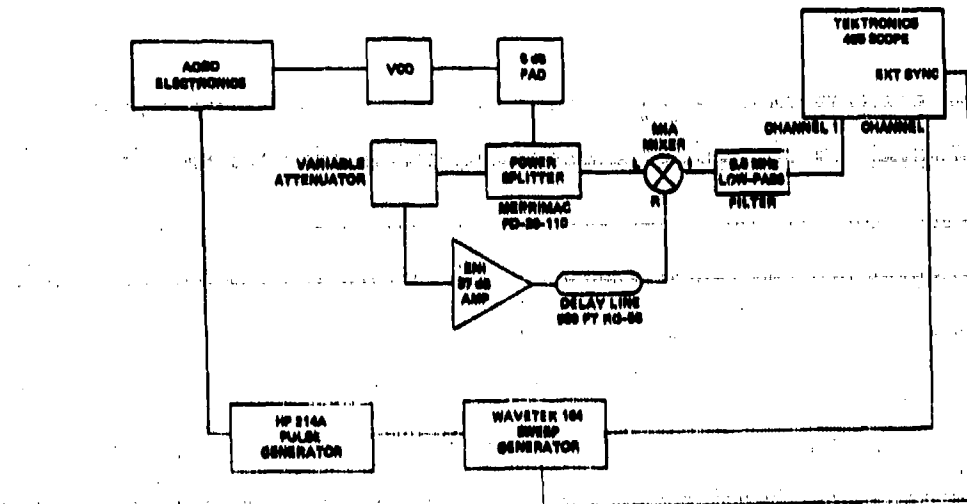


Figure 3.3.4-1. VCO Linearization Measuring Technique

where Δf is the bandwidth swept by the VCO. In this application Δf is 40 MHz. Δt is the time required to complete one full frequency sweep, or scan, which is 5 μ sec. The VCO output is split, using a Merrimac PD-20-110 power splitter. One output is delayed by a 750 ns delay and inserted into the "R" port of a RELCOM MIA mixer. The other output of the power splitter is input to the "L" port of the same mixer. The "I" port of this mixer then yields the product of the two inputs. The delayed input is of the form

$$A_2 \sin 2\pi \frac{\Delta f}{\Delta t} t(t-T_D), \quad 3.3.4-(2)$$

T_D is 750 ns, the amount of delay in the cable delay line. Derivation of the product is as shown.

$$\begin{aligned}
 & \left[A_1 \sin 2\pi \frac{\Delta f}{\Delta t} t^2 \right] \left[A_2 \sin 2\pi \frac{\Delta f}{\Delta t} t(t-T_D) \right] \\
 = & \frac{A_1 A_2}{2} \cos \left[2\pi \frac{\Delta f}{\Delta t} t^2 - 2\pi \frac{\Delta f}{\Delta t} t(t-T_D) \right] - \frac{A_1 A_2}{2} \cos \left[2\pi \frac{\Delta f}{\Delta t} t^2 + 2\pi \frac{\Delta f}{\Delta t} t(t-T_D) \right] \\
 = & \frac{A_1 A_2}{2} \left[\cos 2\pi \frac{\Delta f}{\Delta t} t T_D - \cos 2\pi \frac{\Delta f}{\Delta t} t (2t - T_D) \right]
 \end{aligned} \tag{3.3.4-(3)}$$

The second term $\frac{A_1 A_2}{2} \cos 2\pi \frac{\Delta f}{\Delta t} t (2t - T_D)$ is the sum term, and it is a sweep component starting at 120 MHz. This term is not used, but the first term $\frac{A_1 A_2}{2} \cos 2\pi \frac{\Delta f}{\Delta t} t T_D$ is used.

Substituting the values of Δf , Δt , and T_D into this expression yields the frequency of this component which is 6 MHz. The Hewlett-Packard 214A pulse generator in Figure 3.3.4-1 is triggered by the same pulse that initiates the VCO sweep. The output from the pulse generator is input to the Wavetek 164 sweep generator. The sweep generator is put in the triggered-gated mode such that the pulse from the signal generator gates a 6 MHz CW signal from the Wavetek.

The output of the mixer is input to a 6.5 MHz low-pass filter that removes the unwanted sum frequency. The difference frequency is then connected to a vertical amplifier on a Tektronix 485 oscilloscope. The reference signal output from the Wavetek is connected to the second vertical amplifier and the two waveforms are superimposed on the scope screen, and compared. The "pulse delay" on the signal generator can be adjusted to provide time coincidence between the two

waveforms. It is obvious from the expression $\frac{A_1 A_2}{2} \cos 2\pi \frac{\Delta f}{\Delta t} T_D t$ that, if the

ratio $\frac{\Delta f}{\Delta t}$ remains constant, the frequency remains constant and conversely if the ratio changes, the frequency changes. A constant ratio of $\frac{\Delta f}{\Delta t}$ indicates a linear sweep; therefore, regions where the linearity is correct will appear as a constant frequency of 6 MHz.

Once the test setup for measuring linearity is connected, the operator should use the delayed sweep on the oscilloscope to expand the time scale of the two superimposed sine waves. The delay vernier should then be adjusted to allow viewing of the last 500 ns of the scan. An address corresponding to this location can then be entered into the Address switches. The start of scan corresponds to word 0, and the end of the scan corresponds to word 80. As a result, a point 4.5 μ s into the scan will correspond to word 72. Any arbitrary value can then be entered into the Data switches, and the Load button depressed. The effect on the difference frequency can be observed on the oscilloscope. The goal is to make the two sine waves coincident. Different data values should be tried until an optimum value is found, then the address switches should be incremented by one, and another value entered. If the last 500 ns cannot be linearized, a gain adjustment should be made to the driver circuit, and linearization again attempted. This procedure should be continued until the correct gain setting is determined. After this has been accomplished, the operator should then move the delay vernier on the oscilloscope until the first portion of the scan is visible. Address 0 should be entered, and data values tried until linearization is accomplished at this location. It may be necessary to adjust the pulse delay on the pulse generator to obtain time coincidence between starting points of the two waveforms. The operator then proceeds to sequentially step through the addresses, linearizing each of the 80 segments of the scan.

Both VCO's were linearized using this technique. The driver circuit including the digital-to-analog converter was put on a printed-circuit board, for

each VCO. These circuits, along with the VCO's, were placed in temperature controlled ovens to achieve temperature stability, as shown in Figure 3.3.4-2.

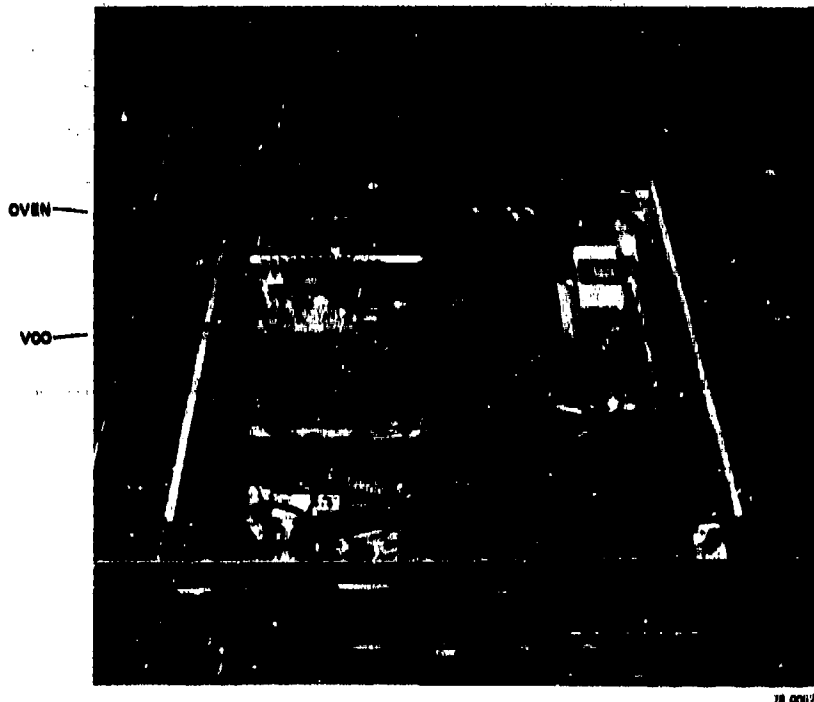


Figure 3.3.4-2. Photograph of the Drive Control for the AOBD/ATWL

However, it was found that the VCO's dissipated too much heat to be placed inside the oven with the driver circuits. The VCO's were relocated to a heat sink outside the ovens. No further attempt to stabilize the VCO's was made. However, a temperature controlled heat sink could be used with each VCO to achieve stability. This was not done since extreme chirp linearity was not a crucial parameter in this program.

The outputs of the VCO's were each attenuated with a 30 dB pad, and input to the Relcom M1 mixers. The mixer outputs were routed to the ANZAC H-1-4

hybrid junction and then to a TRW CA801, 30 dB amplifier. This provides the 0.5 watt drive signal for the AOBD.

3.3.5 ATWL Driver Requirement

The ATWL used in the laser scanner system requires a 4.8 MHz gated RF signal at a repetition rate of 200 kHz. The amount of power required to drive the ATWL is provided by a 300 watt ENI amplifier, capable of providing 400 watts, typically.

3.3.6 ATWL Electronics Description

A functional block diagram of the ATWL electronics is shown in Figure 3.3.6. The timing signals are derived from the same timing and control electronics as the AOBD; therefore, the ATWL is synchronous with the AOBD.

The timing signal is derived from the multiphase clock in Figure B-3, Appendix B. The 200 kHz rate is the input to a series of two one-shots. These one-shots provide for a variable gate width and a variable delay from the start of the AOBD scan to help achieve tracking between the AOBD and ATWL. This signal is then input to the transistor circuit which provides the proper level and drive capability for the mixer. The filter on the output of the transistor was not originally included. However, it was later determined experimentally that if the gated RF had a rounded envelope instead of a square envelope, less reflections occurred in the ATWL. This filter provides a rounded pulse, variable in height, that gates the 4.8 MHz signal through the mixer.

This signal is then input to a power splitter (Figure 3.3.6). One output is routed to a variable attenuator and then to the ENI A300 amplifier. This 300 watt amplifier has approximately 55 dB of gain and provides the power needed to drive the ATWL. The other output of the power splitter is input to the ATWL protection circuitry. The need arose for a protection circuit while experimentation was being done on the ATWL. When the gating pulse was expanded to

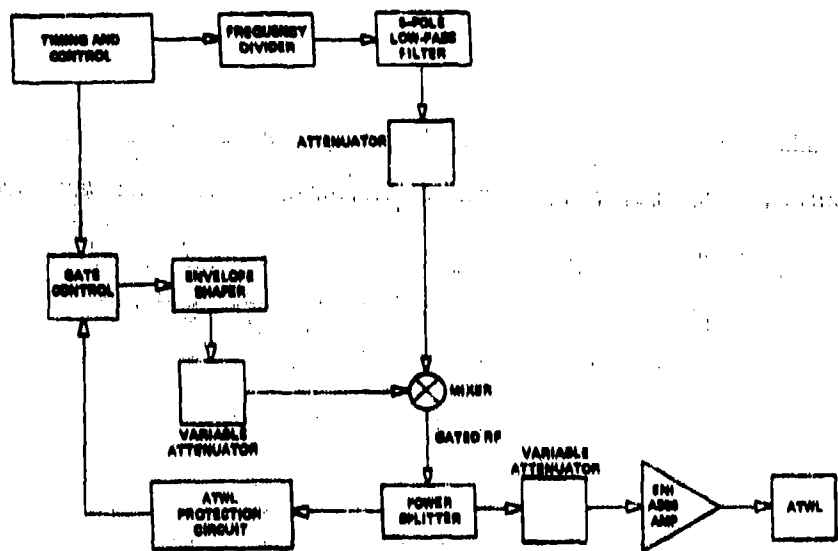


Figure 3.3.6. ATWL Driver Electronics

allow more cycles of the 4.8 MHz signal through to the ATWL, a point would be reached where the average power input to the device would be too great and would cause the ATWL to crack. This type of situation, whether caused by human error or electronic failure, dictated the need for the protection circuit. This circuit is shown in Figure B-11, Appendix B. The effect of the protection circuit is to shut down the ATWL electronics if more than 10 cycles RF are input to the device in any one scan. This number was experimentally determined and could be changed.

3.3.7 Spinner Synchronizing Electronics

A circuit was required to synchronize an Y-scan spinner to the system electronics. The purpose of this circuit was to allow one Y-scan at a time to be initiated manually. This circuit is shown in Figure B-11, Appendix B. A detector was mounted on the spinner to count each facet as it passes by. The output of the detector is input to the comparator and converted to a TTL level. This signal is

then used as the clock input to the counter. The output from this counter is input to the acousto-optic modulator (AOM) mixer, which is turned off.

To produce one Y-scan, the operator activates the RUN switch which enables the counter. The next pulse from the detector is counted and turns the AOM mixer on. The second detector pulse is counted and loads itself with 14 again. This also disables the counter and turns off the AOM mixer. The RUN switch must be activated for each scan.

4.1

Breadboard Experiments

A laser scanner breadboard system based on the design of Section II was assembled using Harris owned equipment. A photograph of the laser scanner breadboard is shown in Figure 4.1. The breadboard was used to demonstrate the 100 percent duty scan from the AOBD, to perform AOBD/ATWL tracking experiments, and was used to measure the optical efficiency of this approach. Although a 15



78-0081C

Figure 4.1 Laser Scanner Breadboard

faceted spinning mirror was available for performing X-Y scanning onto a recording medium, these experiments were not performed on this program; such experiments could be performed with additional funding. An Itek PROM was made available for recording experiments in the laser scanner; however it was not used in the

breadboard system. (A functional test of the PROM was performed and is reported in Appendix C.)

4.2 AOBD/ATWL Tracking Experiments

The basic idea involved in increasing the resolution capability of an AOBD scanning system is to cascade the acousto-optic devices. In order for this technique to work properly, it is essential that the scan velocity of the AOBD be precisely matched to the acoustic propagation velocity of the traveling lens in the ATWL. Therefore careful adjustment of the optics between the AOBD and the ATWL is required to achieve tracking.

Several experiments were performed to achieve tracking across the full aperture of the ATWL cell. This would correspond to 1000 spots or $5 \mu\text{s}$ scan time. On several occasions we achieved $1.5 \mu\text{s}$ of AOBD/ATWL tracking. This corresponds to 300 to 375 spots, depending on the drive power to the ATWL. We discovered the main reason for the failure of the optical system to track over a larger aperture was due to aberrations of one of the lenses in the telescope. The only way to increase the tracking was to obtain a replacement lens that was diffraction limited over a larger aperture. We found that this approach was very cumbersome, compared to the method that has been previously used to achieve AOBD/ATWL tracking over 18,000 spots and a 9-inch aperture. In an earlier laser scanner, the linearity of the output from a voltage controlled oscillator (VCO) that is used to drive the AOBD was adjusted so that the scan rate at the ATWL matched the velocity of the traveling lens. The electronic adjustments could compensate for some nonlinearities in the scan caused by lens aberrations. However, in the present breadboard system we do not have this capability. Because of the inflexibility of the optical tracking approach, we do not recommend its use on future scanner efforts.

An experiment was performed to demonstrate the 100 percent duty scan from the AOBD where the dead time between the two VCO's was adjusted to be only 20 ns producing 99.6 percent active sweep by the VCO's. However, by adjusting the slit width in the Fourier transform plane of the AOBD, 100 percent scan can be achieved using the traveling chirp scan approach. We found that the traveling chirp from each VCO as measured at the ATWL output plane repeated its scan every 10 μ s. However, when alternate VCO's were used to produce a scanning spot every 5 μ s, we found that the scans did not interleave exactly (4.8 μ s between two consecutive spots and 5.2 μ s between the next pair of spots). This interleave problem was caused by the fact that the VCO's were not matched accurately enough in both center frequency and bandwidth. VCO's can be purchased that are matched to each other. This parameter was not adjusted due to lack of funds and insufficient time.

From our experience with using the traveling chirp approach, we suggest an alternative approach that is easier to fabricate and less expensive in the long run. The alternative approach is to use two AOBD's fabricated in the same cell and to switch from one AOBD to the other. As one AOBD is approaching the end of its scan, the second AOBD is loaded with the chirp signal. A two spot AOM is used to switch the laser beam from one cell to the adjacent cell (only a few millimeters away); electronic tracking can be used with this approach. An added benefit of this approach is that the optical efficiency of the AOBD should increase by as much as 50 percent, since diffraction occurs along the entire length of the cell to form a spot (in the other approach, diffraction occurs only along the traveling chirp).

Optical Efficiency Measurements

The optical efficiency is defined as the percent of the incident laser illumination that passes through the system and arrives at the film plane. The overall optical efficiency of the system was measured and found to be 5 percent of the input laser power. The power measurements were made by collecting all of the light onto the sensor of a Model 212 Coherent Radiation Power Meter. The optical efficiency measurements were made at individual components, and the results are shown in Table 4.4. Note that the least efficient element in the system is the AOBD, as would be expected. This element could be improved slightly, however, because of the traveling chirp approach - 50 percent is the theoretical maximum efficiency this element can have. The AOM efficiency is also low (50 percent assumed) to keep the intermodulation product of the drive signal at a reasonably low level. However, if the intermod noise is required to be about 40 dB down, the maximum optical efficiency of the AOM will be less than 10 percent; with this requirement the overall optical efficiency is only 1 percent.

Improvements could be made in the AOBD efficiency either by making the transducer wider or by using an amorphic lens arrangement to focus the light in the nonscanning direction to a smaller (thinner) line. The illumination was slightly wider than the transducer; therefore, the efficiency was somewhat low even at the high drive power levels (3 W). Another way to improve the efficiency

Table 4.4. Optical Efficiency Measurements

<u>Optical Component</u>	<u>Element Efficiency (%)</u>	<u>SYSTEM EFFICIENCY (%)</u>
1. Laser	-	100 %
2. Mirror M_1	99.6	99.6
3. Mirror M_2	99.6	99.2
4. AOM	50	49.6
5. Cylindrical Lens C_1	96.3	47.8
6. Cylindrical Lens C_2	96.3	46.0
7. AOBD at 3 W Special Lens L_1 Prism P_1	17.8	8.2
8. Telescope T_1	94.1	7.7
9. Telescope T_2	96.9	7.5
10. Mirror M_3	99.6	7.4
11. Cylindrical Lens C_3	99.6	7.4
12. ATWL	78.5	5.8
13. Lens L_2	96.9	5.6
14. Spinning Mirror	98	5.5
15. Lens L_3	<u>96.9</u>	<u>5.3</u>
TOTAL Optical Efficiency		5.3%

is not to use the traveling chirp approach; two AOBD's separated by a couple of millimeters in the same cell, using the AOM to switch from one AOBD to the other, could be far more efficient - approaching 90 percent.

The ATWL is also a relatively low efficiency device (78.5 percent). This is caused by the reflection and absorption of the light by the SF-59, which is a yellow looking glass. This element could be improved by using other materials that are optically clear and by antireflection coating of the optical surfaces.

With a system transmission efficiency of about 5 percent, the required laser power can be calculated for a given recording material from the following expression.

$$P_L = \frac{SA}{\eta T}$$

where:

P_L = Average laser power

S = Recording medium sensitivity

η = System optical efficiency

T = Pixel exposure time

A = Area of focused spot

For a sample calculation, the following typical values will be used:

S = 60 ergs/cm² (sensitivity of elastomer device)

A = 2×10^{-6} cm² (14 μ m spot)

η = 5%

T = 5 ns

The required laser power is 48 mW. This formula should apply to any other recording material.

SECTION V CONCLUSIONS

A number of conclusions are drawn from this study relating to the feasibility of using an ATWL laser scanner system for signal processing applications. First, we discuss the conclusions that were reached concerning the individual components of the laser scanner (i.e., the ATWL, AOBG, and AOM) and then we discuss the overall system performance.

The ATWL performed very well with the RF drive with the exception of two problems that were encountered. The first problem was the overheating of the ATWL cell causing it to crack; this problem was eventually solved with sufficient cooling of the glass cell, particularly the sides. The second problem was the acoustic interference caused by the reflection at the opposite end of the cell at the high repetition rates. The acoustic interference was significantly reduced by cutting the end of the cell at an angle relative to the transducer. The cell operated at the 200 kHz line rate, which is the highest rate that an ATWL has operated. Another important conclusion is that the ATWL can be operated without a compression bias when using the gated RF drive. This makes the ATWL device much smaller and simpler to fabricate. The last and probably most important conclusion is that the gated RF drive is at least three times more efficient than the old stepped approach used in the past, therefore smaller, lighter amplifiers can be used to drive the cell.

The AOBG traveling chirp approach was a success; however, tracking of the AOBG and ATWL was difficult and the diffraction efficiency was low. We conclude that because of the low optical efficiency and the difficulty in achieving full aperture tracking, we would not recommend this approach on a future breadboard scanner system. The electronic drive performed well at the 200 kHz line rate where a 20 ns dead time existed between the chirps. The traveling chirp

requires that the two VCO's be matched fairly accurately in center frequency and bandwidth. In our system the center frequencies were not well matched causing adjacent scan lines to occur at $4.8 \mu s$ or at $5.2 \mu s$ periods but not at $5.0 \mu s$. The matching problem would have to be resolved if the traveling chirp approach is to be used on a future system. Another problem that should be addressed is achieving uniform light level across the scanning aperture. This problem was not addressed in this study.

The wideband AOM was not developed on this study. However a Harris wideband AOM was made available to be used in the breadboard system. The diffraction efficiency of the device was measured and the intermodulation noise was measured using two input signals. The results verified the data reported by Hecht¹¹. From this we can conclude that the optical efficiency of the AOM cannot be greater than 10 percent if the intermods are to be down at least 40 dB.

The optical breadboard system was used to determine the difficulty in a AOBD/ATWL tracking and served as a baseline measure of the optical efficiency. The scan tracking lens telescope was assembled and evaluated in the breadboard. We found that it was not possible to achieve tracking over the full ATWL aperture because of aberrations in one of the lens elements. We concluded that diffraction limited lens elements with low distortion are required to cause the AOBD/ATWL to track (this approach is fairly inflexible to any changes in temperature and to glass variations). We do not recommend this approach on future scanner systems; instead, we recommend the dual AOBD approach with electronic tracking control.

SECTION VI

RECOMMENDATIONS

We recommend that a working breadboard system be assembled to test the end-to-end problems of recording wide bandwidth signals onto a temporary recording medium. This end-to-end breadboard would be used to measure the system dynamic range, scan linearity, and to determine the level of the intermods as seen in the Fourier transform plane. We recommend the use of dual AOBD's to achieve the 100 percent duty scan. A different recording format is recommended to achieve a slower line rate. The ATWL is capable of recording several thousand spots per scan line. This would reduce the heat buildup problem. The system efficiency problem should be studied in more detail. The electronic tracking approach is recommended because of its versatility and proven usefulness over large apertures.

This technology appears to have excellent growth potential with resolutions of $8 \mu\text{m}$ spots and recording bandwidths of 400 MHz being realizable. However, a number of engineering questions have been raised in the breadboard investigations; these questions must be answered to minimize the technical risk and ultimately the cost involved in developing such systems. Consequently, we suggest a program during which we reassemble and modify the existing breadboard to perform certain experiments to answer the questions and to use the results as the basis for a complete system design.

The advantageous features of an ATWL laser recorder can be summarized as follows:

- High Speed $>10^8$ pixels/second
- High Resolution 18,000 pixels/line ($10 \mu\text{m}$ spots)
- No Moving Parts Acousto-optic elements are reliable and long lived

- Flat Field Traveling lens can be the final optical element
- Excellent Linearity Inherent in Traveling Lens
- Cost Low projected recurring cost

Most of the experimental results with an ATWL system have been with devices fabricated of SF-59 glass which has a figure of merit $M = 19$. Other materials that have a higher figure of merit should be investigated to determine how well they perform as an ATWL. A list of other materials that should be investigated are listed below in Table 6.1. Note that the index, velocity, and the figure of merit are given for each material. The effective spot size is calculated as shown in Column 5 of the table, where we assume the peak acoustic intensity is the same for all the materials and the wavelength is assumed to be 514.5 nm. From the table, water appears to be one of the best materials based on this comparison. However, to prevent cavitation and bubble formation in the water, the ATWL would have to be pressurized to many atmospheres. This creates a number of engineering problems that would have to be solved before a water cell could be used at high acoustic power levels. Also for some applications the acoustic velocity would be too slow. Note in the last column the effective bandwidth of the cell is given, e.g., the acoustic velocity of the material is divided by the spot size to obtain the number of spots per second (the bandwidth) for each material listed. Even though the effective spot size is the smallest with water it also has the smallest bandwidth. The material listed with the broadest bandwidth is As_2S_3 , however, As_2S_3 can only be used with a red laser (e.g., 632.8 nm) or longer wavelengths. This criteria may cause a system

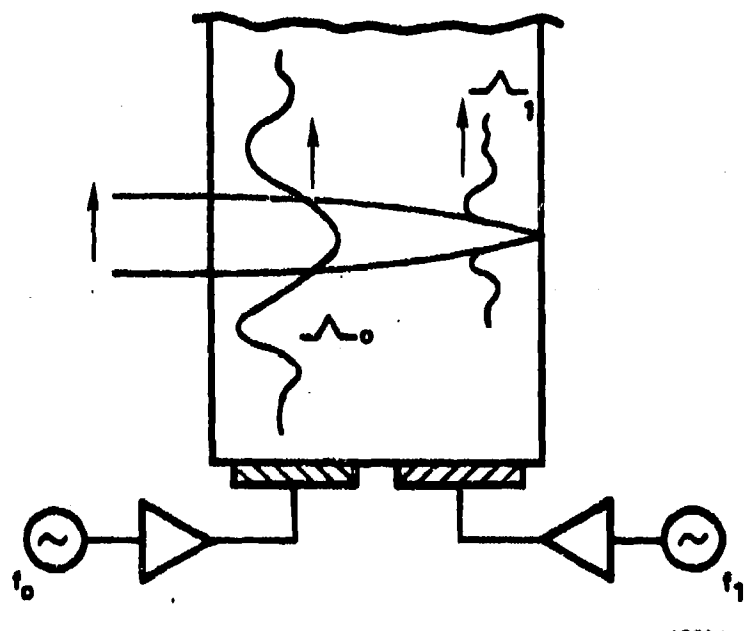
Table 6.1

<u>Material</u>	<u>Index</u>	<u>Velocity mm/μs</u>	<u>Figure of Merit 10⁻¹⁸ s³g</u>	<u>Effective * Spot Size μm</u>	<u>Effective Bandwidth MHz</u>
SF-59	1.95	3.2	19	14.6	219
As ₂ S ₃	2.61	2.6	433	7.7	337
Water	1.33	1.49	126	7.5	198
PbMoO ₄	2.262	3.63	36.3	13.4	270
PbMoO ₅	2.183	2.96	127	9.6	308
Ag ₃ AsS ₃	2.98	2.65	390	8.5	311

*Assume same acoustic intensity in each material, and $\lambda = 633$ nm.

problem where many output recording materials are insensitive to the longer wavelengths.

Another way to increase the resolution of the ATWL is to increase the focusing power of the traveling lens while at the same time reducing the aberrations. This may be accomplished by using a multielement traveling lens. For example, the traveling lens nearest the AOBO would have a long acoustic wavelength so that the input beam diameter would be $\Lambda_0/4$ for the first acoustic lens. The light ray trajectories passing through the traveling lens follow approximately a parabolic path. Figure 6.1 shows a diagram of a multielement ATWL where the second traveling lens is driven with a higher frequency gated RF signal so that $\Lambda_1/4$ matches the beam diameter at that position. The two traveling lenses working together should cause the beam to focus to a much smaller spot. The problem can be computer-simulated to determine the optimum drive frequencies required to reduce the aberrations and produce the smallest spot in the output plane. For example if an 8μ m spot could be produced in SF-59 glass, then the bandwidth of the cell would increase to 400 mega pixels/second.



10085-1

Figure 6.1. Multielement ATWL

Appendix A

Transducer Impulse Response

The frequency response of the transducer, that is, the strain in the lens medium produced by a harmonic electric displacement, is

$$H(\omega) = \gamma \frac{1 - \cos(\omega d/v_1) - i b \sin(\omega d/v_1)}{\sin(\omega d/v_1) - i e \cos(\omega d/v_1)}, \quad (A-1)$$

where γ , b and e are constants. Changing variables to $x = \omega d/v_1$ and defining $y = v_1 t/d$, the impulse response is

$$H(t) = \int_{-\infty}^{\infty} H(\omega) e^{i\omega t} d\omega = \frac{v_1 \gamma}{d} \int_{-\infty}^{\infty} \frac{1 - \cos x - i b \sin x}{\sin x - i e \cos x} e^{ixy} dx \quad (A-2)$$

Consider the last integral over the entire contour of Figure A-1, in the upper

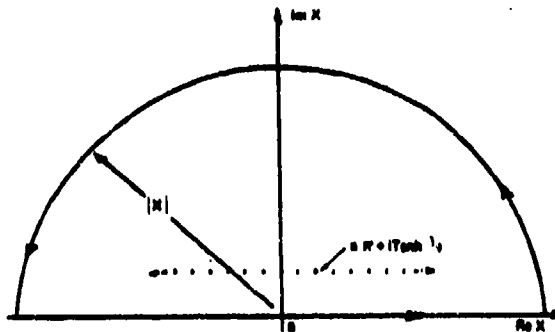


Figure A-1. Contour of Integration for Evaluation of Impulse Response half complex plane. For $y > 0$ (positive time) the integral over the semicircle goes to zero as $|x| \rightarrow \infty$. The remaining integral is that of Equation (A-2) so that

$$H(t) = \frac{v_1 \gamma (2\pi)}{d} \sum_{n=0}^{\infty} R_n, \quad (A-3)$$

where R_n are the residues of the poles at

$$x_n = n\pi + i \tanh^{-1} e, \text{ if } e < 1; \quad x_n = \frac{2n+1}{2}\pi + i \tanh^{-1}(1/e), \text{ if } e > 1 \quad (A-4)$$

Since e is positive, there are no poles in the lower half plane, and therefore a semicircular contour in the lower half plane shows that $H(t) = 0$ for all $t > 0$; the transducer cannot predict a pulse. Taking, for the moment, the case $e < 1$, the residues are found to be

$$R_n = \frac{(-1)^n \sqrt{1-e^2} - (1-be)}{1-e^2} \exp \left\{ i n \pi y - y \tanh^{-1} e \right\} \quad (A-5)$$

Using the relations

$$\exp \left\{ -y \tanh^{-1} e \right\} = \left(\frac{1-e}{1+e} \right)^{t/2} \quad (A-6)$$

$$\lim_{N \rightarrow \infty} \sum_{n=1}^{\infty} e^{i \theta n} = \sum_{m=-\infty}^{\infty} \delta(\theta - m\pi) \quad (A-7)$$

Equation (A-3) leads to

$$H(t) = [4\pi D_0 h v_1 / c_3 (1+ab)] \left\{ \frac{1}{1+e} \sum_{n=1}^{\infty} \left(\frac{1-e}{1+e} \right)^n \delta[t - (2n+1)\tau] \right. \\ \left. - \frac{1-be}{(1+e)^2} \sum_{n=1}^{\infty} \left(\frac{1-e}{1+e} \right)^{n-1} \delta[t - 2n\tau] \right\} \quad (A-8)$$

for $t > 0$. The $t = 0$ term is obtained from the boundary condition $T_1(d) = T_2(d)$, or, equivalently,

$$c_2 S_2 = c_1 S_1 - hD \quad (A-9)$$

and the fact that $S_1(d)$ at $t = 2T$ is related to $S_1(d)$ at $t = 0$ by a transducer round trip traversal including a reflection. Some algebra shows that the $t=0$ term is

$$H_0(t) = \left(\frac{-2\pi h D}{c_2} \right) \cdot \left(\frac{a}{(1+a)} \right) \delta(t) \quad (A-10)$$

With

$$e = (a+b) / (1+ab) \quad (A-11)$$

and

$$\frac{1-a}{1+a} = \left(\frac{1-a}{1+a}\right) \left(\frac{1-b}{1+b}\right) = r_2 r_3 \quad (A-12)$$

we have

$$H(t) = 4[\pi D_{0ha} / c_2(1+a)(1+b)] \times \left\{ -\frac{1+b}{2} \delta(t) + \sum_{n=0}^{\infty} (r_2 r_3)^n \delta[t-(2n+1)T] \right. \quad (A-13)$$

$$\left. - \left(\frac{1-b}{1+a}\right) \sum_{n=1}^{\infty} (r_2 r_3)^{n-1} \delta[t-2nT] \right\}, \quad (A-13)$$

where $T = d/v_1$.

APPENDIX B
ELECTRONIC DESIGN

The circuitry shown in Figures B-1, B-2, and B-3, is the timing and control electronics. As mentioned previously all timing signals are derived from a 96 MHz oscillator which is not synchronized with the laser. The circuit in Figure B-1, translates the 2 volt peak-to-peak sine wave into a TTL level square wave. Flip-flop U1A receives the 96 MHz TTL signal and divides it by two to present a 48 MHz signal to flip-flop U1B and divide-by-three circuit of U3A and U3B. The output of U1B is a 24 MHz signal which is input to the circuit in Figure B-3. The output of U3B is a 16 MHz signal which is used to clock the counters in Figure B-4.

Counters U5 and U4 in Figure B-3, receive the 24 MHz signal and divide it by 12, thus inputting a 24 MHz signal to U15. Counter U15 and decoder U14 further divide the signal by 10. The output of U14 is a multiphase clock at 200 kHz. This is the frequency at which the AOBD driver will operate. However, since each VCO is only operating at half the repetition rate, a 100 kHz signal to gate the VCO driver circuits on and off is provided at the outputs of U12A and U12B. These signals are two phases of the multiphase clock and have been processed with the one shot (U22) to provide a slight delay between them. This delay is adjustable from 40 nanoseconds to 200 nanoseconds by the 10 k_u potentiometer. This prevents any overlapping of the VCO outputs when they are multiplexed. The output of U12A is input to one of ramp generator circuits in Figure B-4, and the output of U12B is input to the other ramp generator circuit. This signal is then effectively OR'ed with the comparator outputs (U15 and U16) to produce the counter reset, the integrator reset and the mixer signal. This provides the timing relationships necessary to time multiplex the VCO's to give a 200 kHz repetition rate with a 98 percent duty cycle.

The ramp generator consists of a set of eight, 256 x 1 bit random access memories (RAMS) that are configured in 256, 8 bit words. These RAMS are addressed by a set of counters which are clocked and controlled by the timing and control electronics. This circuit is shown in Figure B-4. At the end of each scan the counters (U13 and U14) are cleared, which addresses location zero of the RAMS (U1 through U8). During the scan, the counters address RAM locations up through location 80, at which time the counters are cleared and location zero is again addressed. The digital comparators (U17 and U18) provide a clear signal to the counters when a location less than 80 is loaded by switch S7 into registers U15 and U16. This effectively shortens the sweep time of the VCO and provides for a variable bandwidth of its output.

In the write mode switch S6, in Figure B-5, loads the counters (U13 and U14) with the data from the address switches (Figure B-8). This addresses the RAMS at the desired location. The one shot (U12) provides a slight delay and allows the address to be set up at the RAMS before the write pulse is applied. When this occurs the data present at the RAMS from the data switches is loaded at the desired location. Data can be written into memory during any mode of operation.

Switch S1 provides either automatic or manual operation of the counters U13 and U14. In the automatic position, the counters run as they normally would. However, in the manual position, the counters are clocked by switch S4 in Figure B-5. This gives the operator the ability to clock through each location of memory and to examine and/or write data as desired.

Switch S2 disables the reset signals to the counters and enables them to address all 256 locations of the RAMS while running in the automatic mode. Switch S5 in Figure B-5, allows the operator to stop the counters at the location specified by the address switches. A new location may be addressed in this mode

by simply changing the address switches. Switch S3 allows the operator to clear the RAM's quickly while running in the automatic mode.

Latches U9 and U10 in Figure B-4, provide synchronization of data bits to the d/a. Data is collected from the RAMS by the latches and clocked to the d/a by a delayed version of the clock.

Each VCO linearization circuit must be programmed separately. The multiplexing circuit in Figure B-5, provides the operator with the ability to select the VCO he wishes to linearize. Switch S8 provides this function. When a VCO is selected, all switches and indicator LED's apply to that VCO. The other VCO goes into a normal run mode of operation and stays that way until it is selected. Special circuitry is incorporated to prevent the driving electronics from overdriving the VCO's while it is in any mode of operation except the normal run mode. This circuit is shown in Figure B-6. It was found that when a VCO was being linearized, a possibility existed that a memory word could be addressed that would continuously drive the VCO at a hf' voltage. This would not damage the VCO but would burn out the drive circuit. This condition was experienced several times. With the protection circuit incorporated the integrator in the driving electronics (as discussed in Sec. 3.3.6) is set to zero when any mode exists except the normal run mode.

The circuitry which is shown in Figure B-7, takes the digital output from the RAM's and converts it to an analog signal which varies from 0 to +30 volts, and is used as the control voltage input to the VCO.

The d/a converter, U1 converts the 8 bit digital data into an analog output which is input to operational amplifier U2. This amplifier has a gain of about 6, and converts the output of the d/a to a resultant signal that varies from 0 volts to +10 volts. The shape of the signal will depend on, of course, the characteristic of the particular VCO. This signal is then input to amplifier U3.

This amplifier is configured as an integrator and acts like a filter to remove the stair-step like characteristic that is generated by the d/a. This integrator is reset to zero by transistors Q1 and Q2 at the end of each scan by the control electronics. The output of the integrator (U3) is nominally a nonlinear ramp varying from 0 volts to -10 volts. This ramp is input to the closed loop made up of amplifier U5, offsetting transistor Q3, and current amplifier U6. The amplitude of the ramp can be varied with the 10 k Ω gain potentiometer. The closed loop has a maximum gain of 3, and as a result the output of U6 is nominally a ramp from 0 volts to +30 volts. Operational amplifier U4 provides a very stable reference voltage which is used for an offset control voltage to U5. Adjusting the 10 k Ω potentiometer moves the dc value of the ramp over a limited range.

In Figure B-9, U1A, U1B and U2A takes a 48 MHz signal from the timing and control electronics and divides it by five. U2B takes this signal and divides it again by two, producing a 4.8 MHz, 50 percent duty cycle square wave. U3 provides the necessary current drive to the Mixer. The L-C filter on the output of U3 is a 5-pole low pass filter that converts the square wave into an acceptable sine wave that can be used by the ATWL. The signal is then attenuated to the proper level and input to the mixer.

The gate control circuit for the mixer is shown in Figure B-10. Its timing signal is derived from the multiphase clock in Figure B-3. Its 200 kHz rate is input to a series of two one-shots. These one-shots provide for a variable gate width and a variable delay from the start of the AOBD scan to help achieve tracking between the AOBD and ATWL. This signal is then input to the transistor circuit which provides the proper level and drive capability for the mixer. The filter on the output of the transistor was not originally included. However, it was later determined experimentally that if the gated RF had a rounded envelope instead of a square envelope, less reflections occurred in the ATWL.

This filter provides a rounded pulse, variable in height, that gates the 4.8 MHz signal through the mixer.

THIS PAGE IS BEST QUALITY PRACTICABLE
FROM COPY FURNISHED TO DDC

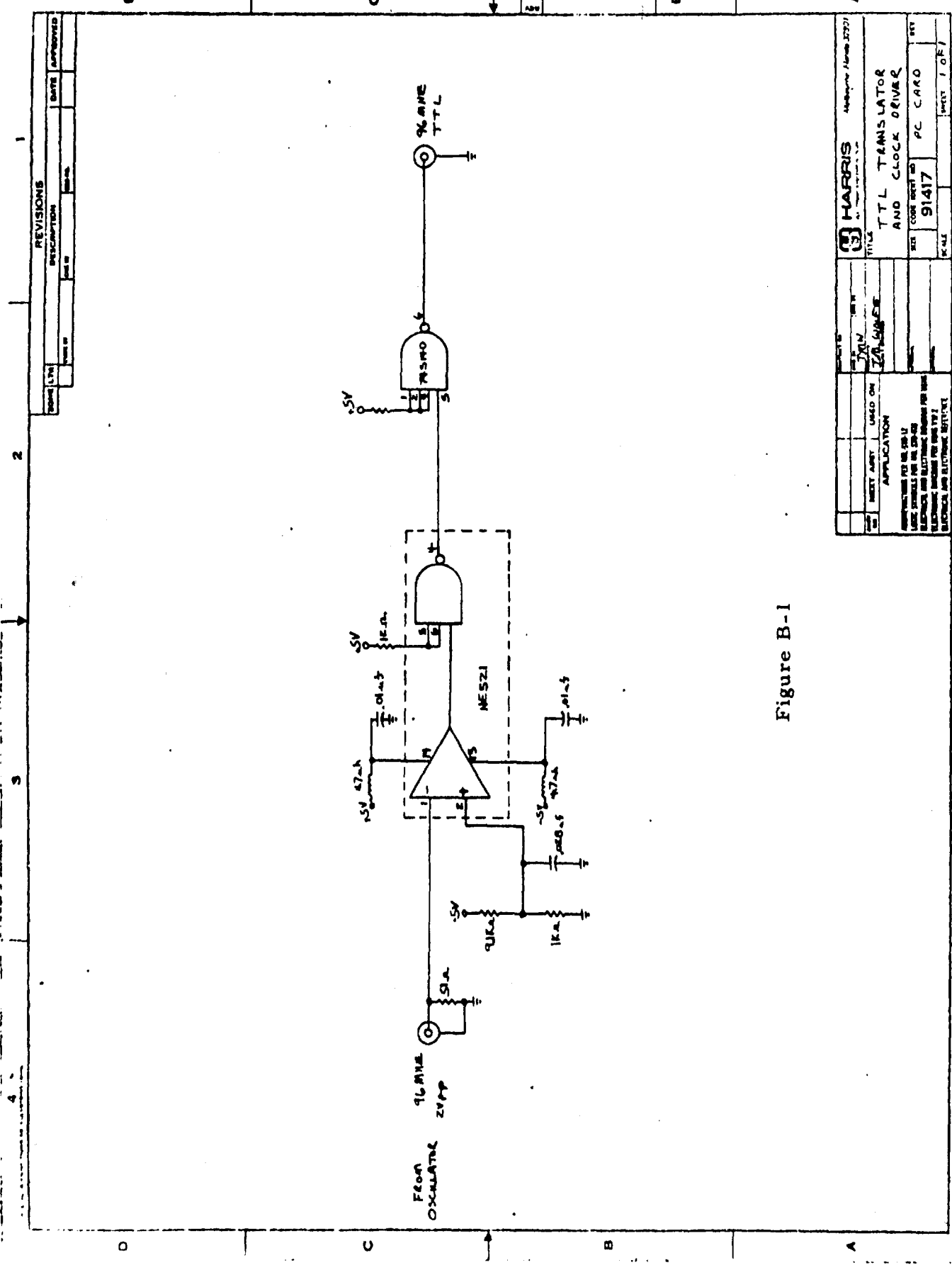


Figure B-1

THIS PAGE IS BEST QUALITY PRACTICABLE
FROM COPY FURNISHED TO DDC

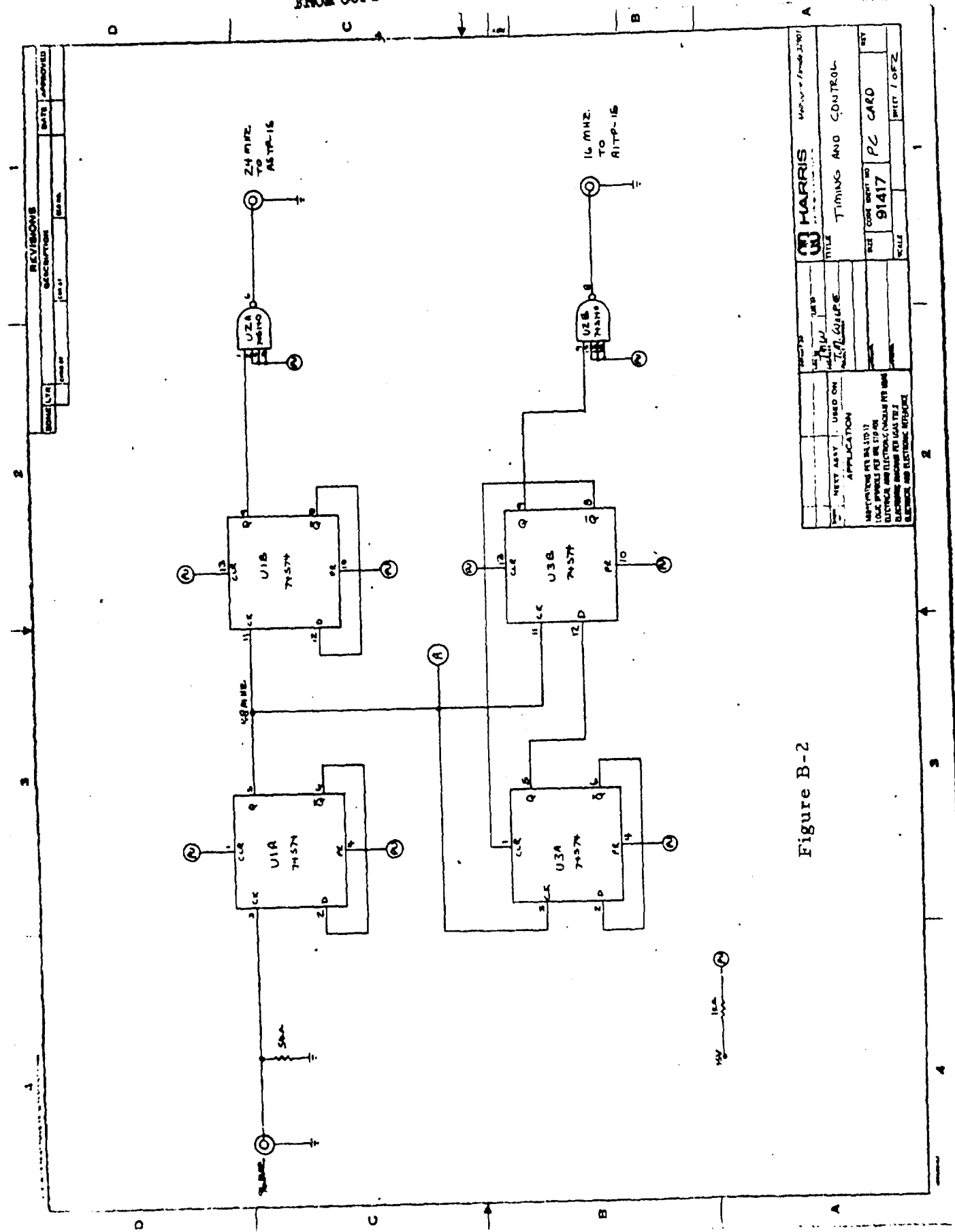


Figure B-2

THIS PAGE IS BEST QUALITY PRACTICABLE
FROM COPY FURNISHED TO DDC

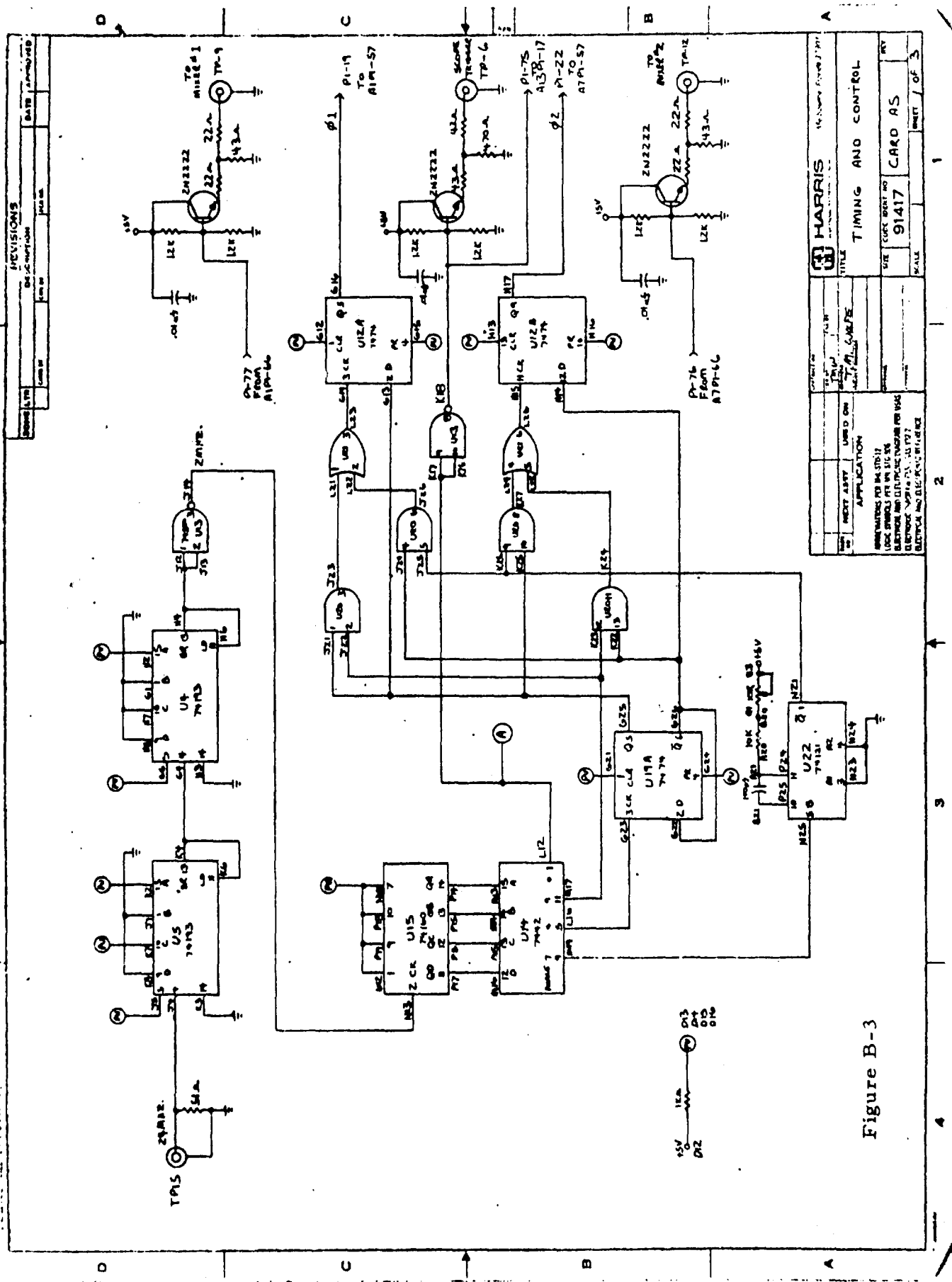


Figure B-3

THIS PAGE IS BEST QUALITY PRACTICABLE
FROM COPY FURNISHED TO DDC

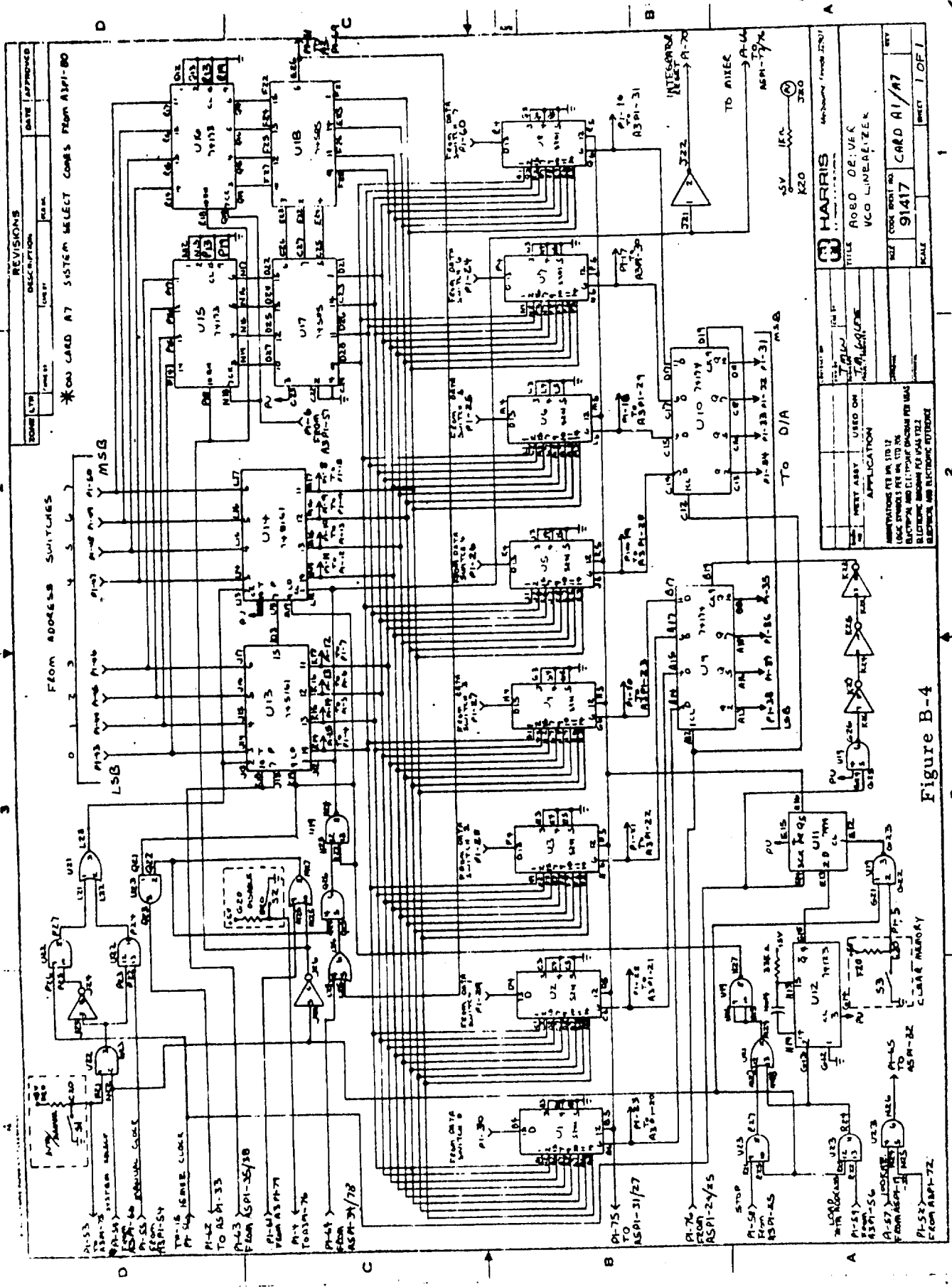


Figure B-4

THIS PAGE IS BEST QUALITY PRACTICABLE
FROM COPY FURNISHED TO DDC

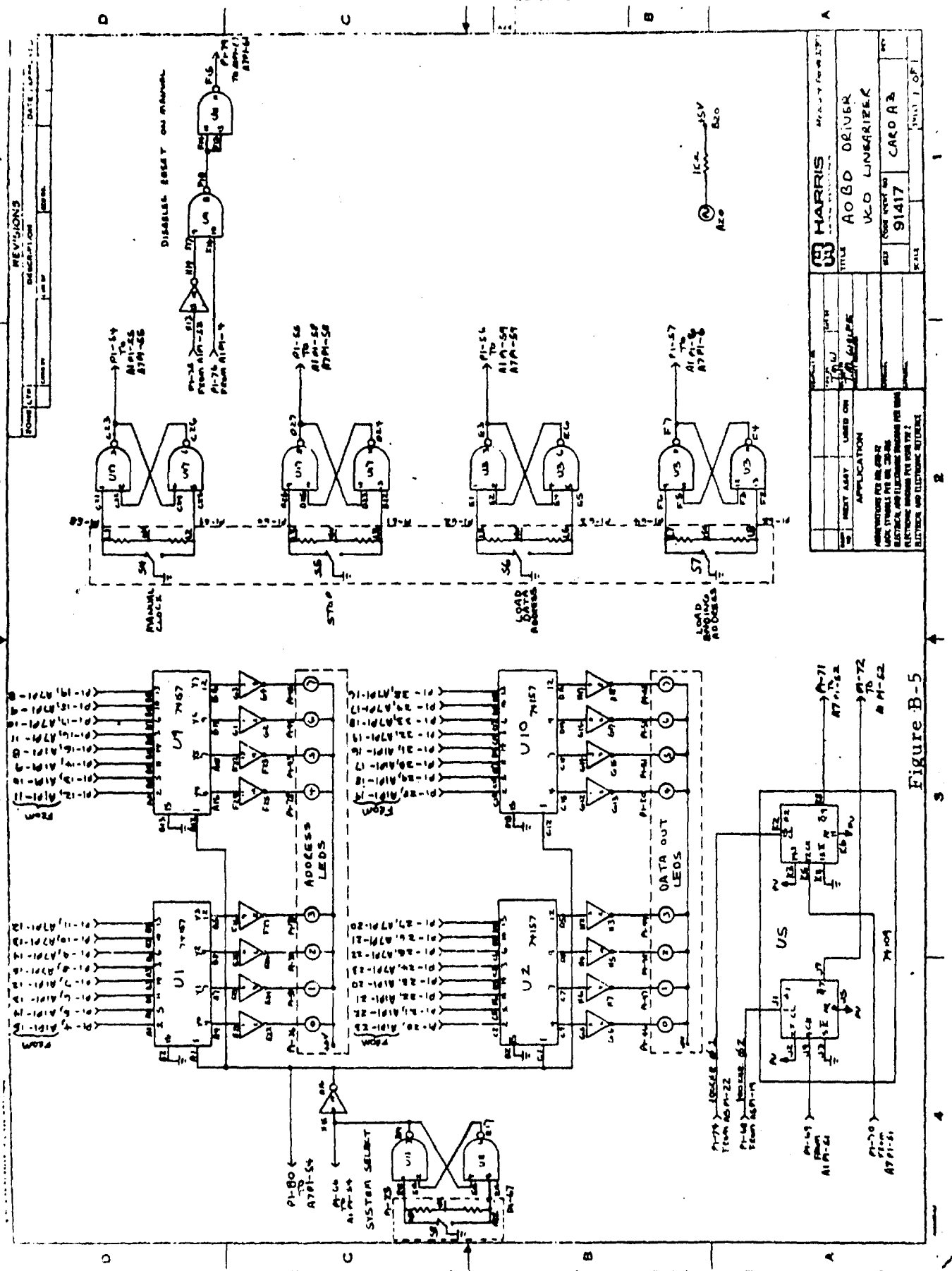


Figure B-5

THIS PAGE IS BEST QUALITY PRACTICABLE
FROM COPY FURNISHED TO DDC

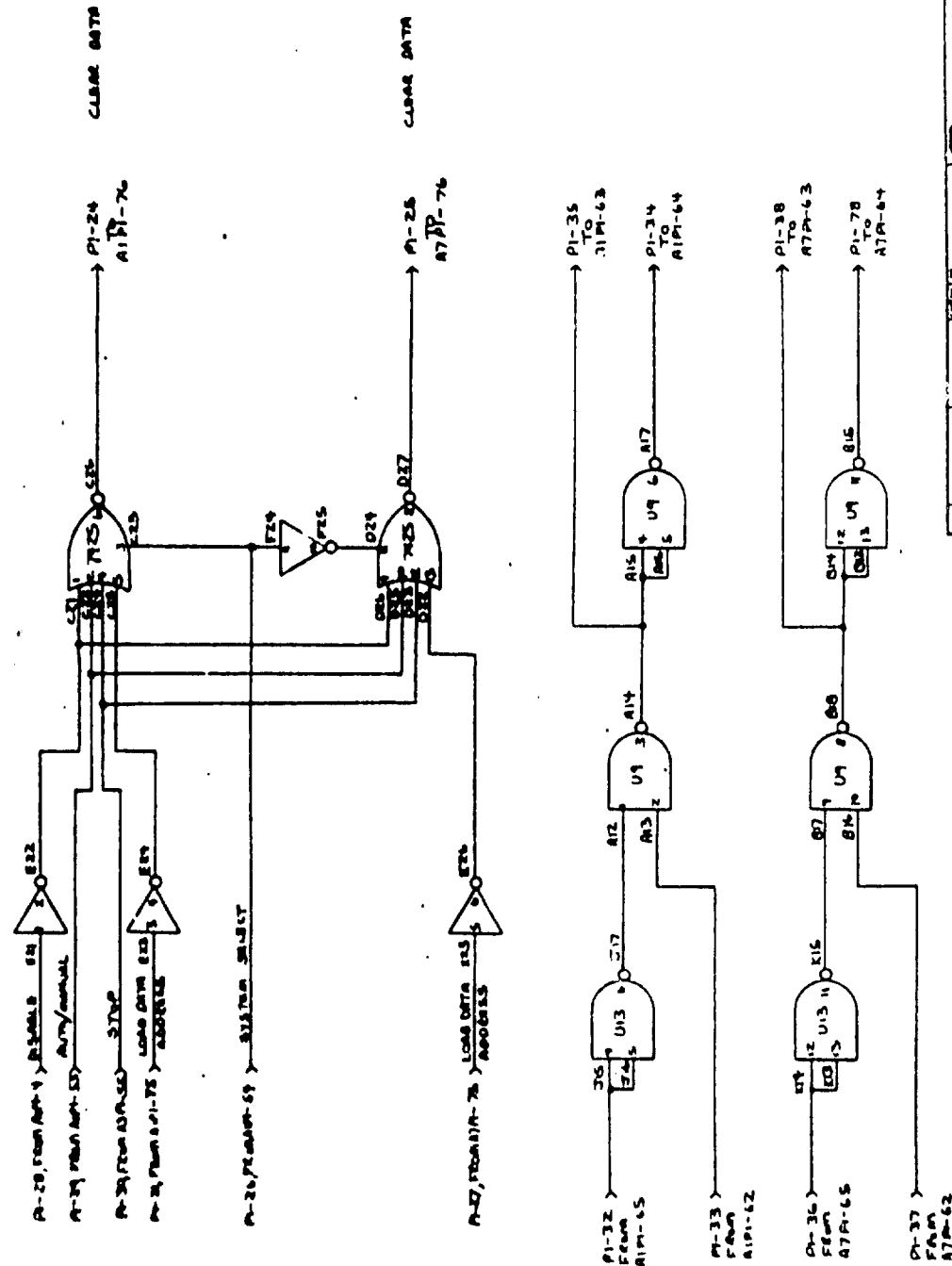


Figure B-6

HARRIS		TITLE AMILOC OUT PUT PROTECTION	
		DATE 10/10/81	
NEXT ASSY	USED ON	DATE	TIME
APPLICATION			
MANUFACTURED BY MIL-SP-100			
LARGE SIGNALS AND SMALL ELECTRONIC DESIGN FOR MILITARY, COMMERCIAL, AND INDUSTRIAL APPLICATIONS			
AMERICAN ELECTRONICS, INC., 1000 N. HANCOCK, CHICAGO, IL 60642			
TELEGRAMS: AELC, CABLE: AELC, TELETYPE: 312-224-1212			
91417	CARD AS	RECALL	RECALL
		PRINTED 3/5/83	PRINTED 3/5/83

THIS PAGE IS BEST QUALITY PRACTICABLE
FROM COPY FURNISHED TO DDC

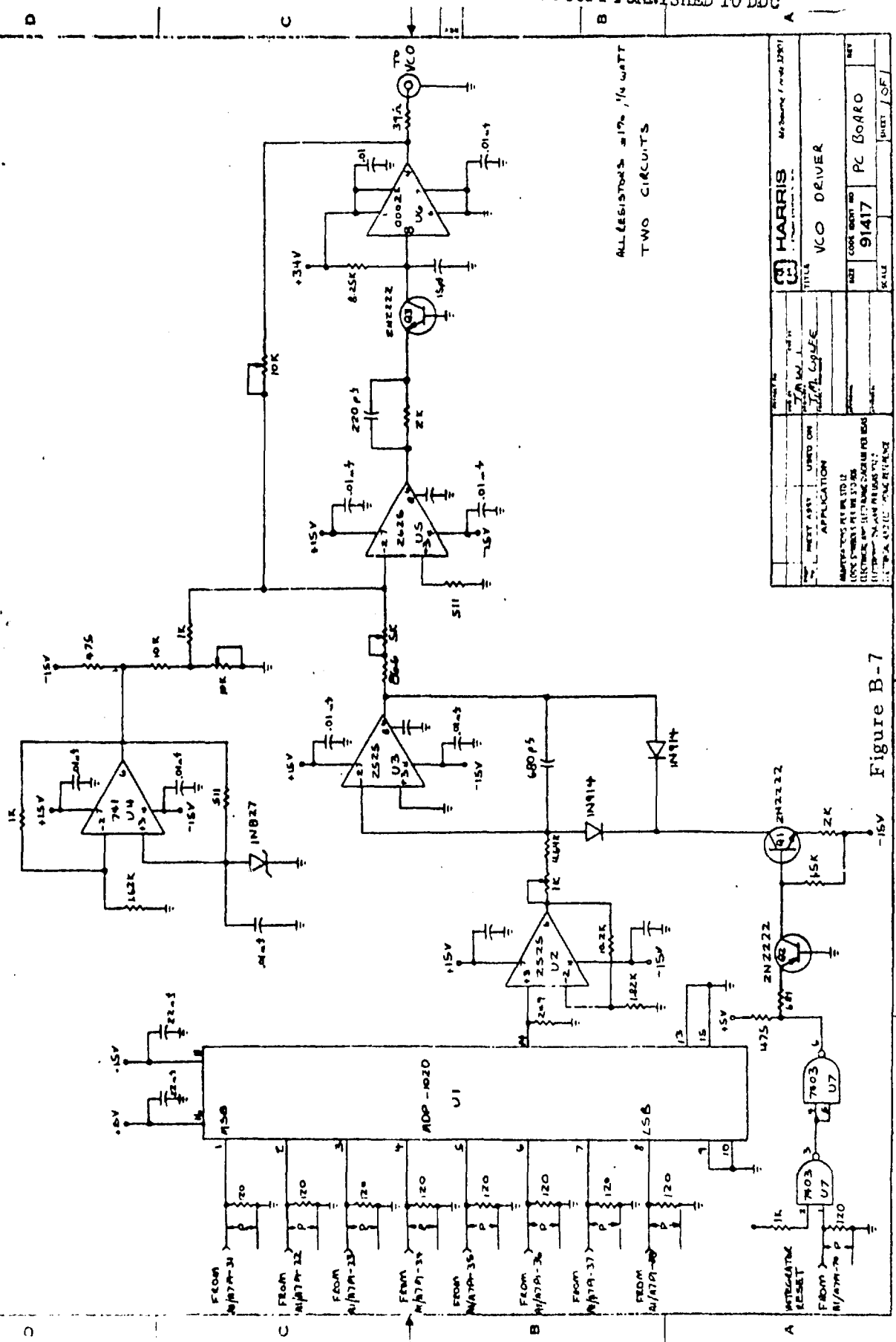


Figure B-7

THIS PAGE IS BEST QUALITY PRACTICABLE
FROM COPY FURNISHED TO DDC

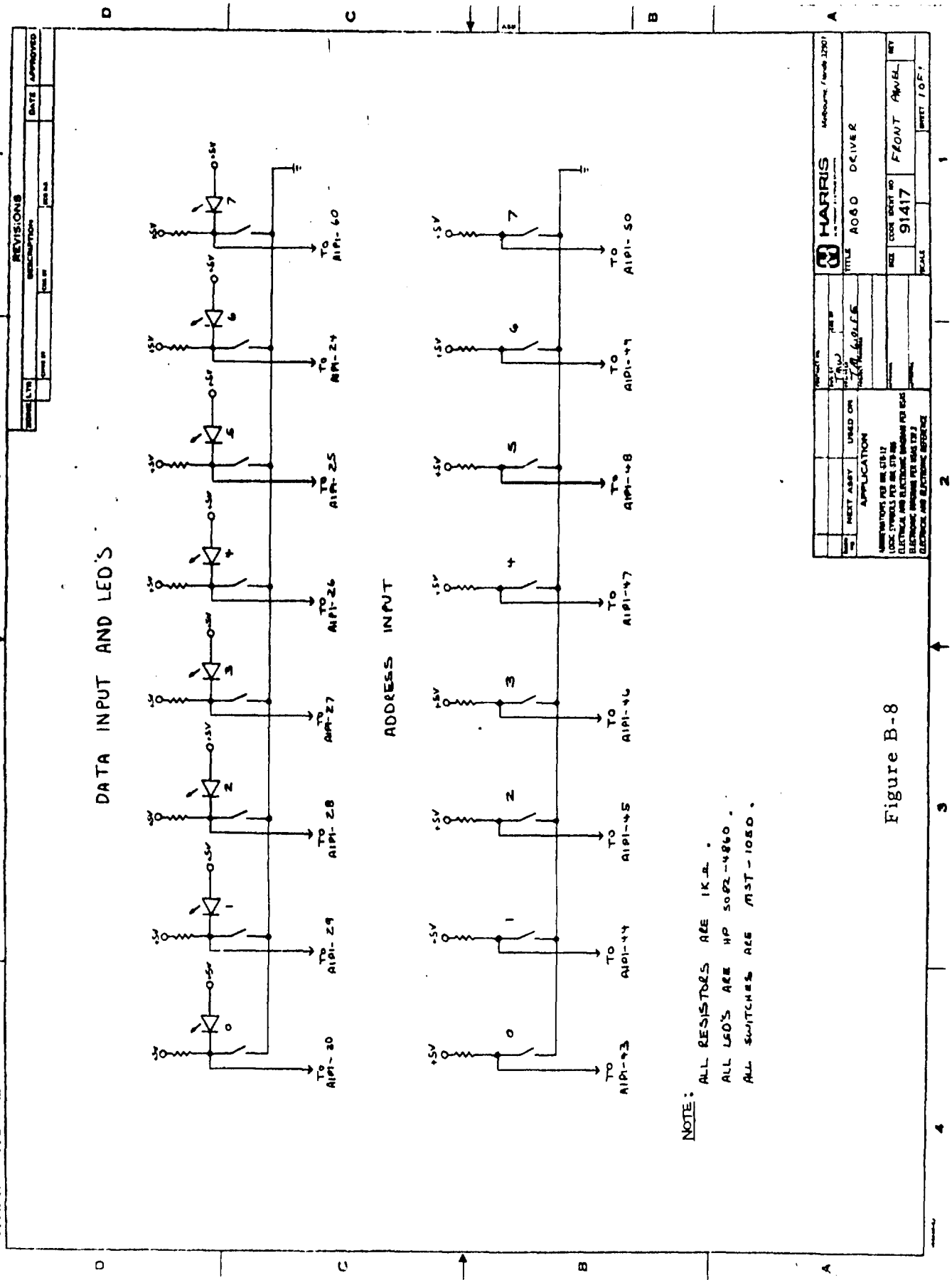


Figure B-8

THIS PAGE IS BEST QUALITY PRACTICABLE
FROM COPY FURNISHED TO DDC

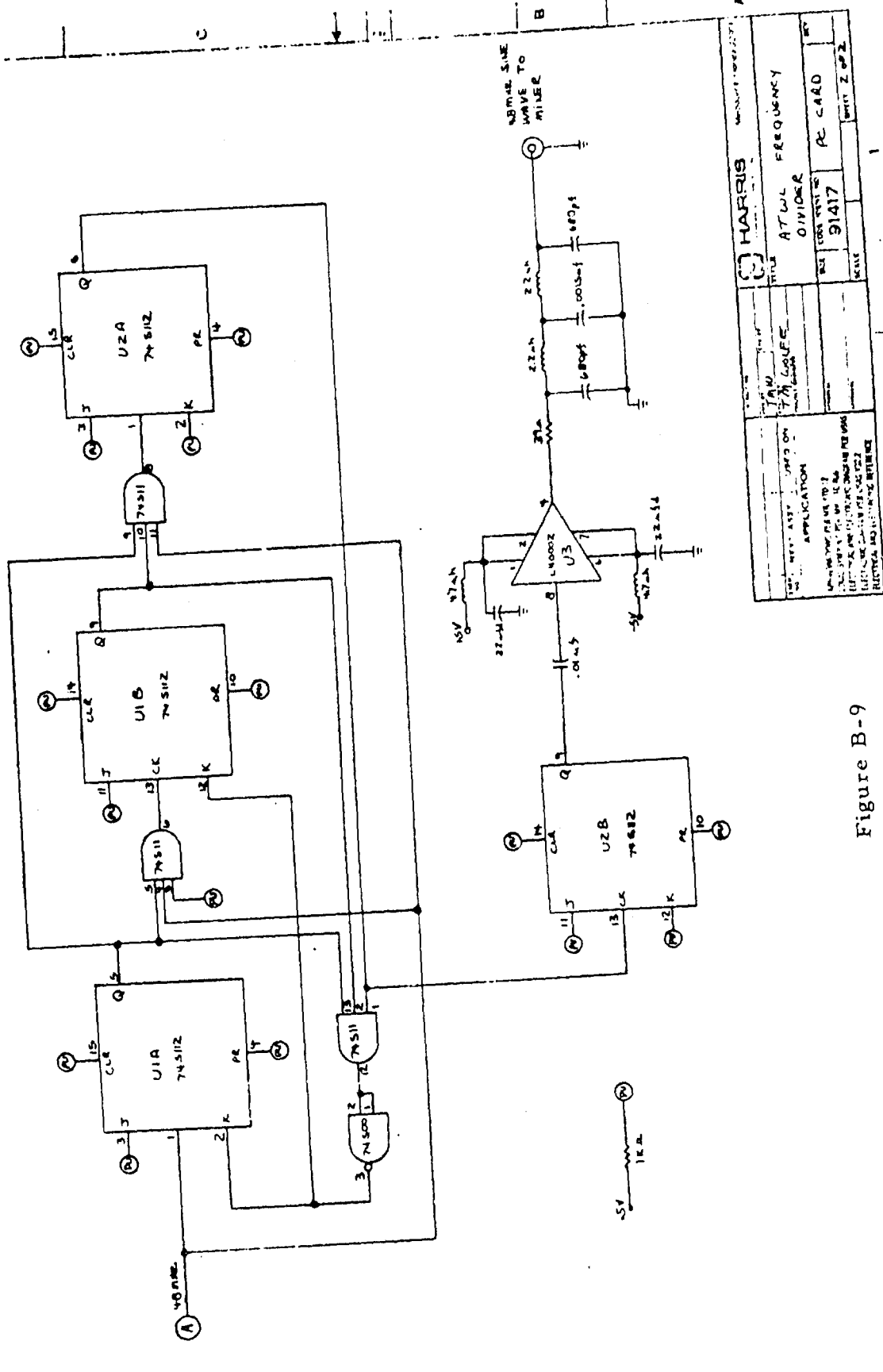


Figure B-9

THIS PAGE IS BEST QUALITY PRACTICABLE
FROM COPY FURNISHED TO DDC

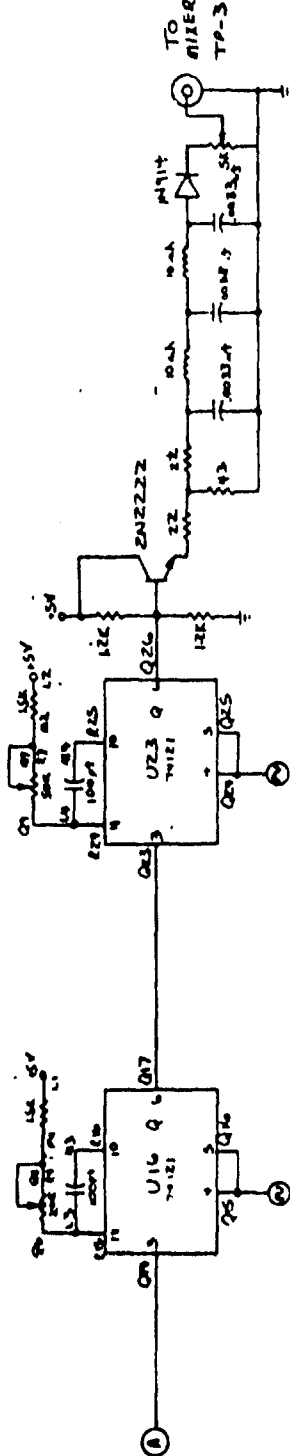
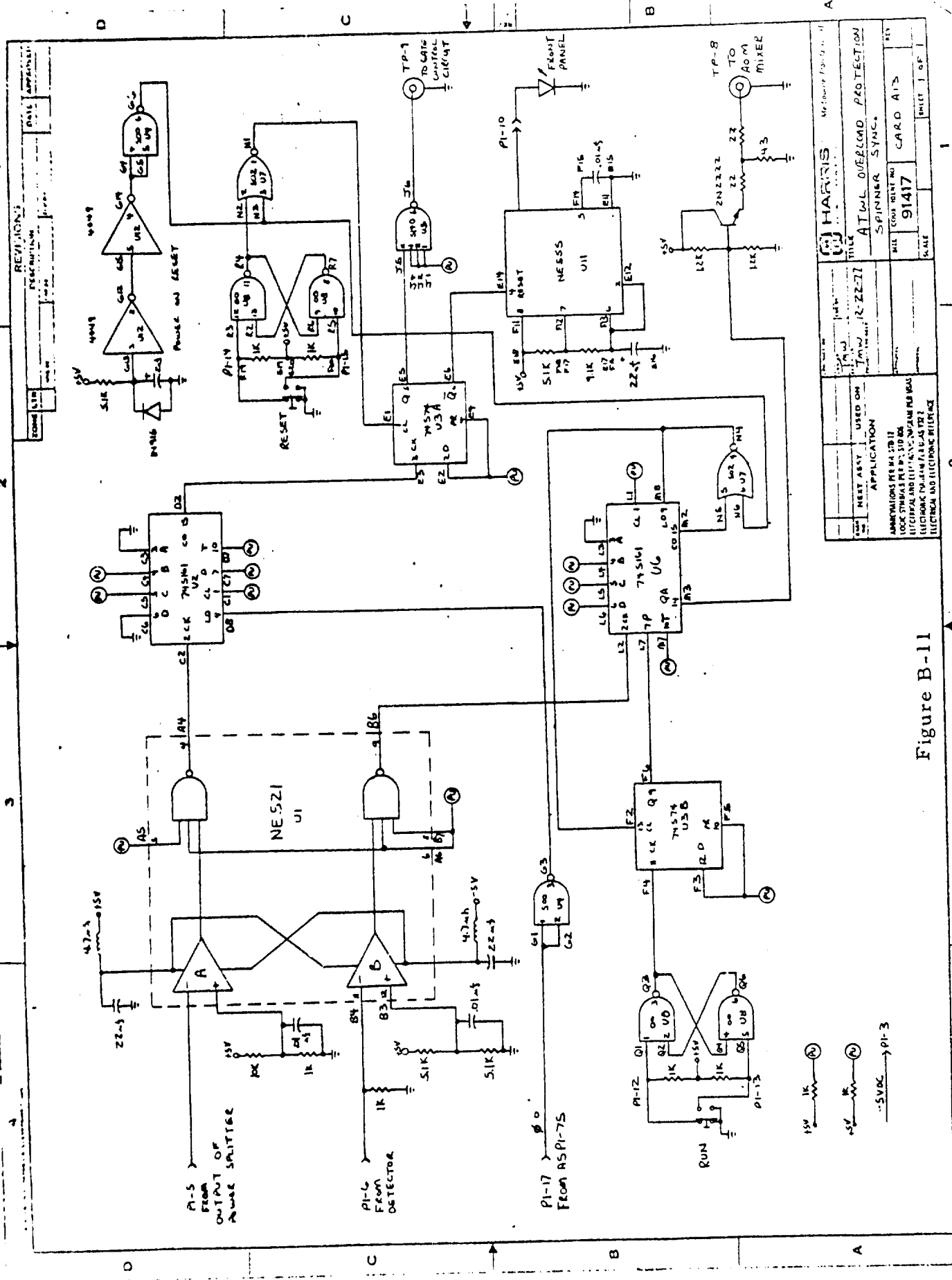


Figure B-10

HARRIS	
W	W
NAME	UNIT
NO. 1 MAY 2007 APPLICATION	UNDO ON TB CURE
ABSORPTIONS IN PULSE	
(LOC. SYMBOLS P. 612)	
DISTANT AND LOCAL CONTROL BY MEANS OF ELECTRIC CURRENTS	
ELECTRIC CURRENTS AND ELECTRIC INDUCTION	
TIME	TIME
10 sec	10 sec
TIMING AND CONTROL AT WL DURING TEST	PULSE WIDTH AND CARO AS
9417	9417
REMARKS	Safety 2 OF 3



APPENDIX C

PROM TEST

The PROM was functionally tested. An Air Force Resolution target was imaged onto the PROM using a coherent light source at 514.5 nm. A photograph of the AF Resolution target was made at the output plane, to measure the throughput resolution of the optical system. The throughput resolution of the optical system is shown in Figure C-1; the results show that the optical system will pass

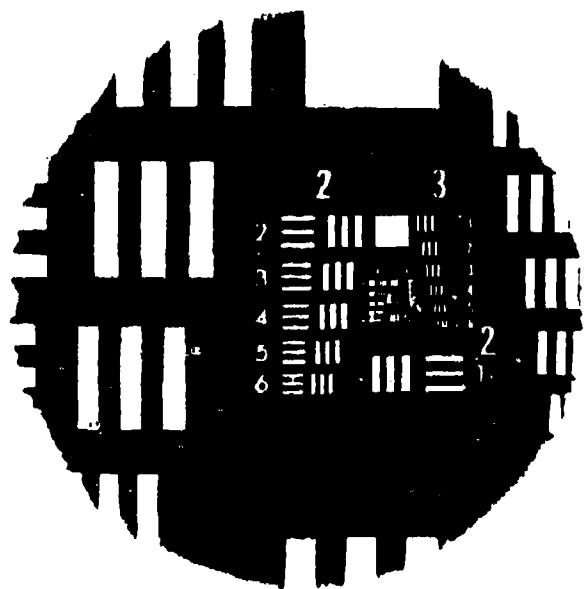
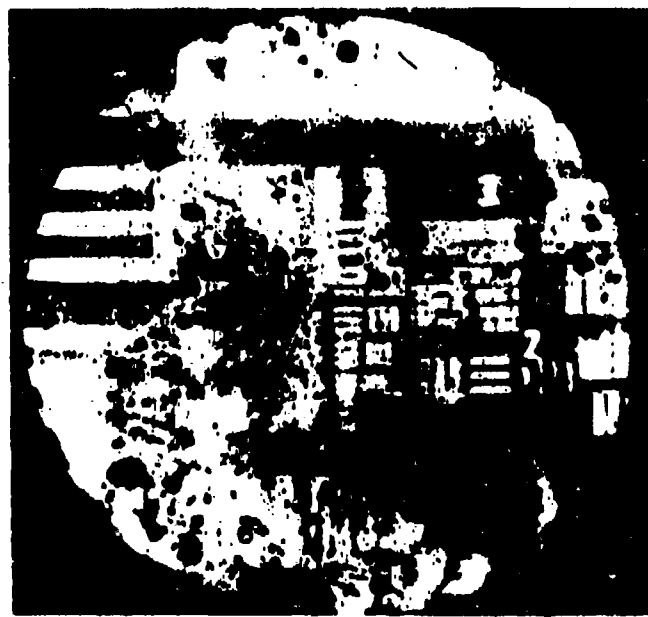
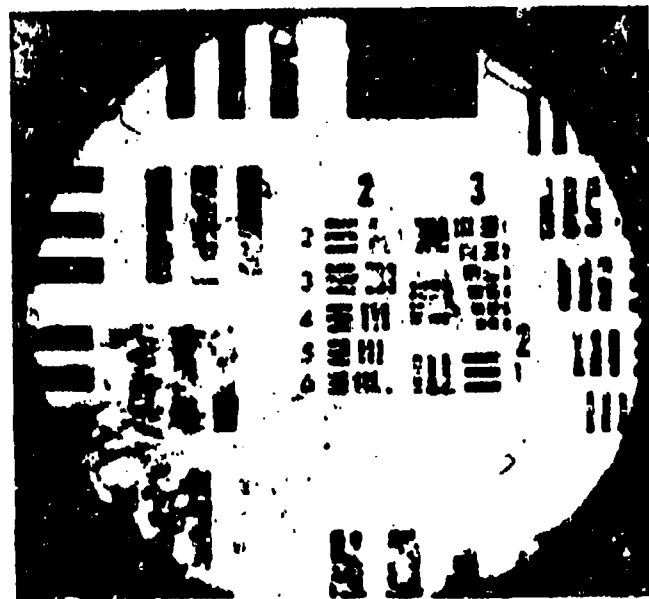


Figure C-1. Throughput Image of the AF Resolution Target

70 cycles/mm. An image of the AF Resolution target was recorded on the PROM. The recorded image was observed and photographed using a red filter on a microscope illuminator as the light source (a lens was used to quasi-collimate the light). A photograph of the image recorded on the PROM was made and is shown in Figure C-2a, where the maximum resolution of 18 cycles/mm was observed for the positive



a. IMAGE RECOVERED FROM PROM



b. REVERSED POLARITY IMAGE

Figure C-2. Signal Recovered From PROM

polarity. Figure C-2b shows the negative polarity case; the maximum resolution was only 14 cycles/mm for this case. Note the device has some local defects that are obscuring about 20-30 percent of the aperture. These defects cannot be seen with normal room lights - the defects are observed only when the device is operating and with polarized light.

The photometric sensitivity of the PROM was measured qualitatively (i.e., a certain amount of laser power was required to produce a satisfactory image). The exposure energy required to produce a reasonable image was 3 mJ/cm². This measurement indicates that the PROM is somewhat slower than the sensitivity reported in the literature - we did not determine the reason for this discrepancy.

REFERENCES

1. Nisenson, P. and S. Iwasa, Appl Opt. 11, 2760 (1972).
2. Feltneib, J. and D. S. Oliver, Applied Opt. 11, 2752 (1972).
3. Lipson, S. G. and P. Nisenson, Appl Opt. 13, 2052 (1974).
4. Foster, L. C., Crumly, C. B., and Cohoon, Appl Opt. 9, 2154 (1970).
5. Uchida, Naoya and Nobukazu Niizeki, Proc. IEEE 61, 1073 (1973).
6. Kogelnik, H., and T. Li, "Laser Beams and Resonators," Proc. IEEE, 54, pp. 1312-1329.
7. Sinclair, Douglas C., Editor, Image-Forming Optics (The Institute of Optics, University of Rochester, Rochester, New York: 1971)
8. Yao, S. K., and E. H. Young, "200 MHz Bandwidth Step-Array Acousto-Optic Beam Deflector," presented at the SPIE Symposium on Optical, Electro-Optical, Laser, and Photographic Technology, August 1976.
9. Reich, Stan, "The Use of Electro-Mechanical Mirror Scanning Devices," Laser Scanning Components and Techniques, SPIE Vol. 84. (The Society of Photo-Optical Instrumentation Engineers, Palos Verdes Estates, California: 1977), pp. 47-56.
10. Kinsler, L. E., Fundamentals of Acoustics, John Wiley and Son, Inc., NY, 1962.
11. Hecht, D. L., IEEE "Sonics and Ultrasonics", Vol. SU-24, No. 1, Jan. 1977